

First Principles Investigation of Thermoelectric Materials

A
thesis submitted
in partial fulfillment of the requirements for the degree of

DOCTOR OF PHILOSOPHY

by

Gautam Sharma

Roll No.: 20153418



**Department of Physics
Indian Institute of Science Education and Research, Pune
Pune - 411008, India**

2021

CERTIFICATE

Certified that the work incorporated in the thesis entitled **“First Principles Investigation of Thermoelectric Materials”** submitted by **Gautam Sharma** was carried out by the candidate, under my supervision. The work presented here or any part of it has not been included in any other thesis submitted previously for the award of any degree or diploma from any other University or institution.

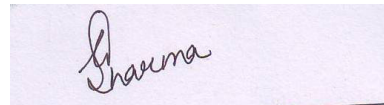


Date: 04-03-2022

(Dr. Prasenjit Ghosh)
Thesis supervisor

Declaration

I, Gautam Sharma, declare that this written submission represents my ideas in my own words and where others ideas have been included, I have adequately cited and referenced the original sources. I also declare that I have adhered to all principles of academic honesty and integrity and have not misrepresented or fabricated or falsified any idea/data/fact/source in my submission. I understand that violation of the above will be cause for disciplinary action by the Institute and can also evoke penal action from the sources which have thus not been properly cited or from whom proper permission has not been taken when needed.

A rectangular box containing a handwritten signature in black ink. The signature is written in a cursive style and appears to read 'G. Sharma'.

Date: 04-03-2022

(Gautam Sharma)

Acknowledgements

I want to thank my thesis supervisor, Dr. Prasenjit Ghosh, for his supportive attitude and constant guidance during the course. I am thankful to him for improving my scientific communication skills and cultivating research aptitude. I am thankful to my Research Advisory Committee members: Dr. Shouvik Datta and Dr. Mukul Kabir, for their valuable pieces of advice and fascinating comments to revamp my research work.

I thank Dr. Kuldeep Singh (ARIES, Nainital) for teaching me tactics of scientific programming languages. My special thanks to Mr. Vineet Kumar Pandey for the fruitful scientific discussions. I am grateful to my seniors, Dr. Nandha Kumar, Dr. Niharika Joshi, Dr. Krishnakanta Mondal, Dr. Nishamol Kuriakose, Dr. Rahul Hardikar, Dr. K.C. Bhamu, and Dr. Subramanyam Sappati for their valuable pieces of advice and motivating discussions. I would like to acknowledge my labmates Unmesh Mondal, Aswathi Mohan, Amit Sahu, Kanika Kohli, Ankit Kumar, Rajeev Ranjan, Prajjwal, and Sarika Lohkna for valuable suggestions related to other scientific discussions and their moral support. I am lucky to have supportive and caring IISER Pune friends (Sumit Srivastav, Anweshi Dewan, Remya N, Imran Mulani, Suddhasattwa Mandal, Debesh Bhattacharjee, Ajith VJ, and Soumendra Nath Panja).

I like to use this opportunity to thank my Panjab University friends to keep the aliveness of life (Anuj Gupta, Anurag Verma, Shankar Lal, Avneet Singh, Shilpa Kumari, Sourav Jain, Lakhwinder Singh, Manjit Singh, Karun Mehta, Harwinder Singh Bindra, AP Singh, Vishal Goyal, and Varun Gorki). I like to express a sincere gratitude towards Gaurav Singh, Anurag Ojha and Simarjit Singh from S.C.D. Government college, Ludhiana. I want to thank all Professors from Panjab University (particularly Dr. C.S. Aulakh, Dr. Sandeep Sahijpal, Late Dr. Kuldeep Kumar, and Dr. C.N. Kumar, whose knowledge and teaching have always inspired me). I am thankful to the most precious high school teacher Mr. Sanjeev Chaudhary from Paonta Sahib, Himachal Pradesh.

I am grateful to Prof. Jayant B. Udgaonkar and Dr. K. N. Ganesh, Director of IISER Pune, for providing an excellent research environment. I thank the IISER Pune library for accessing the research journals and books.

I would like to acknowledge the Center for Modelling and Simulation, University of Pune for access to computing resources of Sahasrar, IISER Pune for access to computing resources of Athena and Fermi, Centre for Development of Advanced Computing (CDAC), Pune for access to computing resources of PARAM Yuva, and Centre for Computational Material Science, Tohoku University, Japan for providing access to computing facilities at Masamune-IMR. I would also like to acknowledge National Supercomputing Mission (NSM) for providing computing resources of 'PARAM Brahma' at IISER Pune, which is implemented by C-DAC and supported by the Ministry of Electronics and Information Technology (MeitY) and Department of Science and Technology (DST), Government of India. Funding provided by DST, Govt. of India (Grant No: EMR/2016/005275 and SR/NM/TP-13/2016) is also acknowledged. I like to express my sincere gratitude to IISER Pune for the fellowship.

I would like to thank and dedicate this thesis to my parents (Mr. Khem Raj Sharma and Mrs. Seema Rani Sharma). I am grateful to my brothers Jaipal Sharma and Ajay Sharma for their love and support. I am grateful to my wife, Dr. Aarti Shukla, for her loving, caring, and supportive nature. I would like to thank Mr. Avinash Shukla and Mrs. Sandhya Shukla for belief in me.

List of Publications

List of publications resulting from work presented in this thesis

1. Gautam Sharma, Shouvik Datta, Prasenjit Ghosh, “First Principles Investigations of Structural, Electronic and Transport Properties of $\text{BiI}_3/\text{ZrS}_2$ van der Waals Heterostructure: A Thermoelectric Perspective”, *Journal of Electronic Materials*, 50, 1644-1654, (2021).
2. Gautam Sharma, Vineet Kumar Pandey, Shouvik Datta, Prasenjit Ghosh, “Effect of Electron-Phonon Coupling on Transport Properties of Monolayers of ZrS_2 , BiI_3 and PbI_2 : A thermoelectric Perspective”, *Physical Chemistry Chemical Physics*, 23, 11663-11671, (2021).
3. Gautam Sharma, Shouvik Datta and Prasenjit Ghosh, “Effect of Resonant Doping on Electronic and Transport Properties of BaCu_2Se_2 ” (manuscript under preparation)

List of publications from other works

1. K.C. Bhamu, Enamul Haque, C. S. Praveen, Nandha Kumar, G. Yumnam, Md. Anwar Hossain and Gautam Sharma “Improving the optical and thermoelectric properties of $\text{Cs}_2\text{InAgCl}_6$ with heavy substitutional doping: a DFT insight”, *RSC Advances*, 11, 5521-5528, (2021).

Synopsis

Thermoelectric (TE) materials have attracted particular attention in the last decade because they act as a green way of converting waste heat energy to electrical energy through Seebeck effect. The efficiency of a thermoelectric device is measured by the dimensionless figure of merit (ZT), which is directly proportional to the square of Seebeck coefficient, electrical conductivity, and inversely proportional to thermal conductivity. Depending on the operational temperatures, materials like bismuth telluride, lead halides, MgAgSb, skutterudites, and copper and tin chalcogenides are promising candidates for use in thermoelectric devices. To the best of our knowledge, the highest reported value of ZT is about 2.6 at 573 K, which is observed for cadmium-doped AgSbTe₂ (Science, 371, 722727 (2021)). In terms of the efficiency of thermoelectric devices, the presently achievable ZT is still quite small compared to traditional power generators. Hence, there are still efforts to improve/design novel materials with high ZT . Improving ZT implies that one needs to increase Seebeck coefficient and electrical conductivity and reduce lattice thermal conductivity. However, the mechanisms that improve one of them deteriorate the other, making it challenging to design novel materials with improved ZT . Over the last several years, many strategies like nanostructuring, band structure engineering, heterostructure formation, dimensionality reduction, etc., have been developed to improve ZT .

In addition to experimental techniques, computational materials design is also an important tool for the discovery of novel thermoelectric materials. In this thesis, using computational tools like density functional theory, semiclassical Boltzmann transport theory, and many-body electron-phonon coupling, we have studied two aspects of computational research in thermoelectric materials. This thesis is divided into two parts consisting of six chapters.

Chapter 1 provides the general introduction to the field of thermoelectrics, challenges

hindering the progress of the field, and strategies to overcome these challenges. We have briefly discussed two main strategies employed in the first part of this thesis to improve the thermoelectric properties of bulk and layered materials.

In **Chapter 2**, we have briefly explained the density functional theory (DFT) and its practical facets of the plane-wave implementation. DFT has been exploited to compute the electronic structure properties. This information is further combined with Boltzmann transport theory to determine the transport properties of the materials under consideration.

The first part of the thesis consists of two chapters where we have used conventional computational methods to study the effect of structural modifications on the electronic structure and transport properties of bulk and layered materials.

Chapter 3 deals with a bulk material, copper chalcogenides (BaCu_2Se_2), which is a promising thermoelectric material. We have exploited the band engineering technique to investigate how doping BaCu_2Se_2 with suitable dopants introduces resonant states in the electronic band structure of this material. As of result, it leads to improvement in transport properties of the system.

Chapter 4 is based on the idea of reduced dimensionality suggested by Dresselhaus *et al.* In this work, we have selected monolayers of BiI_3 and ZrS_2 to form a novel van der Waals heterostructure. We have shown how this heterostructure can improve the transport properties compared to the individual monolayers.

The second part of the thesis consists of **Chapter 5**, where we have critically examined the validation of some approximations that are typically made in the calculations. It is important to compute carrier relaxation time to predict the transport properties of novel materials. Usually, this is computed using deformation potential theory where only coupling of electrons/holes and acoustic phonons are considered. Our work shows that for ionic solids (like BiI_3 and ZrS_2 monolayers), the coupling of charge carriers with optical phonons is significantly substantial. Neglecting them, while computing relaxation times not only results in quantitative errors (by orders of magnitude) but also gives qualitative incorrect trends.

Contents

List of Publications	v
Synopsis	vi
List of Figures	xii
List of Tables	xvii
1 Introduction	1
1.1 Thermoelectric Effects	1
1.1.1 Seebeck effect	1
1.1.2 Peltier effect	2
1.2 Efficiency of thermoelectric device	2
1.3 Classes of TE materials	3
1.3.1 Phonon glass electron crystal based TE materials	3
1.3.1.1 Skutterudites	3
1.3.1.2 Clathrates	4
1.3.2 Metal Oxides	5
1.3.3 Half-Heusler (HH) alloys	5
1.3.4 Metal chalcogenides	6
1.3.4.1 Lead chalcogenides	6
1.3.4.2 Bismuth chalcogenides	7
1.3.4.3 Superionic conductors (SICs)	7
1.3.4.4 Layered structure materials	7
1.3.4.5 Other metal chalcogenides	8
1.3.5 Metal Halides	8
1.4 Strategies to enhance ZT	9
1.4.1 Resonant doping	9

1.4.1.1	Resonant levels	9
1.4.1.2	Resonant doping and thermoelectricity	10
1.4.2	Reduced dimensionality	11
1.5	Thesis outline	11
2	Theoretical methods	13
2.1	Many body Schrödinger equation	13
2.2	Adiabatic or Born-Oppenheimer approximation	14
2.3	Density functional theory	15
2.3.1	Hohenberg-Kohn theorems	15
2.3.2	Kohn and Sham Approach	17
2.3.3	Exchange and correlation	18
2.3.3.1	Local density approximation (LDA)	20
2.3.3.2	Generalized gradient approximation (GGA)	20
2.4	Periodic Supercells	21
2.4.1	Bloch's theorem	21
2.4.2	k -point sampling	22
2.4.3	Pseudopotentials	23
2.5	Electron-phonon interactions	23
2.5.1	History of the electron-phonon interactions	24
2.5.1.1	Metals	25
2.5.1.2	Semiconductors	26
2.5.1.3	Ionic materials	26
2.5.1.4	First calculations of EPIs from first principles	27
2.5.2	Electron-phonon interactions in DFT	27
2.5.2.1	Standard formalism of lattice vibrations	27
2.5.3	EP coupling Hamiltonian	29
2.5.3.1	KS Hamiltonian	29
2.5.3.2	EP coupling Hamiltonian to first and second order in DFT	29
2.5.3.3	Calculation of EP matrix elements	30
2.6	Electron self-energy	32
2.7	Semiclassical Boltzmann Transport	34
3	Identifying resonant dopants for BaCu₂Se₂	36
3.1	Introduction	36

3.2	Computational details	37
3.3	Results and discussion	38
3.3.1	Structure and electronic properties of BaCu_2Se_2	38
3.3.2	Effect of doping BaCu_2Se_2	40
3.3.3	Transport properties of doped configurations	42
3.4	Summary	46
4	First Principles Investigations of Structural, Electronic and Transport Prop- erties of $\text{BiI}_3/\text{ZrS}_2$ van der Waals Heterostructure[†]	47
4.1	Introduction	47
4.2	Computational details	49
4.3	Results and discussion	51
4.3.1	Structure and energetics	51
4.3.2	Electronic properties	54
4.3.3	Computation of relaxation time	57
4.3.4	Electronic transport properties	59
4.4	Summary	63
5	Effect of Electron-Phonon Coupling on Transport Properties of Monolay- ers of ZrS_2, and BiI_3: A thermoelectric Perspective	64
5.1	Introduction	64
5.2	Computational details	66
5.3	Results and discussion	68
5.3.1	Crystal structure and lattice vibrations.	68
5.3.2	Temperature dependent renormalization of the band structure.	70
5.3.3	Computation of τ	73
5.3.3.1	τ from electron-phonon coupling.	73
5.3.3.2	τ from deformation potential theory.	74
5.3.4	Transport properties	76
5.3.4.1	Transport properties with τ obtained from EPIs and DP theory.	76
5.3.4.2	Effect of CRTA and EPIs on transport properties.	76
5.4	Summary	78
A		82

A.1	Computational details	82
A.2	Determination of U	82
A.3	Effect of doping BaCu ₂ Se ₂	83
B		86
B.1	Mode-resolved imaginary part of electron-phonon self-energy	87
Bibliography		88

List of Figures

1.1	Schematic of thermocouple demonstrating (a) Seebeck effect (b) Peltier cooling.	2
1.2	(a) Schematic diagram of a conduction band with defect state (blue) and a resonant state (pink) and (b) resonant state producing distortion in density of states (DOS).	10
2.1	KS equations can be solved as illustrated by self consistent cycle.	19
2.2	Schematic demonstration of all-electron (solid red lines) and pseudo-electron potential (dashed red lines) and corresponding wavefunctions (green curves). All-electron and pseudopotential coincide beyond cut-off radius (r_c). (Reprinted with permission from ref. [1]. Copyright ©1992, American Physical Society)	24
2.3	Feynman diagram for electron self-energy arising due to EPIs within Migdal approximation. This diagram is made up of two diagrams representing the phonon emission (left half) and absorption (right half).	33
3.1	(a) Crystal structure of orthorhombic BaCu_2Se_2 . Brown, red, blue and green colored spheres are used to represent Ba, Cu_1 , Cu_2 and Se atoms, respectively. (b) Electronic band structure (left) and the projected density of states (right) of BaCu_2Se_2 computed at the PBE+U level. The valence band maximum (VBM) is set to zero.	39
3.2	The formation energies are computed for boron group of elements doped on Cu, Se and Ba lattice sites.	41
3.3	The total DOS of pristine (black) and doped (red) BaCu_2Se_2 computed at the level of PBE+U. The DOS projected on dopant s and p -states are shown in dashed and solid blue lines respectively. (a), (b), (c) and (d) are for Al, Ga, In and Tl doped cases. The dopant atom occupies Cu_1 -site. The VBM is set to zero in all the cases.	43

3.4	The total DOS of pristine (black) and doped (red) BaCu ₂ Se ₂ calculated at the level of PBE+U. The DOS projected on dopant <i>s</i> and <i>p</i> -states are shown in dashed and solid blue lines respectively. (a), (b), (c) and (d) are for Al, Ga, In and Tl doped cases. The dopant atom occupies Cu ₂ -site. The VBM is set to zero in all the cases.	44
3.5	(a,d) $ S $, (b,e) σ/τ and (c,f) PF/ τ as a function of carrier concentration for pristine and doped configurations corresponding to Cu ₁ -site (left) and Cu ₂ -site (right).	45
4.1	The top and side views of the structures of a monolayer of (a) ZrS ₂ and (b) BiI ₃ . The two-dimensional unit cell for each case is denoted by a black parallelogram. The large light green and violet spheres denote Zr and Bi ions respectively. The S (I) atoms in the top and bottom layers of ZrS ₂ (BiI ₃) are represented with yellow (blue) and golden (green) spheres respectively.	52
4.2	The side (a,c and e) and top view (b,d and f) for HS-BiI ₃ /ZrS ₂ in configurations (B'BC, B'BA and B'AC, respectively). The Bi, Zr, I _{up} , I _{down} , S _{up} and S _{down} atoms are represented by violet, light green, blue, dark green, yellow and golden colored spheres, respectively.	53
4.3	The electronic band structure computed using PBE (blue) and Gau-PBE (red) functionals for monolayers of ZrS ₂ (a), BiI ₃ (b) and the B'BC configuration of the HS(c). The Fermi energy is set to zero.	55
4.4	(a) The band structure of the HS projected on the BiI ₃ electronic states. Black lines represent the bands arising from ZrS ₂ and colored lines represent the bands arising from BiI ₃ . (b) The density of states projected onto the atomic orbitals of Bi, Zr, I and S. Both are computed using PBE+vdW+SOC. (c) Planar average of the charge transfer due to the formation of the HS.	56
4.5	Magnified view of the band structure around (a) the conduction band minima and (b) valence band maxima of the HS. For sake of comparison, also shown in (a) and (b) the same for ZrS ₂ and BiI ₃ monolayers respectively. For both the cases, the bands are shifted with respect to the minima and maxima respectively.	57

4.6	Seebeck coefficient (α) as a function of chemical potential (μ) in (a) ZrS_2 , (b) BiI_3 and (c) HS. The black, red and green plots are at 300 K, 400 K and 500 K respectively. Negative (Positive) values of μ denote holes (electrons).	60
4.7	Electronic conductivity, σ (a, b, c), power factor PF (d, e, f) and electronic contribution to thermal conductivity, κ (g, h, i) for holes as a function of the chemical potential (μ) at three different temperatures, namely 300 K, 400 K and 500 K. The first, second and third columns are results for ZrS_2 , BiI_3 and the HS respectively.	61
4.8	Electronic conductivity, σ (a, b, c), power factor PF (d, e, f) and electronic contribution to thermal conductivity, κ (g, h, i) for electrons as a function of the chemical potential (μ) at three different temperatures, namely 300 K, 400 K and 500 K. The first, second and third columns are results for ZrS_2 , BiI_3 and the HS respectively.	61
4.9	Effect of τ and band gap on σ of holes (a) and electrons (b). In the figure legend, E_g denotes band gap and τ denotes the relaxation time.	62
5.1	The top and the side view of (a) ML- ZrS_2 and (b) ML- BiI_3 , where Sulfur (Iodine) is represented by light yellow (light green) and dark yellow (dark green) colored balls belonging to two different sublayers. Zr and Bi are shown by sky blue and red balls respectively.	69
5.2	The phonon band structures (a) ML- ZrS_2 and (b) ML- BiI_3	70
5.3	The DFT band structure (black) and the renormalized ones at 0K (colored lines) for (a) ML- ZrS_2 , (b) ML- BiI_3 and at 300 K ((c) ML- ZrS_2 , (d) ML- BiI_3). For the renormalized band structure, the magnitude of the imaginary part of electron-phonon self energy is also shown. For both the cases, the energy eigenvalues are shifted with respect to the Fermi energy. The Fermi energy is taken to be at the middle of the band gap.	71
5.4	The variation of the renormalized band gap as a function of temperature for (a) ML- ZrS_2 (left panel) and (b) ML- BiI_3 (right panel).	72

5.5	The imaginary part of the electron self-energy for the conduction (solid lines) and valence band (dashed lines) for ML-ZrS ₂ (a) and ML-BiI ₃ (b) at 300 K (black), 400 K (red) and 500 K (blue). The vibrational patterns of optical modes at Γ point which have the largest contribution to $\text{Im}\Sigma_{n,k}$ are shown for ML-ZrS ₂ and ML-BiI ₃ in (c-d). The average relaxation times for electrons (blue) and holes (red) as a function of temperature for the ML-ZrS ₂ (e) and ML-BiI ₃ (f) are also shown.	79
5.6	The average relaxation time estimated using deformation potential theory for electrons (blue) and holes (red) as a function of temperature for (a) ZrS ₂ and (b) BiI ₃ monolayers.	80
5.7	Comparison of the transport properties for n-type (solid lines) and p-type (dashed lines) doping of ML-ZrS ₂ at 300 K, where τ for the charge carriers is obtained using EPIs (top panel) and deformation potential approximation (bottom panel).	80
5.8	The transport properties as a function of chemical potential (μ) based on DFT-BS and CRTA [DFT-BS (τ_{CRTA})] (black solid lines), DFT-BS and with explicit values of τ_{nk} for each state [DFT-BS (τ_{b-CRTA})] (green dashed lines), DFT-BS and renormalized band gap within CRTA [EPW-gap+DFT-BS (τ_{CRTA})] (red solid line) and renormalized band structure and band gap within CRTA [EPW-gap+EPW-BS (τ_{CRTA})] (blue). The top, second, third and bottom panels show plots of α , σ , power factor ($S^2\sigma$) and κ_e , respectively. The left and right panels are for ZrS ₂ , BiI ₃ respectively.	81
A.1	The projected DOS of Al-doped BaCu ₂ Se ₂ computed at the level of (a) Gau-PBE (b) PBE+U (4 eV) and (c) PBE+U (12 eV). The dopant atom occupies Cu ₁ -site. The VBM is set to zero in all the cases.	83
A.2	Al doped on Cu-site in (a) T ₁ and (b) T ₂ tetrahedron. T ₁ and T ₂ tetrahedra are represented by red and blue color respectively. The projected DOS of Al-doped BaCu ₂ Se ₂ computed at the level of PBE+U when Al occupies (c) Cu ₁ and (d) Cu ₂ -site. The VBM is set to zero in all the cases.	84

B.1 The mode resolved imaginary part of electron-phonon self energy for the valence (top panels (a-b)) and conduction (middle panels (c-d)) bands for the ML-ZrS₂ and ML-BiI₃ at 300 K, where contribution from various modes are shown by different colors. The largest contribution to $\text{Im}\Sigma_{n,k}$ due to optical modes is shown by red curves in each case. The vibrational patterns of optical modes at Γ point with dominant contribution to $\text{Im}\Sigma_{n,k}$ are shown for ML-ZrS₂ and ML-BiI₃ in (e-f). 87

List of Tables

3.1	The optimized lattice constants for BaCu_2Se_2 are listed. For comparison, we have mentioned the lattice constants from the previous theoretical and experimental reports.	40
3.2	The band gaps for BaCu_2Se_2 computed with PBE+U and Gau-PBE functionals. The values of band gap from previous theoretical and experimental reports are also given.	40
3.3	The optimized lattice constants for pristine and doped configurations with $(2 \times 1 \times 1)$ supercell.	41
4.1	van der Waals radius (r_{vdW}) and the C_6 coefficients for the different atomic species used in the Grimme-D2 vdW corrections. These values are taken from Ref. [2].	50
4.2	The lattice parameters (a) and binding energy per unit area (E_{BE}) of the three possible configurations of the HS- $\text{BiI}_3/\text{ZrS}_2$ obtained with PBE+vdW+SOC.	54
4.3	The band gap (E_g , in eV) of BiI_3 , ZrS_2 and the B'BC configuration of the HS obtained with PBE and Gau-PBE hybrid functionals.	57
4.4	C , m^* , E_{dp} and τ for the electrons and holes in ZrS_2 and BiI_3 monolayers and in the HS.	58
5.1	Comparison of effective masses of electrons and holes in the monolayers between the DFT-band structure and the renormalized band structure.	73
5.2	C , E_{dp} and τ for the electrons and holes in ZrS_2 and BiI_3 monolayers.	75
A.1	Bond distances in the tetrahedra T_1 and T_2 for pristine and doped configurations. All the distances are in Å.	85
B.1	Pauling electronegativity (EN) values for the different elements present in the monolayers [3]. Difference between the electronegativity (ΔEN) of the elements present in the monolayers.	86

Chapter 1

Introduction

Natural resources such as petroleum and natural gases are being exhausted rapidly over several years to fulfill domestic and industrial needs. Usage of these resources increases global warming and releases an enormous amount of heat energy as a waste. To reduce the consumption of these resources, researchers worldwide are faced with new challenges to search for alternative means of clean energy. It can be advantageous if waste heat ejected from industries or automobiles etc., can be converted into some useful form of energy. Thermoelectric materials can play a prominent role in converting waste heat into electricity.

1.1 Thermoelectric Effects

The processes through which heat can be converted into electricity or vice versa are called thermoelectric effects. While the former is called the Seebeck effect, the latter is called Peltier effect. Below we briefly describe the two.

1.1.1 Seebeck effect

If a temperature gradient (ΔT) is maintained across a junction consisting of two different electrically conducting materials joined in series but thermally connected in parallel (Fig. 1.1 (a)), then a potential difference (ΔV) is generated across the junction. This process is known Seebeck effect, and the ratio ($\Delta V / \Delta T$) is termed as Seebeck coefficient (S). Mathematically, it is expressed as:

$$S = \frac{\Delta V}{\Delta T} \quad (1.1)$$

1.1.2 Peltier effect

In this process, when an electric current is passed through the junction a temperature gradient is developed across its ends. Thus heat evolves from one end and gets absorbed at the other end of the junction (Fig. 1.1 (b)). It is the reverse of Seebeck effect. The amount of heat evolved or absorbed at the junction per unit time (\dot{Q}) is given by $\dot{Q} = \Pi \times I$, where Π is the Peltier coefficient and I is the magnitude of current. The Seebeck and Peltier effects are used for power generation and refrigeration, respectively.

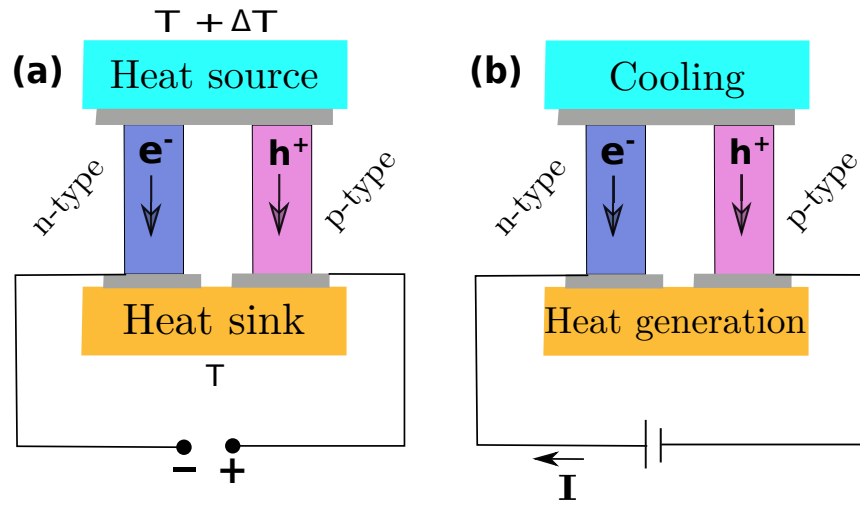


Figure 1.1: Schematic of thermocouple demonstrating (a) Seebeck effect (b) Peltier cooling.

1.2 Efficiency of thermoelectric device

The conversion efficiency (η) of a thermoelectric device is given by:

$$\eta = \left(1 - \frac{T_c}{T_h}\right) \frac{\sqrt{1 + ZT_{avg}} - 1}{\sqrt{1 + ZT_{avg}} + T_c/T_h} \quad (1.2)$$

where T_h (T_c) is the temperature of hot (cold) end and T_{avg} is the average of the temperature at the hot and cold end ($T_{avg} = (T_h + T_c)/2$). ZT is the material's figure of merit and is related to the material properties like Seebeck coefficient, electrical conductivity (σ) and thermal conductivity (κ). ZT is given by:

$$ZT = \frac{S^2 \sigma T}{\kappa} \quad (1.3)$$

Larger the value of ZT more is the value of η .

However, finding materials with considerable ZT is challenging due to the interconnect-
edness of the various physical quantities involved. For instance, S is inversely propor-
tional to doping concentration while σ increases with it. Furthermore, an increase in σ also
increases electronic conductivity (κ_e) because they are related through Wiedemann-Franz
Law. So these factors bring up great challenges to independently control ZT . Despite the
difficulties, researchers have developed various new techniques to improve the value of
 ZT for several materials. In the following sections, we briefly describe various classes of
thermoelectric materials, and then we will discuss some of the strategies employed in this
thesis to enhance ZT of a few materials.

1.3 Classes of TE materials

1.3.1 Phonon glass electron crystal based TE materials

TE material should have high electrical conductivity and low lattice thermal conductivity,
thus possessing high ZT . Materials exhibiting such properties are called “phonon glass and
an electron crystal (PGEC).” In the following, we briefly discuss a few important classes
of TE materials that possess properties similar to PGEC. Usually, such materials have
complex cage-like structures filled with heavy atoms, namely skutterudites and clathrates.

1.3.1.1 Skutterudites

Skutterudites derive their name from naturally occurring arsenic minerals (CoAs_3) found
in Skutterud, Norway, in 1845. These bulk materials have cubic crystal structures with a
space group $Im\bar{3}$ [4]. The general formula representing the unit-cell of binary skutterudites
is $\square_2\text{T}_8\text{X}_{24}$, where T denotes transition metal, X indicates pnictogen, and \square symbolizes
the voids. These voids that can be filled with alkaline-earth or rare-earth elements with
heavy atomic masses.

Within the filled skutterudites, the guest atoms act as independent oscillators giving rise
to the “rattling effect.” Since rattlers are weakly bound inside the cages formed by host
atoms, they vibrate locally with lower frequencies. These rattlers scatter the heat-carrying
normal phonon modes of lower frequencies and thus prevent the flow of heat through-

out the crystal. So, the rattling effect lessens the lattice thermal conductivity, whereas rattlers do not affect the high electrical conductivity of filled skutterudites. Thus filled skutterudites behaves as PGEC. Nolas *et al.* have demonstrated PGEC characteristics in $\text{Yb}_{0.19}\text{Co}_4\text{Sb}_{12}$ in 2000 [5].

These materials are earth-abundant and more cost-effective than other TE materials [6]. They can function at a wide range of temperatures (up to 900 K) [6]. However, the application of skutterudites is limited by their non-resistance to oxidation and sublimation of group 5 elements [7]. These materials exhibit very high ZT with suitable fillers. For example, Xun *et al.* had demonstrated ZT of 1.7 at 850 K for n-type $\text{Ba}_{0.08}\text{La}_{0.05}\text{Sb}_{0.04}\text{Co}_4\text{Sb}_{12}$ [8]. Some latest reviews by several authors on skutterudites are available elsewhere [6,9].

1.3.1.2 Clathrates

Clathrates exist in a more complex cage-like structure than skutterudites and show variation in their compositions. These materials are most commonly found in two types of structures described by general formula $\text{X}_a\text{Y}_b\text{Z}_{46-b}$ (type-I) and $\text{X}_a\text{Y}_b\text{Z}_{136-b}$ (type-II), where Y and Z are Group 3 and 4 elements that form cage-like structures to host guest atoms X from alkali or alkaline-earth metals. Type-I clathrates crystallize in cubic structure with $Pm\bar{3}n$ space group forming cage-like framework composed of 6 tetrakaidecadron and 2 dodecahedron cages per unit cell. The unit cell of these clathrates is made up of 46 tetrahedrally coordinated host atoms. In Wyckoff notation, the host atoms occupy at $6c$, $6i$ and $24k$ Wyckoff sites, whereas the 8 guest atoms occupy $6d$ and $2a$ Wyckoff sites at the center of the cages formed by tetrakaidecadron and dodecahedron, respectively.

On the other hand, type-II clathrates also possess cubic crystal structure, but with $Fd\bar{3}m$ space group. They also exist in a cage-like framework made up of 8 hexakaidecahedra and 16 dodecahedron cages per unit cell. The unit cell of clathrates type-II contains 136 tetrahedrally coordinated host atoms occupying $96g$, $32e$ and $8a$ Wyckoff positions, whereas the 24 guest atoms occupy $8b$ and $16c$ Wyckoff positions at the center of cages formed by hexakaidecahedra and dodecahedron, respectively. A detailed information on crystal structures of type-I and type-II clathrates can be found elsewhere [10, 11].

Similar to skutterudites, clathrates also possess remarkably low lattice thermal conductivity due to the rattling effect of guest atoms [12, 13]. Furthermore, these materials exhibit

comparable Seebeck coefficient and electrical conductivity relative to that of commercially used TE materials [10, 13]. As a result, a significantly high ZT (> 1) is observed for this class of materials. For example, a high $ZT \sim 1.35$ is observed in n -type $\text{Ba}_8\text{Ga}_{16}\text{Ge}_{30}$ at 900 K [13]. Some reviews on clathrates can be found elsewhere [10, 14].

1.3.2 Metal Oxides

Oxide-based TE materials are cost-effective and environment-friendly. They are chemically and thermally stable. However, this class of materials could not get much attention due to its relatively high lattice thermal conductivity [15]. However, in 1997, interest in oxide-based layered materials was kindled when Terasaki *et al.* discovered highly anisotropic NaCo_2O_4 single crystals with high in-plane power factor $\sim 50 \mu\text{WK}^{-2}\text{cm}^{-1}$, which is greater than that of Bi_2Te_3 [16]. Since then, many high-temperature (> 800 K) oxide-based TE materials, like $(\text{Ca}_2\text{CoO}_3)_{0.7}\text{CoO}_2$, $\text{Bi}_2\text{Sr}_2\text{Co}_2\text{O}_y$, and $\text{Na}_x\text{CoO}_{2-\delta}$, have been discovered with ZT around 1 [17–19]. Based on theoretical calculations, Dresselhaus *et al.* predicted that low-dimensional systems can give rise to enhanced ZT relative to their bulk counterparts [20, 21]. Following these novel routes suggested by Dresselhaus *et al.* [20, 21], the highest ZT of about 2.5 was observed for SrTiO_3 superlattice by Ohta *et al.* [22]. Further elaborative information on oxide-based TE materials is available elsewhere [23–26].

1.3.3 Half-Heusler (HH) alloys

Half Heusler alloys (XYZ) are composed of three different types of atoms, where X and Z can be transition metals, and Y is a metal or non-metal. They crystallize in cubic crystal structure with space group $F\bar{4}3m$. In the primitive unit-cell, X and Z are located at $4a$ (0, 0, 0) and $4b$ (0.5, 0.5, 0.5) Wyckoff positions forming a rock-salt crystal structure, while Y atom occupies $4c$ (0.25, 0.25, 0.25) Wyckoff position along body diagonal and leaving the $4d$ (0.75, 0.75, 0.75) Wyckoff position vacant [27].

HH has attracted immense attention from researchers due to their mechanical robustness, remarkable electronic transport properties, and thermal stability [28, 29]. These materials can provide larger output power than other state-of-art TE materials due to their higher power factors [30–32]. These materials are environment-friendly, cost-effective, and have flexible compositions [7]. Additionally, these materials can operate in temperatures rang-

ing from 600 K to 1000 K [7, 33]. There are many HH alloys with significant ZT (~ 1) values. For example, Fu *et al.* found a maximum $ZT \sim 1.1$ for p-type $\text{FeNb}_{1-x}\text{Ti}_x\text{Sb}$ at 1100 K [32]. Zhu *et al.* have reported a $ZT \sim 1.52$ for p-type TaFeSb-based HH alloys at 973 K [34]. Similarly, a peak $ZT \sim 0.9$ was obtained for n-type $\text{Nb}_{0.83}\text{CoSb}$ at 1123 K by Xia *et al.* [35]. Likewise, in a recent experimental work, Yu *et al.* obtained a $ZT \sim 1$ for n-type $\text{Hf}_{0.5}\text{Zr}_{0.5}\text{NiSn}_{0.98}\text{Sb}_{0.02}$ system [36].

Since HH alloys are composed of the lightweight elements, thus they exhibit high lattice thermal conductivity relative to that of commercially used TE materials. Heavy atoms can replace lighter ones with appropriate doping to overcome these challenges. Some in depth reviews on HH alloys are available elsewhere [33, 37–41].

1.3.4 Metal chalcogenides

The metal chalcogenides (MCs) are composed of metal and chalcogenides ($X = \text{S}, \text{Se}$ and Te). MCs are at the forefront of TE materials due to their better and more reliable performance relative to any other class of TE materials. Notably, heavy atomic mass is responsible for these materials' low lattice thermal conductivity, and thus, MCs exhibit very high $ZT > 1$. Based on the composition and crystal structure, Chao *et al.* have divided MCs into nine groups [42], and here we discuss some paramount classes of MCs as follows:

1.3.4.1 Lead chalcogenides

Lead is the most promising element in this class of TE materials due to its high earth abundance and heavy atomic mass. Lead chalcogenides can operate in mid-range temperatures (600-800 K). They exist in a rock-salt crystal structure with lead atoms inhabiting the cation sites and chalcogens populating anion sites. Amongst lead chalcogenides, in particular, PbTe has played a vital role in the field of thermoelectrics for the last five decades. The full potential of PbTe was realized in 2011 when Snyder *et al.* demonstrated the $ZT \sim 1.4$ in p -type, and n -type PbTe at 750 K [43, 44]. Furthermore, Kanishka *et al.* achieved a $ZT \sim 2.2$ (at 915 K) in p -type PbTe with maximum reduction in the lattice thermal conductivity [45].

1.3.4.2 Bismuth chalcogenides

Bismuth chalcogenides represent another exciting TE material class used widely near room temperature. In particular, Bi_2Te_3 is a layered semiconductor and narrow bandgap (160 meV) material [42]. It exists in trigonal crystal structure with space group $R\bar{3}m$, where Bi and Te layers are arranged in a ... Te-Bi-Te-Bi-Te ... manner. Bi and Te layers are bonded by robust covalent bonds, whereas Te layers interact via weak van der Waals forces along the z-axis [46]. As a result, anisotropy is observed in electronic transport properties and lattice thermal conductivity of Bi_2Te_3 . For instance, Bismuth telluride shows in-plane (cross-plane) lattice thermal conductivity of 1.5 (0.7) $\text{Wm}^{-1}\text{K}^{-1}$ [46]. In 1950, Bi_2Te_3 was used in TE refrigerators with $ZT \sim 0.6$ at 300 K [42]. Recently, a ZT for p-type $\text{Bi}_{0.5}\text{Sb}_{1.5}\text{Te}_3$ (n-type $\text{Bi}_2\text{Se}_{0.3}\text{Te}_{2.7}$) has touched 1.86 at 320 K (1.2 at 445 K) [42, 47, 48]. Moreover, Rama *et al.* observed a ZT of 2.4 (at 300 K) in $\text{Bi}_2\text{Te}_3/\text{Sb}_2\text{Te}_3$ superlattices [49].

1.3.4.3 Superionic conductors (SICs)

There is a particular class of materials called superionic conductors (SICs), which exhibits properties similar to PGEC. For example, Cu_2Se and Cu_2S are the two SICs that have played a vital role in developing TE materials. These materials exist in the low-temperature α -phase and high-temperature β -phase (so-called SICs). In the β -phase, chalcogenide atoms adopt a rigid crystal structure and offer a pathway for charge transport, whereas Cu ions move in a highly disordered fashion around the chalcogen sublattice, hindering the transport of heat [50, 51]. Therefore, when Cu ions flow liquid-like around the chalcogenide sublattice, the chalcogenide sublattice acts as the phonon-liquid and electron crystal (PLEC), basically analogous to PGEC. Thus an outstanding performance was demonstrated in p-type Cu_{2-x}Se with ZT of 1.5 at 1000 K [50]. Moreover, in 2013, Liu *et al.* had reported the highest ZT of 2.3 at 400 K in n-type Cu_2Se . [51].

1.3.4.4 Layered structure materials

Layered structure materials are divided into three categories: Ternary ACrX_2 layered structures, Bi-O-X systems, and transition metal dichalcogenides (TMDCs) [42]. Here we focus on TMDCs as follows:

TMDCs

These materials possess trigonal crystal structure with space group $P\bar{3}m1$. In particular,

bulk TiS_2 , in its most stable form (1T- TiS_2), crystallizes in a layered structure. Each layer is formed by a Ti sublayer sandwiched between two S sublayers. Thermoelectric properties of $\text{Ti}_{1+x}\text{S}_2$ have been investigated by intercalating the excess Ti atoms into the layers, and transport coefficients are reported with increasing with the content of Ti atoms [52]. Moreover, thermoelectric properties of Cu_xTiS_2 in-plane and cross-plane have been inspected by Guilmeau *et al.* [53]. Apart from TiS_2 , many other TMDCs have been investigated, such as MoS_2 [54, 55], WSe_2 [54], ZrS_2 [56], TiS_3 [57], etc.

1.3.4.5 Other metal chalcogenides

Other metal chalcogenides are divided into Ga-Te systems and Non-layered transition metals chalcogenides [42]. The latter is discussed as follows:

Non-layered transition metals chalcogenides

Apart from layered TMDCs, many TMDCs exist in non-layered crystal structures as exemplified by CeSe_2 , Ce_3Te_4 , FeS_2 , MnTe , and BaCu_2Se_2 , etc. These materials possess promising TE properties either due to their band structure stemming from distinctive properties of transition metals or complex crystal structure [42]. For instance, Na doping on Ba-site increases the electrical conductivity by two orders of magnitude, giving rise to a $ZT \sim 1$ at 773 K in BaCu_2Se_2 [58].

The rest of the classes belonging to MCs are discussed in detail by Chao *et al.* [42] and Priyanka Jood and Michihiro Ohta [59].

1.3.5 Metal Halides

Metal halides are a new class of materials defined by a chemical formula MX_3 , where M denotes a metal atom and X indicates a halide ion. Recently, great interest is arisen in studying physical properties of metal halides [60–64]. Recently, the family of MX_3 (where $\text{M}=\text{Sc}$, Y , As , Sb , and Bi) is shown to be a semiconductor by Liu *et al.* [64]. Amongst them, the Bismuth triiodide (BiI_3) is notably fascinating due to its Mexican hat-like valence bands that might result in a high Seebeck coefficient [65]. Moreover, BiI_3 is predicted to possess an ultralow thermal conductivity [66].

There is an endless list of many more classes of TE materials like silicon-based, organic, and spinels TE materials [7, 67, 68]. In this thesis we have chosen ZrS_2 , BaCu_2Se_2 , and

BiI_3 from layered and non-layered transition metal chalcogenides and metal halides, respectively. The motivation to select each one of them is discussed in respective chapters.

1.4 Strategies to enhance ZT

From Eqn. 1.3 we note that the lattice contribution to the thermal conductivity (κ_L) is independent of the other material parameters that depend on the electronic properties. This suggests two major strategies that can be employed to improve ZT of thermoelectric materials: reduce the κ_L and enhance $S^2\sigma$. Methods to reduce κ_L are discussed elsewhere. [69] In the following, we briefly describe two methods that have been employed in this thesis to enhance the power factor.

1.4.1 Resonant doping

It is a band engineering technique used to improve the ZT by increasing the values of S . The phenomenon of resonant levels and their influence on transport coefficients are treated as follows.

1.4.1.1 Resonant levels

Typically in doped semiconductors, the impurity states are in the band gap and carriers from these states can be excited to conduction or valence bands by providing activation energy (E_D). However, when defect state overlaps with the electronic states of parent crystal for which E_D is negative, these states are called resonant levels (RLs) or also labeled as “virtual bound states” as shown in Fig. 1.2 (a). The term “Resonant levels (RLs)” was first introduced for metals in solid-state physics [70]. RLs refer to impurity states that overlap with the energy spectrum of the host material. So all the impurity states in metals and semi-metals can be assigned as RLs.

As the energy of defect state coincides with that of parent electronic state, so they resonate to create two new states with slightly different energies. Two newly-formed extended states further resonate with other extended states of corresponding energies and so on. As a result, resonant state acquires finite width Γ and produces a distortion in electronic density of states of parent crystal (Fig. 1.2 (b)).

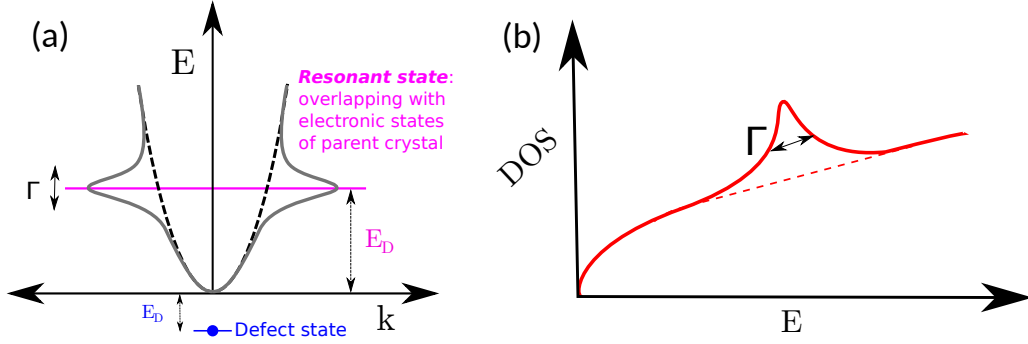


Figure 1.2: (a) Schematic diagram of a conduction band with defect state (blue) and a resonant state (pink) and (b) resonant state producing distortion in density of states (DOS).

1.4.1.2 Resonant doping and thermoelectricity

The RLs affect the transport properties in two ways : by induced distortion in density of states (DOS) and through resonant scattering.

Distortion in DOS

The Seebeck coefficient within Mott picture is given as follows [71]:

$$S = \frac{k_B}{q} \frac{1}{\sigma_{\alpha,\beta}} \int_0^\infty \sigma_{E,\alpha,\beta}(E) \left(\frac{E - E_F}{k_B T} \right) \left(- \frac{\partial f}{\partial E} \right) dE \quad (1.4)$$

where f denotes Fermi-Dirac occupation, $\sigma_{\alpha,\beta}$ is conductivity tensor and zero of energy is set at the band edge. Notice that Eq. (1.4) can be applied only to a material having Fermi surface composed of a single pocket.

S can be approximated using Bethe-Sommerfeld expansion for a single parabolic band as follows [71]:

$$\begin{aligned} S &= \frac{\pi^2 k_B}{3} \frac{1}{q} (k_B T) \left[\frac{1}{n(E)} \frac{dn(E)}{dE} + \frac{1}{\mu(E)} \frac{d\mu(E)}{dE} \right] \\ &= \frac{\pi^2 k_B}{3} \frac{1}{q} (k_B T) \left[\frac{g(E)}{n(E)} + \frac{1}{\mu(E)} \frac{d\mu(E)}{dE} \right] \end{aligned} \quad (1.5)$$

where k_B is Boltzmann constant, μ is mobility of charge carriers, $g(E)$ is DOS and $n(E) = \int g(E) dE$.

Eq. 1.5 suggests that S can be improved through two mechanisms : (i) local increase in DOS can increase $g(E)$ (ii) an increase in $\frac{d\mu(E)}{dE}$. For example, $\mu(E)$ can decrease due to scattering mechanism between conduction electrons and resonant state that has strong de-

pendence on the energy of charge carriers. This is called “resonant scattering”. However, resonant scattering is more prominent at low temperatures. The increase in $g(E)$ term, due to distortion produced in DOS (Fig. 1.2 (b)), has a prominent influence and is responsible for the enhancement of thermoelectric properties of the materials. Lately, Heremans *et al.* have demonstrated that ZT of p-type PbTe can be increased to 1.5 at 773K through resonant doping [72]. We have employed this approach to enhance transport properties of BaCu₂Se₂ in **Chapter 3** of this thesis.

1.4.2 Reduced dimensionality

Properties of the materials can be boosted by increasing the DOS as suggested by the first term in Eq. 1.5. A significant enhancement in DOS can be achieved when dimensions of the materials are reduced and approach to nanometers length scales. This remarkable strategy was proposed by Dresselhaus *et al.* to design thermoelectric materials with enhanced ZT by reducing dimensionality. [20, 21] Theoretically, it was shown that Bi₂Te₃ with quantum well structure might possess great potential to attain a significant ZT [20]. The improvement in ZT mainly originates from enhancement in S due to increased DOS when the dimensionality of the materials is reduced. These predictions have been a great insight to develop various new routes such as nanostructuring to improve the power factor. We use this strategy to form a novel van der Waals heterostructure (HS) of BiI₃ and ZrS₂ monolayers in **Chapter 4** of this thesis.

1.5 Thesis outline

The rest of the thesis is arranged as follows.

Chapter 2 includes a description of density functional theory (DFT) used to calculate the electronic structure of the materials. Additionally, it has a brief description of the semiclassical Boltzmann transport theory (BTT) that is used to calculate the transport coefficients.

Further, this thesis is partitioned into two parts.

Part 1

In this part we use conventional computational methods to study the effect of structural

modifications on transport properties of bulk and layered materials.

Cu based chalcogenides are emerging to be promising thermoelectric materials. To identify resonant dopants to enhance Seebeck coefficient and thereby ZT of α -BaCu₂Se₂, we have studied the effect of doping, with Boron group of elements, on the electronic and transport properties of α -BaCu₂Se₂. The results of our study are presented in **Chapter 3**.

In **Chapter 4** we present the study of electronic and transport properties of a heterostructure of BiI₃ and ZrS₂ monolayers. Subtle modifications are observed in the electronic band structure of the heterostructure compared to individual layers that also affect transport properties. We have calculated the relaxation time of charge carriers in the parent compound and the heterostructure based on deformation potential theory. These are further used to transport coefficients.

Part 2

In this part we critically examine the validation of some approximations that are typically made in the calculations. It is important to compute carrier relaxation time to predict the transport properties of novel materials. Usually, this is computed using deformation potential theory where only coupling of electrons/holes and acoustic phonons are considered.

In **Chapter 5**, we investigate the effect of electron-phonon interactions on the electronic and thermoelectric properties of ZrS₂ and BiI₃ monolayers. The relaxation time of charge carriers is computed for these materials incorporating the contributions of the optical modes. Further relaxation time is also computed based on deformation potential theory. Comparison between the two is very insightful from the perspective of computational material design.

Chapter 2

Theoretical methods

The physical properties of a material can be, in principle, calculated from first principles by solving the many-body Schrödinger equation (SE). However, it is not possible to do so practically thereby necessitating the usage of some approximations. In this chapter we briefly describe the challenges to solve the many-body SE and describe one of the methodologies, namely density functional theory, developed to overcome the challenges to solve the SE. We have also briefly discussed the theory of electron-phonon interactions in solids from first principles. Further, this thesis also includes the computation of transport properties, we have briefly described the semiclassical Boltzmann transport theory.

2.1 Many body Schrödinger equation

Matter is composed of N nuclei (positively charged) and n electrons (negatively charged) interacting with each other via Coulomb forces. Time-independent Schrödinger equation (TISE) for this system is given by

$$\hat{H}_{tot}\Psi(\mathbf{R}, \mathbf{r}) = E_{tot}\Psi(\mathbf{R}, \mathbf{r}) \quad (2.1)$$

where $\Psi(\mathbf{R}, \mathbf{r})$ denotes many-body wavefunction which depends on the position of all the nuclei $\{\mathbf{R}\}$ and electrons $\{\mathbf{r}\}$ constituting the system. Hamiltonian (\hat{H}_{tot}) of the system is

given by

$$\begin{aligned} \hat{H}_{tot} = & - \sum_{I=1}^N \frac{\hbar^2}{2M_I} \nabla_I^2 - \sum_{i=1}^n \frac{\hbar^2}{2m_e} \nabla_i^2 + \frac{e^2}{2} \frac{1}{4\pi\epsilon_0} \sum_{I=1}^N \sum_{\substack{J=1, \\ I \neq J}}^N \frac{z_I z_J}{|\mathbf{R}_I - \mathbf{R}_J|} \\ & + \frac{e^2}{2} \frac{1}{4\pi\epsilon_0} \sum_{i=1}^n \sum_{\substack{j=1, \\ i \neq j}}^n \frac{1}{|\mathbf{r}_i - \mathbf{r}_j|} - \frac{e^2}{4\pi\epsilon_0} \sum_{I=1}^N \sum_{i=1}^n \frac{z_I}{|\mathbf{R}_I - \mathbf{r}_i|}, \end{aligned} \quad (2.2)$$

where z_I and e denote the charges of I^{th} nuclei and an electron, respectively. M_I and m_e indicate masses of I^{th} nuclei and electron respectively. In Eq. (2.2), first two terms refer to the kinetic energy (K.E.) of the nuclei and electrons respectively. The 3rd, 4th and 5th terms in Eq. (2.2) indicate nuclei-nuclei, electron-electron and nuclei-electron Coulomb interactions, respectively. In principle, all the information about the system can be obtained by solving the TISE. However, main difficulty to solve Eq. (2.1) is posed by the non-local potential terms in Eq. (2.2). Hence some approximations must be invoked to solve it.

2.2 Adiabatic or Born-Oppenheimer approximation

Within this approximation, it is assumed that decoupling of electronic and nuclear motion is possible. The mass of a nucleus is enormously greater than an electron ($\frac{m_{proton}}{m_{electron}} \approx 1836$). Thus the motion of nuclei is very slow compared to electrons. In other words, timescale associated with the motion of electrons is quite small relative to the nuclei ($t_{nuclei} \gg t_{electrons}$). One can safely assume that the electrons will instantly respond to the motion of nuclei with hardly any change in their the electronic states. It is the Born-Oppenheimer (BO) approximation. As a result $\Psi(\mathbf{R}, \mathbf{r})$ can be decoupled as a product of nuclear wave function ($\Phi_N(\mathbf{R})$) and electronic wavefunction ($\psi(\mathbf{R}; \mathbf{r})$), where $\psi(\mathbf{R}; \mathbf{r})$ has only parametric dependence on the nuclear coordinates. Mathematically,

$$\Psi(\mathbf{R}, \mathbf{r}) = \sum_n \Phi_n(\mathbf{R}) \psi_n(\mathbf{R}; \mathbf{r}) \quad (2.3)$$

Hence for a given value of $\{\mathbf{R}\}$ we write the electronic Schrödinger equation (SE) using Eq. (2.3) as follows:

$$\left(-\frac{\hbar^2}{2m} \sum_{i=1}^n \nabla_i^2 + \frac{e^2}{2} \frac{1}{4\pi\epsilon_0} \sum_{I=1}^N \sum_{\substack{J=1, \\ I \neq J}}^N \frac{z_I z_J}{|\mathbf{R}_I - \mathbf{R}_J|} + \frac{e^2}{2} \frac{1}{4\pi\epsilon_0} \sum_{i=1}^n \sum_{\substack{j=1, \\ i \neq j}}^n \frac{1}{|\mathbf{r}_i - \mathbf{r}_j|} - \frac{e^2}{4\pi\epsilon_0} \sum_{I=1}^N \sum_{i=1}^n \frac{z_I}{|\mathbf{R}_I - \mathbf{r}_i|} \right) \psi_n(\mathbf{R}; \mathbf{r}) = E_n^{ele}(\mathbf{R}) \psi_n(\mathbf{R}; \mathbf{r}) \quad (2.4)$$

where the motion of nuclei can be ignored. However, Eq. (2.4) still has the non-local electron-electron (two-body) interaction term. Hence analytic solution of electronic SE is not possible and some more approximations need to be invoked.

2.3 Density functional theory

Hohenberg and Kohn (HK) proposed to develop density functional theory (DFT) as an exact theory of many-body systems, which forms the basis of present day electronic structure theory. They came up with an alternative approach to use charge density ($n(\mathbf{r})$) as the basic variable rather than the many-body wavefunction. Since $n(\mathbf{r})$ can greatly diminish the complexity of the many-body problem by shrinking the degree of freedom from $3n$ variables to 3 (n being the number of electrons). DFT is applicable to any system of n interacting electrons moving in an external potential ($V_{ext}(\mathbf{r})$) due to clamped nuclei. [73] The Hamiltonian for a system of interacting electrons is given by (using Hartree atomic units; $\hbar = m = e = 4\pi\epsilon_0 = 1$),

$$\hat{H}_{int} = -\sum_i \frac{\nabla_i^2}{2} + \sum_i V_{ext}(\mathbf{r}_i) + \frac{1}{2} \sum_{i \neq j} \frac{1}{|\mathbf{r}_i - \mathbf{r}_j|}. \quad (2.5)$$

Following two theorems pave the way for DFT [74]

2.3.1 Hohenberg-Kohn theorems

The following theorems are given by P. Hohenberg and W. Kohn [73, 75].

Theorem 1: For any system of interacting particles in an external potential $V_{ext}(\mathbf{r})$, the potential $V_{ext}(\mathbf{r})$ is determined uniquely, except for a constant, by the ground state particle

density $n_0(\mathbf{r})$.

Theorem 2: A *universal functional* for the energy $E[n]$ in terms of the density $n(\mathbf{r})$ can be defined, valid for any external potential $V_{\text{ext}}(\mathbf{r})$. For any particular $V_{\text{ext}}(\mathbf{r})$, the exact ground state energy of the system is the global minimum value of this functional, and the density $n(\mathbf{r})$ that minimizes the functional is the exact ground state density $n_0(\mathbf{r})$.

The first theorem establishes that two distinct external potentials can not give rise to the indistinguishable ground state (GS) charge density ($n_0(\mathbf{r})$). Specifically, V_{ext} is known uniquely through $n_0(\mathbf{r})$.

$$n_0(\mathbf{r}) \longrightarrow V_{\text{ext}}(\mathbf{r}). \quad (2.6)$$

The second theorem tells that $E[n]$ can be minimized with respect to (w.r.t) variations in $n(\mathbf{r})$. The value of density that minimizes $E[n]$ gives the GS density $n_0(\mathbf{r})$ and the corresponding value of energy is the GS energy (E_{min}). In summary, if $n_0(\mathbf{r})$ is specified, all properties can be uniquely characterized.

If $V_{\text{ext}}(\mathbf{r})$ is given, then HK energy functional (E_{HK}) is written as:

$$E_{HK}[n] = F_{HK}[n] + \int V_{\text{ext}}(\mathbf{r})n(\mathbf{r})d\mathbf{r}, \quad (2.7)$$

where $F_{HK}[n]$, being the sum of the K.E. of the electrons ($T[n]$) and the electron-electron interaction ($E_{ee}[n]$) terms, can be written as:

$$F_{HK}[n] = T[n] + E_{ee}[n]. \quad (2.8)$$

If $F_{HK}[n]$ is given, it implies the information of the GS properties is known for the system. HK theorem predicts existence of a universal functional form of $F_{HK}[n]$ that could give all the GS properties of the system. However, it does not give a recipe to calculate it. In the next section, we have briefly discussed a practical way to find $F_{HK}[n]$ suggested by Kohn and Sham.

2.3.2 Kohn and Sham Approach

By mid 1960, Kohn and Sham addressed the problem to tackle unknown functional ($F_{HK}[n]$) [76]. They replaced the difficult many-body system with interacting electrons by a fictitious system of independent (non-interacting) electrons for the sake of numerical treatment. Kohn and Sham's ansatz is as follows [73]:

- The GS density of the fictitious system is same as that of actual system.
- The calculations can be performed on a fictitious independent-particle systems defined by Hamiltonian (\hat{H}_s) for single electron having the K.E. term and subjected to an effective local potential ($V_{\text{eff}}(\mathbf{r})$). (Here we adopt Hartree atomic units $\hbar = m = e = 4\pi\epsilon_0 = 1$).

$$\hat{H}_s = -\frac{\nabla^2}{2} + V_{\text{eff}}(\mathbf{r}) \quad (2.9)$$

Using above two ansatz, the KS suggested to rewrite expression of $F_{HK}[n]$ functional in the following manner:

$$F_{KS}[n] = T_s[n] + E_H[n] + E_{XC}[n], \quad (2.10)$$

where $T_s[n]$ denotes the ground state K.E. of non-interacting electrons of the supplementary system and is written as:

$$T_s[n] = \frac{1}{2} \sum_i \int |\nabla \psi_i(\mathbf{r})|^2 d\mathbf{r}. \quad (2.11)$$

Notice that, this is not equal to the K.E. of interacting system ($T[n]$). $E_H[n]$ denotes the Hartree energy given by

$$E_H[n] = \frac{1}{2} \int \int \frac{n(\mathbf{r})n(\mathbf{r}')}{|\mathbf{r} - \mathbf{r}'|} d\mathbf{r}d\mathbf{r}', \quad (2.12)$$

So, $E_{KS}[n]$ can be expressed as:

$$E_{KS}[n] = F_{KS}[n] + \int n(\mathbf{r})V_{\text{ext}}(\mathbf{r})d\mathbf{r}. \quad (2.13)$$

KS equations (2.17) for a system of independent electrons moving in local effective po-

tential ($V_{KS}(\mathbf{r})$) can be derived by the minimizing $E_{KS}[n]$. This property is known as ‘‘Hohenberg-Kohn variational principle’’ and can be written as follows:

$$\left. \frac{\delta E_{KS}[n]}{\delta n} \right|_{n_0} = 0 \quad (2.14)$$

The functional form of effective KS potential for a system of non-interacting electrons is the following:

$$V_{KS}(\mathbf{r}) = V_{\text{ext}}(\mathbf{r}) + \int \frac{n(\mathbf{r}')}{|\mathbf{r} - \mathbf{r}'|} d\mathbf{r}' + V_{XC}(\mathbf{r}), \quad (2.15)$$

where the 2^{nd} term in the R.H.S is the Hartree potential (V_H) and V_{XC} in the 3^{rd} term denotes exchange-correlation potential. The exchange-correlation potential can be expressed as the functional derivative of E_{XC} w.r.t $n(\mathbf{r})$.

$$V_{XC}(\mathbf{r}) \equiv \frac{\delta E_{XC}}{\delta n(\mathbf{r})}, \quad (2.16)$$

Thus, if we know V_{KS} (local effective potential), we can solve the following set of single electron *Kohn-Sham equations* and obtain information of GS of the system of interacting electrons:

$$\left(-\frac{1}{2} \nabla^2 + V_{KS}(\mathbf{r}) \right) \psi_i(\mathbf{r}) = \epsilon_i \psi_i(\mathbf{r}). \quad (2.17)$$

where, $\psi_i(\mathbf{r})$ denotes Kohn-Sham orbitals which are related to $n(\mathbf{r})$ as follows:

$$n(\mathbf{r}) = \sum_{i=1}^n |\psi_i(\mathbf{r})|^2. \quad (2.18)$$

All the GS properties of the system can be determined by solving the set of n KS equations (2.17). The computational strategy to solve (2.17) self consistently is demonstrated in Fig. 2.1.

2.3.3 Exchange and correlation

In previous section, we found that the problem of finding $F[n]$ for a system of interacting particles was boiled down to a system of non-interacting particles by introducing the exchange-correlation energy E_{XC} , which is a sum of exchange (E_X) and correlation (E_C) energies. The exchange interaction essentially originates from Pauli’s exclusion principle,

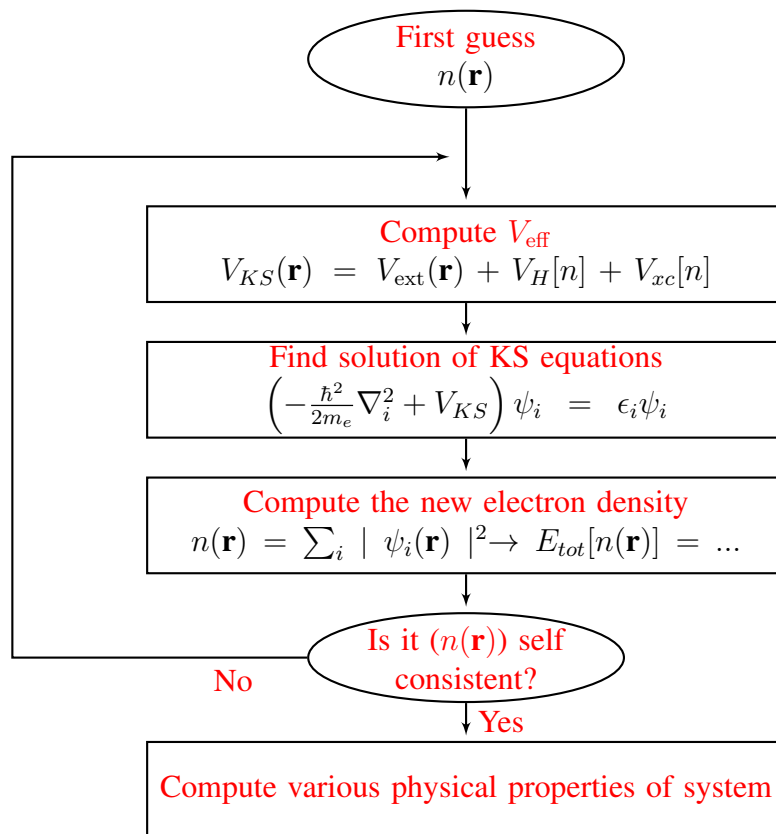


Figure 2.1: KS equations can be solved as illustrated by self consistent cycle.

which demands a spatial separation between the electrons having the same spin entering in the same quantum state and thus reducing the Coulomb repulsion. This reduction in energy is known as the exchange energy. The correlation effect comes into play when two electrons with opposite spins are also separated spatially. It further reduces the Coulomb repulsion but at the price of increase in K.E. of electrons. This reduction in energy is called correlation energy. We can incorporate such many-body effects of interacting electrons into the calculations via the exchange-correlation functional. The expression of exchange-correlation energy is given by,

$$E_{XC}[n] = \int n(\mathbf{r})\epsilon_{XC}([n](\mathbf{r}))d\mathbf{r}, \quad (2.19)$$

where, $\epsilon_{XC}([n](\mathbf{r}))$ denotes the energy density at \mathbf{r} which depends on $n(\mathbf{r})$ in the vicinity of point \mathbf{r} . So far, the functional form of $\epsilon_{XC}(n(\mathbf{r}))$ has not been discovered and thus approximated. The most commonly used approximations are discussed as follows.

2.3.3.1 Local density approximation (LDA)

In LDA, the exchange-correlation energy functional is constructed using the local electron density at point \mathbf{r} in space. The exchange-correction energy is written as:

$$E_{XC}^{LDA} = \int n(\mathbf{r})\epsilon_{XC}^{hom}(n(\mathbf{r}))d^3\mathbf{r} \quad (2.20)$$

where $\epsilon_{xc}^{hom}(n(\mathbf{r}))$ denotes exchange-correlation energy per particle for a homogeneous electron gas with density $n(\mathbf{r})$ at a point \mathbf{r} . LDA provides exact functional form of exchange-correlation energy for homogeneous electron gas and thus it performs splendidly for systems whose electron density vary slowly. Hence properties of weakly correlated systems can be predicted with reasonable accuracy using LDA.

2.3.3.2 Generalized gradient approximation (GGA)

In GGA, the inhomogeneity of electronic density of system is plugged through the magnitude of gradient of the electron density ($|\nabla n(r)|$) in company with local electron density

and the E_{XC}^{GGA} is given by:

$$E_{XC}^{GGA} = \int n(\mathbf{r}) \epsilon_{XC}(n(\mathbf{r}), |\nabla n(\mathbf{r})|) d^3\mathbf{r} \quad (2.21)$$

Various approximations of GGA functional are available, for e.g., Becke (B88) [77], Perdew and Wang (PW91) [78] etc. In this thesis, we employ GGA functional parameterized by Perdew, Burke and Ernzerhof (PBE) as it provides better description of many-body electron system than LDA [79].

2.4 Periodic Supercells

So far it was shown that many-body problem can be replaced by single electron SE equation for non-interacting particles subjected to V_{KS} . However, two intimidating challenges are lurking here: one is to solve KS equations for infinite number of independent electrons moving in V_{ext} due to infinite number of nuclei and the second challenge is how to use intractably large basis sets while expanding each of the wavefunction. In the following section we describe how periodic nature of crystals can be taken into account to resolve both the difficulties.

2.4.1 Bloch's theorem

It follows from Bloch's theorem that electronic wave function can be represented as.

$$\psi_i(r) = e^{i\mathbf{k}\cdot\mathbf{r}} u_i(r) \quad (2.22)$$

where $u_i(r)$ is the periodic function (cell-periodic part) that has same periodicity as that of the crystal. This periodic function is expanded with a discrete basis set of plane waves.

$$u_i(r) = \frac{1}{V} \sum_{\mathbf{G}} C_{\mathbf{i},\mathbf{G}} e^{i\mathbf{r}\cdot\mathbf{G}} \quad (2.23)$$

where \mathbf{G} indicates the reciprocal lattice vector (with $\mathbf{G}\cdot\mathbf{T} = 2\pi\mathbf{p}$, where \mathbf{T} is the translation lattice vector in real space and \mathbf{p} is an integer.) Using above two equation, we can expand

ψ_i as the sum of plane waves as shown below.

$$\psi_i(r) = \frac{1}{V} \sum_{\mathbf{G}} C_{\mathbf{i},\mathbf{k}+\mathbf{G}} e^{i(\mathbf{k}+\mathbf{G})\cdot\mathbf{r}} \quad (2.24)$$

First challenge is tackled by utilizing periodic property of Bloch functions and thus wavefunctions contained within a primitive unit cell are determined instead of finding wavefunctions for infinite number of electrons.

Moreover, we infer from above equation that infinite number of plane waves are required to expand the Bloch wavefunction. Customarily, the contribution of plane waves with small K.E. ($\frac{\hbar^2}{2m} |\mathbf{k}+\mathbf{G}|^2$) is relevant. So we neglect the chunk of plane waves with large values of \mathbf{G} and truncate the basis set at a certain cutoff energy (E_{cut}), which is given by:

$$\frac{\hbar^2 |\mathbf{k}+\mathbf{G}|^2}{2m} \leq \frac{\hbar^2 \mathbf{G}_{cut}^2}{2m} = E_{cut} \quad (2.25)$$

Then the infinite sum becomes

$$\psi_i(r) = \frac{1}{V} \sum_{|\mathbf{k}+\mathbf{G}| \leq \mathbf{G}_{cut}} C_{\mathbf{i},\mathbf{k}+\mathbf{G}} e^{i(\mathbf{k}+\mathbf{G})\cdot\mathbf{r}} \quad (2.26)$$

Furthermore the value of E_{cut} can be chosen by examining the convergence of the total energy. This approach helps us to overcome the second difficulty.

2.4.2 k -point sampling

To compute physical quantities like total energy one needs to perform numerical integrations using a set of infinite number of k -points to sample the irreducible Brillouin zone (BZ). In practice we can only perform calculations with a few k -points by selecting special k -points in BZ. In this thesis, we followed a method given by Monkhorst *et al.* [80] to generate of a finite grid of k -points. Using this method, one can generate k -points spaced uniformly in the BZ.

$$\mathbf{k}_j = x_{1j}\mathbf{b}_1 + x_{2j}\mathbf{b}_2 + x_{3j}\mathbf{b}_3 \quad (2.27)$$

where \mathbf{b}_i denotes the reciprocal lattice vector, and

$$x_{ij} = \frac{(2j - q - 1)}{2q}, j = 1, 2, 3, \dots, q \quad (2.28)$$

where q is an integer which determines the size of set of k -points.

2.4.3 Pseudopotentials

The properties of the crystals are primarily governed by the valence electrons of constituent atoms. The core electrons do not take part in bond formation, while valence electrons actively do so. Thus the computational cost can be reduced by neglecting the core electrons. In pseudopotential approximation, the actual potential felt by the valence electrons can be replaced with a weak potential screened by the core electrons. So one replaces V_{ext} in KS equations by the pseudopotential (V_{pseudo}). Additionally, the rapidly oscillating true wavefunction in the core region requires large number of plane waves to expand it. To rectify this problem true wave function is replaced with ψ_{pseudo} which behaves smoothly in the core region (Fig. 2.2) [1]. From the perspective of the computational cost, this approximation reduces the size of the basis set since the valence electron wavefunctions do not have the nodes and sharp peaks and few Fourier modes are needed to represent this wavefunction.

Two types of pseudopotentials are used in plane wave electronic structure calculations: norm-conserving and ultrasoft pseudopotentials. Two condition are obeyed in norm-conserving pseudopotentials: (1) the valence electron and pseudo wavefunction should coincide beyond a cutoff radius (labeled as r_c) and (2) norm of the pseudo wavefunction should match with that of the valence wavefunction below r_c [81]. In the ultrasoft pseudopotentials, the norm-conserving condition is relaxed which reduces the size of basis set [82].

2.5 Electron-phonon interactions

Frenkel coined the term “phonon” in 1932 to replace the “elastic waves.” The interaction of electrons with the elastic waves of the lattice is termed electron-phonon interactions (EPIs) [83]. Electron-phonon interactions lead to many physical phenomena like superconductivity, and temperature-dependence of electrical conductivity of materials, etc. This section briefly describes the history of electron-phonon interactions and then discusses how to compute it from the first principles. Furthermore, we will discuss the

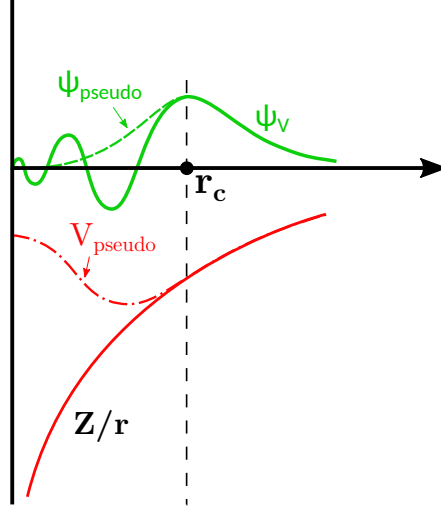


Figure 2.2: Schematic demonstration of all-electron (solid red lines) and pseudo-electron potential (dashed red lines) and corresponding wavefunctions (green curves). All-electron and pseudopotential are coincide beyond cut-off radius (r_c). (Reprinted with permission from ref. [1]. Copyright ©1992, American Physical Society)

electron self-energies useful for computing the carriers' relaxation time and band structure renormalization.

2.5.1 History of the electron-phonon interactions

The Hamiltonian of a coupled electron-phonon system is given by [84]

$$\hat{H} = \hat{H}_e + \hat{H}_p + \hat{H}_{ep} + \hat{H}_{ep}^{(2)} \quad (2.29)$$

where

$$\hat{H}_e = \sum_{n\mathbf{k}} \epsilon_{n\mathbf{k}} \hat{c}_{n\mathbf{k}}^\dagger \hat{c}_{n\mathbf{k}} \quad (2.30)$$

$$\hat{H}_p = \sum_{\mathbf{q}\nu} \hbar\omega_{\mathbf{q}\nu} (\hat{a}_{\mathbf{q}\nu}^\dagger \hat{a}_{\mathbf{q}\nu} + \frac{1}{2}) \quad (2.31)$$

$$\hat{H}_{ep} = N_p^{-1/2} \sum_{\substack{\mathbf{k}, \mathbf{q} \\ mn\nu}} g_{mn\nu}(\mathbf{k}, \mathbf{q}) \hat{c}_{m\mathbf{k}+\mathbf{q}}^\dagger \hat{c}_{n\mathbf{k}} (\hat{a}_{\mathbf{q}\nu} + \hat{a}_{-\mathbf{q}\nu}^\dagger) \quad (2.32)$$

$$\hat{H}_{ep}^{(2)} = N_p^{-1} \sum_{\substack{\mathbf{k}, \mathbf{q}, \mathbf{q}' \\ mn\nu\nu'}} g_{mn\nu\nu'}^{\text{DW}}(\mathbf{k}, \mathbf{q}, \mathbf{q}') \hat{c}_{m\mathbf{k}+\mathbf{q}+\mathbf{q}'}^\dagger \hat{c}_{n\mathbf{k}} (\hat{a}_{\mathbf{q}\nu} + \hat{a}_{-\mathbf{q}\nu}^\dagger) (\hat{a}_{\mathbf{q}'\nu'} + \hat{a}_{-\mathbf{q}'\nu'}^\dagger) \quad (2.33)$$

The first and second terms, in Eqn. 2.29, describe the electron and phonon subsystems

expressed within the formalism of the second quantization. The third and fourth terms represent the electron-phonon interactions to the first and second order in atomic displacement, respectively. Here $\epsilon_{n\mathbf{k}}$ represents the electron eigenvalue with wavevector \mathbf{k} and band n . $\omega_{\mathbf{q}\nu}$ indicates the frequency of a phonon with wavevector \mathbf{q} and mode ν . $\hat{c}_{n\mathbf{k}}^\dagger$ and $\hat{c}_{n\mathbf{k}}$ ($\hat{a}_{\mathbf{q}\nu}^\dagger$ and $\hat{a}_{\mathbf{q}\nu}$) denote the fermionic (bosonic) creation and annihilation operators, respectively. Here N_p represents the number of unit cells in a periodic supercell. $g_{mn\nu}(\mathbf{k}, \mathbf{q})$ and $g_{mn\nu\nu'}^{\text{DW}}(\mathbf{k}, \mathbf{q}, \mathbf{q}')$ quantify the strength of electron-phonon interactions.

The entire history of EPIs revolves around determining the parameters entering the Eqn. 2.29. The subsequent sections discuss the early and present approaches to estimate these parameters.

2.5.1.1 Metals

In early approaches, the free electron gas model ($\epsilon_{n,\mathbf{k}} = \frac{\hbar^2 k^2}{2m_e} - E_F$, where E_F is Fermi energy) described the electronic excitation in Eqn 2.29, while the Debye model ($\omega_{\mathbf{q}\nu} = \mathcal{V}_s |\mathbf{q}|$, \mathcal{V}_s indicates the speed of sound inside the medium) described the lattice vibrations as acoustic waves. These approximations worked reasonably well for elemental, noble and monovalent alkali metals. However, it was more difficult to specify reasonable approximations to estimate the EP matrix elements.

In 1929, Bloch provided the first expression for the EP matrix element, which represents the scattering of the electronic state $|\mathbf{k}\rangle$ to $|\mathbf{k}+\mathbf{q}\rangle$ through an acoustic phonon (with frequency $\omega_{\mathbf{q}\nu}$) and defined by [85]

$$g_{mn,\nu}(\mathbf{k}, \mathbf{q}) = -i \sqrt{\frac{\hbar}{2N_p M_\kappa \omega_{\mathbf{q}\nu}}} \mathbf{q} \cdot \mathbf{e}_{\kappa\nu}(\mathbf{q}) V_\kappa(\mathbf{q}) \quad (2.34)$$

where M_κ denotes the mass of the κ^{th} nucleus, and polarization vector of the acoustic wave is indicated by $\mathbf{e}_{\kappa\nu}(\mathbf{q})$ associated with the wavevector \mathbf{q} and mode ν . In 1929, Bloch replaced $V_\kappa(\mathbf{q})$ with a unit-cell averaged effective potential V_0 experienced by the electrons inside the medium [85]. For a continuously deformable medium, Bloch derived an expression for $V_0 = \frac{\hbar^2}{16m_e a_0^2}$ (where a_0 is Bohr radius), which was useful to understand EPIs in monovalent metals.

2.5.1.2 Semiconductors

In 1950, Bardeen and Shockley developed a “deformation-potential” theory to tackle EPIs in non-polar semiconductors [86]. Their theory assumes that local deformations caused by the long-wavelength acoustic waves are identical to those in a homogeneously deformed crystal. Since the charge carriers are generally trapped within the narrow energy window near the band extrema in the semiconductors; therefore, it was anticipated that the appreciable contribution to EPIs might arise due to the long-wavelength acoustic phonons ($\mathbf{q} \rightarrow 0$). Furthermore, a system’s elastic constant is associated with acoustic phonons.

Using the effective mass approximation, Bardeen and Shockley established that the effective potential (V_0) in Eqn. 2.34 can be described by the deformation potential constant (E_{dp}) of the system and is given by

$$V_0 \longrightarrow E_{dp} = \frac{\partial \epsilon_{n,\mathbf{k}}}{\partial \delta} \quad (2.35)$$

Here δ is the strain on the system and $\epsilon_{n,\mathbf{k}}$ denotes the valence (conduction) band edge energy. Further details can be found in the original work by Bardeen and Shockley [86].

2.5.1.3 Ionic materials

Polar materials have played a vital role in developing the theory of EPIs. In polar materials, the vibration pattern of the atoms induces an oscillating electric field that results in additional scattering to the charge carriers. Thus EPIs are usually strong in ionic materials.

In 1950, Frohlich *et al.* took into account the screening effects occurring due to dielectric polarization of the insulating medium and provided a model to estimate the effective potential (V_0) inside isotropic ionic systems, defined by

$$V_0 \longrightarrow \frac{-1}{|\mathbf{q}^2|} \sqrt{\left[\frac{e^2 \omega_{\mathbf{q}\nu}^2 M_\kappa}{\epsilon_0 \mathcal{V}} \left(\frac{1}{\epsilon^\infty} - \frac{1}{\epsilon^0} \right) \right]} \quad (2.36)$$

Here ϵ_0 is the permittivity of the free space. ϵ^0 and ϵ^∞ indicate the static and high-frequency relative permittivities, respectively. \mathcal{V} denotes the unit cell volume. For $\epsilon^0 > \epsilon^\infty$, EP matrix elements can be computed using 2.34 and 2.36. Notice that EP matrix elements ($g_{mn,\nu}(\mathbf{k}, \mathbf{q})$) diverge as $\frac{1}{|\mathbf{q}|}$ at long-wavelengths and give strong EPIs in the polar materials.

2.5.1.4 First calculations of EPIs from first principles

Estimating EPIs became possible after the significant development of *ab initio* DFT methods by 1981. The first predictive EPIs calculations were performed by Dacorogna *et al.* using “frozen-phonon” methods in 1985 [87]. They performed first principle calculations to compute Aluminum’s electronic and phonon band dispersions. Moreover, they performed self consistent field calculations to compute electron-phonon matrix elements ($g_{m\nu}(\mathbf{k}, \mathbf{q})$) and the electron-phonon coupling strength ($\lambda_{\mathbf{q}\nu}$) throughout the Brillouin zone for a few phonon bands. The average EP coupling strength was found to have a good agreement with the experiments.

2.5.2 Electron-phonon interactions in DFT

This section will discuss calculations of EPIs from DFT. First, we set up the formalism to obtain phonon frequencies and EP coupling Hamiltonian. Then we discuss the method to compute EP matrix elements based on density functional perturbation theory.

2.5.2.1 Standard formalism of lattice vibrations

Let us consider M nuclei inside a unit cell. The κ^{th} nucleus’s cartesian coordinates and position vector are denoted by $u_{\kappa\alpha}$ and \mathbf{u}_κ . Here we apply Born-von Kármán (BvK) boundary conditions to represent an infinite solid. The vectors \mathbf{R}_p (with $p = 1, \dots, N_p$) identify N_p unit cells in a periodic supercell. Thus position of κ^{th} nucleus inside p^{th} unit cell is the sum of \mathbf{R}_p and the position vector of the nucleus within the unit cell.

$$\mathbf{u}_{\kappa p} = \mathbf{R}_p + \mathbf{u}_\kappa \quad (2.37)$$

Within the BO approximation, the total potential energy of the crystal can be obtained from a standard DFT code implemented to handle periodic systems. Here $U(\{\mathbf{u}_\kappa\})$ labels the total energy of the system and $\{\mathbf{u}_\kappa\}$ denotes the set of all nuclei.

If BO approximation is relaxed and assumed that the nuclei vibrate about their mean positions ($\{\mathbf{u}_{\kappa p}^0\}$) with tiny amplitudes, then, within the harmonic approximation, the total energy of the system can be expressed as follows:

$$U = U_0 + \frac{1}{2} \sum_{\substack{\kappa\alpha p \\ \kappa'\alpha'p'}} \Phi_{\kappa\alpha p, \kappa'\alpha'p'} \Delta u_{\kappa\alpha p} \Delta u_{\kappa'\alpha'p'} \quad (2.38)$$

where U_0 indicates the total energy of the system at equilibrium, and $\Phi_{\kappa\alpha p, \kappa'\alpha' p'}$ indicates interatomic force constants (IFCs) and is given by

$$\Phi_{\kappa\alpha p, \kappa'\alpha' p'} = \frac{\partial^2 U}{\partial u_{\kappa\alpha p} \partial u_{\kappa'\alpha' p'}} \quad (2.39)$$

The dynamical matrix (DM) can be obtained by performing the Fourier transform of IFCs as follows [88]:

$$\mathcal{D}_{\kappa\alpha, \kappa'\alpha'}^{\text{DM}}(\mathbf{q}) = \frac{1}{\sqrt{(M_\kappa M_{\kappa'})}} \sum_p \Phi_{\kappa\alpha 0, \kappa'\alpha' p} \exp(i\mathbf{q} \cdot \mathbf{R}_p) \quad (2.40)$$

where M_κ is the mass of the κ^{th} nucleus and \mathbf{q} denotes a set of phonon wavevectors forming a uniform grid of N_p points to sample the one unit of reciprocal space.

The dynamical matrix is hermitian and yields real eigenvalues ($\omega_{\mathbf{q}\nu}^2$).

$$\sum_{\kappa'\alpha'} \mathcal{D}_{\kappa\alpha, \kappa'\alpha'}^{\text{DM}}(\mathbf{q}) e_{\kappa'\alpha', \nu}(\mathbf{q}) = \omega_{\mathbf{q}\nu}^2 e_{\kappa\alpha, \nu}(\mathbf{q}) \quad (2.41)$$

where ν varies from 1 to $3M$. $\omega_{\mathbf{q}\nu}$ denotes the frequency of the phonon mode ν with wavevector \mathbf{q} and $e_{\kappa\alpha, \nu}(\mathbf{q})$ indicates the normal mode of vibration corresponding to mode ν . We can use the frozen-phonon method or density functional perturbation theory (DFPT) to calculate the dynamical matrix [89].

Using Eqn. 2.38, one can write the Hamiltonian for nuclei being treated as quantum particles as follows:

$$\hat{H}_p = - \sum_{\kappa\alpha p} \frac{\hbar^2}{2M_\kappa} \frac{\partial^2}{\partial u_{\kappa\alpha p}^2} + \frac{1}{2} \sum_{\substack{\kappa\alpha p \\ \kappa'\alpha' p'}} \Phi_{\kappa\alpha p, \kappa'\alpha' p'} \Delta u_{\kappa\alpha p} \Delta u_{\kappa'\alpha' p'} \quad (2.42)$$

Here we have dropped the constant term the U_0 . The above equation holds good under the following approximations:

- Harmonic approximation which neglects the higher-order terms in the Taylor expansion of U . These higher-order terms are called anharmonic terms and are significant at higher temperatures [90].
- BO approximation while computing IFCs.

The above Hamiltonian can be expressed in the framework of second quantization as follows [85]:

$$\hat{H}_p = \sum_{\mathbf{q}\nu} \hbar\omega_{\mathbf{q}\nu} (\hat{a}_{\mathbf{q}\nu}^\dagger \hat{a}_{\mathbf{q}\nu} + \frac{1}{2}) \quad (2.43)$$

2.5.3 EP coupling Hamiltonian

This section will address how the rest of the terms are calculated entering in Eqn. 2.29.

2.5.3.1 KS Hamiltonian

Within the formalism of second quantization, we can express the KS Hamiltonian as follows:

$$\hat{H}_e = \sum_{n\mathbf{k}, n'\mathbf{k}'} \langle \psi_{n\mathbf{k}} | \hat{H}_{KS} | \psi_{n'\mathbf{k}'} \rangle \hat{c}_{n\mathbf{k}}^\dagger \hat{c}_{n'\mathbf{k}'} = \sum_{n\mathbf{k}} \epsilon_{n\mathbf{k}} \hat{c}_{n\mathbf{k}}^\dagger \hat{c}_{n\mathbf{k}} \quad (2.44)$$

2.5.3.2 EP coupling Hamiltonian to first and second order in DFT

In the following sections, we briefly discuss the formalism to obtain electron-phonon matrix elements from the first principles. More excellent details on the same are available elsewhere [85]. The first ($g_{mn\nu}(\mathbf{k}, \mathbf{q})$) and second-order ($g_{mn\nu\nu'}^{\text{DW}}(\mathbf{k}, \mathbf{q}, \mathbf{q}')$) EP matrix elements can be obtained by expanding V_{KS} in terms of the first and second derivatives with respect to atomic displacements about their mean positions.

$$V_{KS}(\{\mathbf{u}_{\kappa p}\}) = V_{KS}(\{\mathbf{u}_{\kappa\alpha p}^0\}) + \sum_{\kappa\alpha p} \frac{\partial V_{KS}}{\partial u_{\kappa\alpha p}} \Delta u_{\kappa\alpha p} \quad (2.45)$$

The above expression can be rewritten as follows:

$$V_{KS}(\{\mathbf{u}_{\kappa p}\}) = V_{KS}(\{\mathbf{u}_{\kappa\alpha p}^0\}) + \frac{1}{\sqrt{N_p}} \sum_{\mathbf{q}\nu} \Delta_{\mathbf{q}\nu} V_{KS}(\hat{a}_{\mathbf{q}\nu} + \hat{a}_{-\mathbf{q}\nu}^\dagger) \quad (2.46)$$

using

$$\Delta u_{\kappa\alpha p} = \left(\frac{M_0}{N_p M_\kappa} \right)^{1/2} \sum_{\mathbf{q}\nu} e^{i\mathbf{q}\cdot\mathbf{R}_p} e_{\kappa\alpha, \nu}(\mathbf{q}) l_{\mathbf{q}\nu} (\hat{a}_{\mathbf{q}\nu} + \hat{a}_{-\mathbf{q}\nu}^\dagger) \quad ; \quad l_{\mathbf{q}\nu} = \sqrt{\frac{\hbar}{2M_0\omega_{\mathbf{q}\nu}}} \quad (2.47)$$

where M_0 is taken to be the mass of the proton and $l_{q\nu}$ is called “zero-point” amplitude.

$$\Delta_{\mathbf{q}\nu} V_{KS} = e^{i\mathbf{q}\cdot\mathbf{r}} \Delta_{\mathbf{q}\nu} v_{KS} \quad ; \quad \Delta_{\mathbf{q}\nu} v_{KS} = l_{q\nu} \sum_{\kappa\alpha} \sqrt{\frac{M_0}{M_\kappa}} e_{\kappa\alpha,\nu}(\mathbf{q}) \partial_{\kappa\alpha,\mathbf{q}} v_{KS} \quad (2.48)$$

$$\partial_{\kappa\alpha,\mathbf{q}} v_{KS} = \sum_p e^{iq\cdot(\mathbf{r}-\mathbf{R}_p)} \left. \frac{\partial V_{KS}}{\partial u_{\kappa\alpha}} \right|_{\mathbf{r}-\mathbf{R}_p} \quad (2.49)$$

where $\Delta_{\mathbf{q}\nu} v_{KS}$ and $\partial_{\kappa\alpha,\mathbf{q}} v_{KS}$ are named as lattice-period functions.

The above expression can be related to first order EPIs within the formalism of second quantization as follows:

$$\hat{H}_{ep} = \sum_{n\mathbf{k},n'\mathbf{k}'} \langle \psi_{n\mathbf{k}} | V_{KS}(\{\mathbf{u}_{\kappa p}\}) - V_{KS}(\{\mathbf{u}_{\kappa\alpha p}^0\}) | \psi_{n'\mathbf{k}'} \rangle \hat{c}_{n\mathbf{k}}^\dagger \hat{c}_{n'\mathbf{k}'} \quad (2.50)$$

Using Eqn. 2.48, 2.49 and $\psi_{n\mathbf{k}}(\mathbf{r}) = N_p^{-1/2} u_{n\mathbf{k}}(\mathbf{r}) e^{i\mathbf{k}\cdot\mathbf{r}}$, one can write as follows:

$$\hat{H}_{ep} = N_p^{-1/2} \sum_{\substack{\mathbf{k}, \mathbf{q} \\ mn\nu}} g_{mn\nu}(\mathbf{k}, \mathbf{q}) \hat{c}_{m\mathbf{k}+\mathbf{q}}^\dagger \hat{c}_{n\mathbf{k}} (\hat{a}_{\mathbf{q}\nu} + \hat{a}_{-\mathbf{q}\nu}^\dagger) \quad (2.51)$$

where the EP matrix element within the unit cell is given by

$$g_{mn\nu}(\mathbf{k}, \mathbf{q}) = \langle u_{m\mathbf{k}+\mathbf{q}} | \Delta_{\mathbf{q}\nu} v_{KS} | u_{n\mathbf{k}} \rangle \quad (2.52)$$

If we expand the V_{KS} up to second derivate w.r.t to atomic displacements and follow a similar method, then we obtain the second order EP coupling Hamiltonian as follows:

$$\hat{H}_{ep}^{(2)} = N_p^{-1} \sum_{\substack{\mathbf{k}, \mathbf{q}, \mathbf{q}' \\ mn\nu\nu'}} g_{mn\nu\nu'}^{\text{DW}}(\mathbf{k}, \mathbf{q}, \mathbf{q}') \hat{c}_{m\mathbf{k}+\mathbf{q}+\mathbf{q}'}^\dagger \hat{c}_{n\mathbf{k}} (\hat{a}_{\mathbf{q}\nu} + \hat{a}_{-\mathbf{q}\nu}^\dagger) (\hat{a}_{\mathbf{q}'\nu'} + \hat{a}_{-\mathbf{q}'\nu'}^\dagger) \quad (2.53)$$

where $g_{mn\nu\nu'}^{\text{DW}}(\mathbf{k}, \mathbf{q}, \mathbf{q}') = \frac{1}{2} \langle u_{m\mathbf{k}+\mathbf{q}+\mathbf{q}'} | \Delta_{\mathbf{q}\nu} \Delta_{\mathbf{q}'\nu'} v_{KS} | u_{n\mathbf{k}} \rangle$ is computed within the unit cell.

2.5.3.3 Calculation of EP matrix elements

The EP matrix elements ($g_{mn\nu}(\mathbf{k}, \mathbf{q})$) are obtained using the frozen-phonon method, DFPT and the dielectric approach. This section will succinctly discuss the first two approaches

to obtaining EP matrix elements. The dielectric approach is discussed elsewhere [85].

Within the frozen-phonon method, one can evaluate the derivative of potential using the finite difference method as follows:

$$\left. \frac{\partial V_{KS}}{\partial u_{\kappa\alpha p}} \right|_{u_{\kappa p}^0} \simeq \frac{V_{KS}(\mathbf{r}; u_{\kappa\alpha p}^0 + d) - V_{KS}(\mathbf{r}; u_{\kappa\alpha p}^0 - d)}{2d} \quad (2.54)$$

In the above expression, d is a tiny displacement of the κ^{th} nucleus of the p^{th} unit cell along the α -direction, which is of the order of zero-point amplitude ($l_{q\nu}$) defined by Eqn. 2.47. This method is widely used in the scientific community. However, this method requires a big supercell to calculate the EP matrix elements corresponding to large-wavelength phonons.

Baroni *et al.* have proposed a new approach to compute the scattering potential using DFPT [89]. The advantage of their method is that it is computationally cheaper than the frozen-phonon method since one does not require a supercell to compute scattering potential ($\Delta_{\mathbf{q}\nu} v_{KS}$).

Within the DFPT approach, the lattice-period scattering potential ($\partial_{\kappa\alpha, \mathbf{q}} v_{KS}$) is computed by differentiating V_{KS} using 2.49 and is given by

$$\partial_{\kappa\alpha, \mathbf{q}} v_{KS} = \partial_{\kappa\alpha, \mathbf{q}} v_{ext} + \partial_{\kappa\alpha, \mathbf{q}} v_H + \partial_{\kappa\alpha, \mathbf{q}} v_{XC} \quad (2.55)$$

The variation of the above potentials are computed using V_{ext} , V_H and V_{XC} and results are expressed in Fourier transform as follows:

$$\partial_{\kappa\alpha, \mathbf{q}} v_{ext}(\mathbf{G}) = -i(\mathbf{q}+\mathbf{G})_{\alpha} V_{\kappa}(\mathbf{q}+\mathbf{G}) e^{-i(\mathbf{q}+\mathbf{G}) \cdot \mathbf{u}_{\kappa}} \quad (2.56)$$

$$\partial_{\kappa\alpha, \mathbf{q}} v_H(\mathbf{G}) = \Omega v_C(\mathbf{q}+\mathbf{G}) \partial_{\kappa\alpha, \mathbf{q}} n(\mathbf{G}) \quad ; \text{ where } v_C(\mathbf{q}) = \frac{1}{\Omega} \frac{e^2}{4\pi\epsilon_0} \int d\mathbf{r} \frac{e^{-i\mathbf{q} \cdot \mathbf{r}}}{|\mathbf{r}|} \quad (2.57)$$

$$\partial_{\kappa\alpha, \mathbf{q}} v_{XC}(\mathbf{G}) = \Omega \sum_{\mathbf{G}'} f_{XC}(\mathbf{q}+\mathbf{G}, \mathbf{q}+\mathbf{G}') \partial_{\kappa\alpha, \mathbf{q}} n(\mathbf{G}') \quad (2.58)$$

where $f_{XC}(\mathbf{r}, \mathbf{r}')$ is the second-order functional derivative of E_{XC} with $n(\mathbf{r})$, given by

$$f_{XC}(\mathbf{r}, \mathbf{r}') = \frac{\delta^2 E_{XC}[n]}{\delta n(\mathbf{r})\delta n(\mathbf{r}')} \Big|_{n(\mathbf{r}; \{u_{\kappa\alpha p}^0\})} \quad (2.59)$$

The above equations 2.57 and 2.58 involve the variation of the charge density rendered by perturbation potential. The charge density variation is computed by finding the first-order correction to KS wavefunctions using perturbation theory. More details on this can be found elsewhere [85, 89].

2.6 Electron self-energy

Inside a crystal, the electron's energy is influenced by the many-body interactions occurring due to the other electrons and phonons. Thus electron self-energy arising due to EPIs can be described with infinite Feynman diagrams. Notably, Migdal has shown that only the lowest order Feynman diagram is sufficient to consider while calculating electron self-energy [91]. Within the Migdal approximation, Feynman diagram of electron self-energy arising due to EPIs is shown in Fig. 2.3. Following the Green's function approach to many-body interactions so-called "Field-theoretic approach," one can arrive at the following expression for electron-self energy within the Migdal approximation:

$$\sum_{n\mathbf{k}}^{EP} = \sum_{\mathbf{q}\nu, m} w_{\mathbf{q}} |g_{mn, \nu}(\mathbf{k}, \mathbf{q})|^2 \left[\frac{n_{\mathbf{q}\nu} + 1 - f_{m\mathbf{k}+\mathbf{q}}}{\epsilon_{n\mathbf{k}} - \epsilon_{m\mathbf{k}+\mathbf{q}} - \hbar\omega_{\mathbf{q}\nu} - i\delta} + \frac{n_{\mathbf{q}\nu} + f_{m\mathbf{k}+\mathbf{q}}}{\epsilon_{n\mathbf{k}} - \epsilon_{m\mathbf{k}+\mathbf{q}} + \hbar\omega_{\mathbf{q}\nu} - i\delta} \right] \quad (2.60)$$

where $g_{mn, \nu}(\mathbf{k}, \mathbf{q}) = (\frac{\hbar}{2m_0\omega_{\mathbf{q}\nu}})^{1/2} \langle \psi_{m\mathbf{k}+\mathbf{q}} | \partial_{\mathbf{q}\nu} V_{KS} | \psi_{n\mathbf{k}} \rangle$. $w_{\mathbf{q}}$ is the weight associated with phonon wavevector \mathbf{q} in the Brillouin zone, $\partial_{\mathbf{q}\nu} V_{KS}$ is the derivative of self consistent potential associated with a phonon of wavevector \mathbf{q} , branch index ν and frequency $\omega_{\mathbf{q}\nu}$. The temperature dependence of electron self-energy originates from the Fermi-Dirac ($f_{m\mathbf{k}+\mathbf{q}}$) and Bose-Einstein occupations ($n_{\mathbf{q}\nu}$), while EP matrix elements are calculated at 0K using DFPT. In 2.60, the first and second term in square bracket refer to phonon emission and absorption, respectively.

Notice that electron self-energy is computed for each band and k point, thus providing

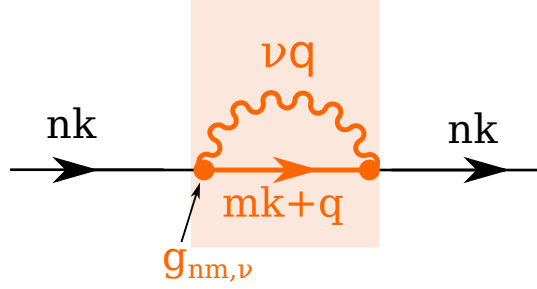


Figure 2.3: Feynman diagram for electron self-energy arising due to EPIs within Migdal approximation. This diagram is made up of two diagrams representing the phonon emission (left half) and absorption (right half).

vast information on the microscopic level. Therefore, electron self-energy convergence usually requires an ultra-dense q -grid containing $10^4 - 10^6$ q -points to sum over q in equation 2.60. However, the direct calculation of EP matrix elements is impossible on such a dense grid using DFPT due to intractable computational cost. Thus one relies on an interpolation scheme using maximally localized Wannier functions to achieve so. Further computational details can be found elsewhere [85, 92].

Temperature-dependent band structure can be obtained by adding the real part of electron self-energy to the KS eigenvalues as follows:

$$E_{n,\mathbf{k}} = \epsilon_{n,\mathbf{k}} + \text{Re} \sum_{n\mathbf{k}}^{EP} \quad (2.61)$$

The relaxation time of the charge carriers in each electronic state $n\mathbf{k}$ can be obtained from the imaginary part of self-energy as follows:

$$\tau_{n,\mathbf{k}} = \frac{\hbar}{2 \left(\text{Im} \sum_{n\mathbf{k}}^{EP} \right)} \quad (2.62)$$

The electronic transport properties of a material, like electrical conductivity, electronic thermal conductivity and mobility, etc., depend on the relaxation time $\tau_{n,\mathbf{k}}$, which depends on the strength of EPIs in the system. If one can not capture the scattering contribution due to various phonon modes, the wrong estimate of $\tau_{n,\mathbf{k}}$ is possible, and it might overestimate the transport properties. Thus the determination of $\tau_{n,\mathbf{k}}$ to a reasonable accuracy is crucial

for *in silico* search of new thermoelectric materials. The same is true at elevated temperatures. Further, as discussed in the following section, one can incorporate the computed relaxation time into the transport coefficients to get their absolute values.

2.7 Semiclassical Boltzmann Transport

In general, transport properties of a material can be understood in terms of the response of carriers to external perturbations like external electric fields or temperature gradient, etc. Boltzmann transport theory can be applied to understand transport properties and calculate the transport coefficients. The electric current j_i in the presence of electric fields and temperature gradient can be expressed in terms of conductivity tensors as follows [93]:

$$j_i = \sigma_{ij} E_j + \nu_{ij} \nabla_j T + \dots \quad (2.63)$$

The conductivity tensor in terms of group velocity (v) and relaxation time (τ) is written as

$$\sigma_{\alpha\beta}(i, \mathbf{k}) = e^2 \tau_{i,\mathbf{k}} v_\alpha(i, \mathbf{k}) v_\beta(i, \mathbf{k}) \quad (2.64)$$

where group velocity along α -direction can be computed from electronic band structure.

$$v_\alpha(i, \mathbf{k}) = \frac{1}{\hbar} \frac{\partial \epsilon_{i,\mathbf{k}}}{\partial k_\alpha} \quad (2.65)$$

$\tau_{n,\mathbf{k}}$ depends on several factors like scattering by defects, disorders and electron-phonon interactions, etc. Dependence of $\tau_{n,\mathbf{k}}$ on scattering from phonons can be theoretically estimated from electron-phonon coupling as described in the previous sections. One can also assume that $\tau_{i,\mathbf{k}}$ is independent of the electronic states and temperature and thus it can be treated as a constant. This approximation is called constant relaxation time approximation (CRTA). Further, we can write the conductivity tensor in terms of energy by projecting the density of states with conductivity tensor as follows.

$$\sigma_{\alpha\beta}(\epsilon) = \frac{1}{N} \sum_{i,\mathbf{k}} \sigma_{\alpha\beta}(i, \mathbf{k}) \frac{\delta(\epsilon - \epsilon_{i,\mathbf{k}})}{d\epsilon} \quad (2.66)$$

This is called transport distribution function. Transport coefficients can be obtained as a function of chemical potential (μ) and temperature (T) as below.

$$\sigma_{\alpha\beta}(T; \mu) = \frac{1}{V} \int \sigma_{\alpha\beta}(\epsilon) \left[\frac{-\partial f_0(T, \epsilon, \mu)}{\partial \epsilon} \right] d\epsilon \quad (2.67)$$

$$S_{\alpha\beta}(T; \mu) = \frac{1}{eT\sigma_{\alpha\beta}(T; \mu)} \int \sigma_{\alpha\beta}(\epsilon)(\epsilon - \mu) \left[\frac{-\partial f_0(T, \epsilon, \mu)}{\partial \epsilon} \right] d\epsilon \quad (2.68)$$

$$\kappa_{\alpha\beta}(T; \mu) = \frac{1}{e^2TV} \int \sigma_{\alpha\beta}(\epsilon)(\epsilon - \mu)^2 \left[\frac{-\partial f_0(T, \epsilon, \mu)}{\partial \epsilon} \right] d\epsilon \quad (2.69)$$

$$\nu_{\alpha\beta}(T; \mu) = \frac{1}{eTV} \int \sigma_{\alpha\beta}(\epsilon)(\epsilon - \mu) \left[\frac{-\partial f_0(T, \epsilon, \mu)}{\partial \epsilon} \right] d\epsilon \quad (2.70)$$

where f_0 is the Fermi Dirac occupation, V indicates the volume of the unit cell. The absolute values of transport coefficients can be obtained by incorporating $\tau_{i,\mathbf{k}}$ calculated explicitly by various methods like deformation potential theory, by computing imaginary part of self-energies of carriers and through experiments, etc.

Chapter 3

Identifying resonant dopants for BaCu_2Se_2

3.1 Introduction

We have discussed in **Chapter 1** that ZT can be enhanced by increasing the power factor ($\text{PF}=\alpha^2\sigma$) and reducing the thermal conductivity. In this chapter, we adopt a band structure engineering technique to increase the PF. Amongst the different ways to achieve band engineering, we chose resonant doping approach to do so. Conventionally, in semiconductor physics, donor (acceptor) impurity provides free charge carriers through the discrete donor (acceptor) levels formed in the band gap near the conduction (valence) bands. An activation energy (E_D) is required to excite these extra charge carriers to participate in the transport phenomenon. In contrast, a resonant state is formed when a defect level lies inside the conduction (valence) bands and overlaps with energies of conduction (valence) electronic states. As a result, it acquires a width Γ and produces a distortion in density of states (Fig. 1.2). Furthermore, its effects on electronic and transport properties are discussed in detail in chapter 1.

A couple of experimental reports have demonstrated the potential of resonant doping in practice. For instance, Heremans *et al.* have successfully achieved a ZT value of 1.5 due to enhancement of thermopower with 2% of Tl doping in PbTe at 773 K. [72]. Moreover, Zhang *et al.* have obtained a ZT value of 1.3 through Al doping in PbSe [94]. Interestingly, an experimental and theoretical study by Pan *et al.* has investigated the impact of resonant doping by Na and Tl co-doping in PbSe [95]. Their study reveals that resonant dopants do not always enhance ZT since enhancement in S , sometimes, comes with significant reduction of mobility [95]. Theoretically, Jiahong *et al.* have investigated that In (Tl) doping in BiCuSeO could give rise to resonant states near the conduction (valence)

bands [96].

In this project, we identify resonant dopants for copper chalcogenide (BaCu_2Se_2). Similar to clathrates, this class of materials is given a huge amount of attention in thermoelectrics because they contain rattling atoms residing in large cages formed by other types of atoms. [97] Thus these materials usually possess ultralow lattice thermal conductivities since the rattling atom disrupts the other vibrations as they travel through the medium. Moreover, this class of materials is also cost-effective [98].

BaCu_2Se_2 exists in two phases, a stable orthorhombic phase and a metastable tetragonal phase. Theoretically, it has been predicted that phase transition may occur from orthorhombic to tetragonal phase at 950 K, but no such transition was seen experimentally until 873 K. [99] We have investigated both the phases, but we discuss results only for orthorhombic phase because results are not promising for the tetragonal system. Orthorhombic BaCu_2Se_2 exhibits high Seebeck coefficient ($390 \mu\text{V/K}$), moderate electrical conductivity (5.5 S cm^{-1}) and low lattice thermal conductivity ($\sim 1.5 \text{ W/mK}$) at 300 K. [58] Zheng *et al.* have shown that potassium doping on Ba-site could give ZT value of 0.3 at 800 K by increasing the electrical conductivity by one order of magnitude [100]. Moreover, it has been reported that Na doping on Ba-site improves the electrical conductivity by 2 orders of magnitude which give rise to a $ZT \sim 1$ at 773 K, which reflects that orthorhombic BaCu_2Se_2 is a prominent thermoelectric materials. [58]

In this project, we study the effect of doping group 13 elements, namely Al, Ga, In and Tl, in BaCu_2Se_2 . Here group 13 elements are chosen because it has been observed that s and p -orbitals of dopants are more likely to hybridize with band structure of parent system and produce localized states [71]. In particular, we are interested in identifying dopants that give rise to resonant states. Some of these dopants have been reported to improve ZT of some materials like GeTe and PbTe through resonant doping [72, 101]. Here we investigate effects of these dopants on the electronic and transport properties of orthorhombic BaCu_2Se_2 .

3.2 Computational details

We have performed first principles calculations based on density functional (DFT) theory as implemented in the Quantum ESPRESSO software [102, 103]. Ultrasoft pseu-

dopotentials have been used to describe the interactions between the valence electrons and ionic cores [82]. For the different elements following valence electronic configuration have been used: Ba- $5s^25p^66s^2$, Cu- $3d^{10}4s^1$, Se- $4s^24p^4$, Al- $3s^23p^1$, Ga- $3d^{10}4s^24p^1$, In- $4d^{10}5s^25p^1$ and Tl- $5d^{10}6s^26p^1$. The exchange-correlation potential of electrons was described by using the Perdew-Burke-Ernezerhof (PBE) form of generalized gradient approximation (GGA) [79]. We have used energy cutoffs of 50 and 450 Ry for wavefunction and charge density, respectively. For conventional unit cell, Brillouin zone (BZ) integrations are performed using a $(12 \times 4 \times 4)$ Monkhorst-Pack [80] k -point grid.

We have constructed $(2 \times 1 \times 1)$ supercell containing 40 atoms. We have sampled its Brillouin zone using a $(6 \times 4 \times 4)$ Monkhorst-Pack [80] k -point grid for the BZ integrations. The boron group of elements was tried as dopants, namely, Aluminium (Al), Gallium (Ga), Indium (In) and Thallium (Tl). We have substituted one of the host atoms in supercell by a dopant atom resulting in doping concentrations of 12.5%, 6.25% and 6.25% when Ba, Cu and Se are substituted, respectively.

As DFT fails to describe accurate electronic picture of atoms with strongly correlated electrons. Therefore, Hubbard U corrections (with $U = 4$ eV) is considered in our study to account for the on-site Coulomb interaction in d orbitals of Cu-atoms [104]. The reason for choosing $U = 4$ eV is discussed in Appendix A. We have also carried out spin-polarized calculations to determine the ground state of doped systems and it is observed that all dopants prefer a non-magnetic ground state.

Based on PBE+ U band structure, transport properties are computed as function of electron doping by solving the semiclassical Boltzmann transport equations using BoltzTraP code [93]. A k -point grid of $(36 \times 24 \times 24)$ is used for accurate Fourier interpolation of energy eigenvalues and to ensure the convergence of transport properties with respect to k -points.

3.3 Results and discussion

3.3.1 Structure and electronic properties of BaCu_2Se_2

BaCu_2Se_2 is known to exist in orthorhombic (α) crystal structures with space group $Pnma$. In this system, Ba is sevenfold coordinated with Se atoms in a trigonal prismatic

geometry where the seventh Se atom caps one of rectangular faces. Each Ba is also surrounded by nine Cu atoms arranged in a tricapped trigonal prismatic configuration (Fig. 3.1). We find that Ba-Se distances vary from 3.20 to 3.43 Å and Ba-Cu distances range from 3.42 to 3.72 Å. There are two kinds of Cu atoms (Cu_1 and Cu_2) forming tetrahedra (T_1 and T_2 , respectively) with the anions. T_2 (blue) is more distorted relative to T_1 (red) due to fact that Cu atom is closer to tetrahedral face. This also gives rise to two types of Se atoms (Se_1 and Se_2) corresponding to T_1 and T_2 tetrahedra. In T_1 , Cu_1 -Se bond distances are 2.59 (twice) and 2.54 (twice) Å, while the Cu_2 -Se bond distances are 2.50 (twice), 2.52 and 2.62 Å in T_2 .

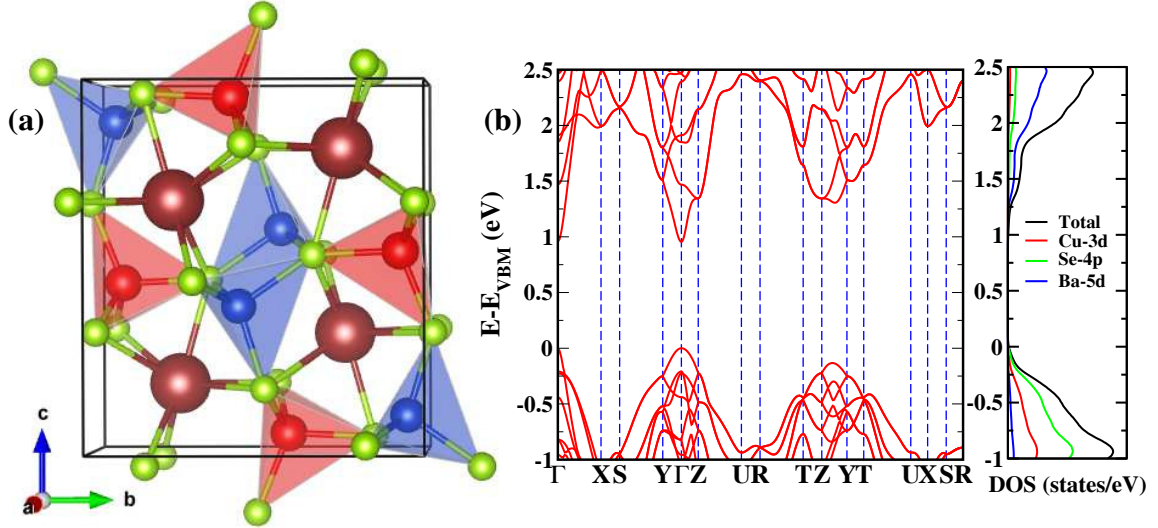


Figure 3.1: (a) Crystal structure of orthorhombic BaCu_2Se_2 . Brown, red, blue and green colored spheres are used to represent Ba, Cu_1 , Cu_2 and Se atoms, respectively. (b) Electronic band structure (left) and the projected density of states (right) of BaCu_2Se_2 computed at the PBE+U level. The valence band maximum (VBM) is set to zero.

We have obtained the lattice constants after geometry optimization of the conventional unit cell (Table 3.1). We have provided the previous computational and experimental reports on these systems for comparison. Our results are in agreement with previous computational and experimental studies. [105, 106].

The electronic band structure for pristine BaCu_2Se_2 is shown in Fig. 3.1 (b) (left). It has a direct band gap at Γ point of the BZ. We have obtained a band gap of ~ 0.98 eV with PBE+U functionals. Further, Gau-PBE hybrid functionals have been used to predict the band gap accurately [109]. The estimated band gap with PBE+U and Gau-

Table 3.1: The optimized lattice constants for BaCu₂Se₂ are listed. For comparison, we have mentioned the lattice constants from the previous theoretical and experimental reports.

BaCu ₂ Se ₂	PBE+U	Exp [105]	Exp [106]	(others, PBE) [107]	(others, PBE) [99]	(others, revPBE [108])
a (Å)	4.23	4.21	4.21	4.20	4.24	4.32
b (Å)	9.80	9.59	9.59	9.57	9.66	9.74
c (Å)	10.82	10.77	10.78	10.75	10.88	10.94

PBE functionals are listed in Table 3.2. For the sake of comparison, we have mentioned the band gap reported by previous computational and experimental studies. We noticed that band gap computed with Gau-PBE is in close agreement with experiments, while the same estimated with HSE computed by Zuo *et al.* is underestimated by 0.42 eV compared to experimental value [106, 108]. Fig. 3.1 (b) (right) shows the density of states (DOS) projected onto the atomic orbitals of Ba, Cu and Se atoms. We find that the valence bands are comprised of *3d*-orbitals of Cu and *4p*-orbitals of Se atoms, while *5d*-orbitals of Ba atoms have dominant contribution in the conduction bands.

Table 3.2: The band gaps for BaCu₂Se₂ computed with PBE+U and Gau-PBE functionals. The values of band gap from previous theoretical and experimental reports are also given.

BaCu ₂ Se ₂	PBE+U	Gau-PBE	Exp. [106]	(others, PBE) [106]	(others, HSE) [108]	(others, revPBE+U) [108]
E_g (eV)	0.98	1.85	1.80	1.30	1.38	0.85

3.3.2 Effect of doping BaCu₂Se₂

Fig. 3.2 shows the formation energies (E^f) of doped configurations computed using Eq. (3.1).

$$E^f = E_{tot} - E_{pristine} - E_D + E_H \quad (3.1)$$

where D stands for dopant atoms (Al, Ga, In, Tl) and H stands for the available lattice sites i.e. (Ba, Cu and Se). E_{tot} and $E_{pristine}$ are the DFT total energies of doped and pristine system, respectively. E_D and E_H are the DFT energies of one dopant atom and one host atom in its respective bulk phase. We notice that all the elements prefer Cu-site as the formation energies are lowest in these cases (Fig. 3.2) with comparable values of the formation energies for doping on Cu₁ and Cu₂-site. The reason can be attributed to comparable sizes of atomic radii of the dopants to that of Cu atoms. Hence both the Cu-sites are considered for further investigations.

The optimized lattice parameters of the doped configurations with the lowest formation energies are mentioned in Table 3.3. The changes in bond distances are mentioned in Appendix A.

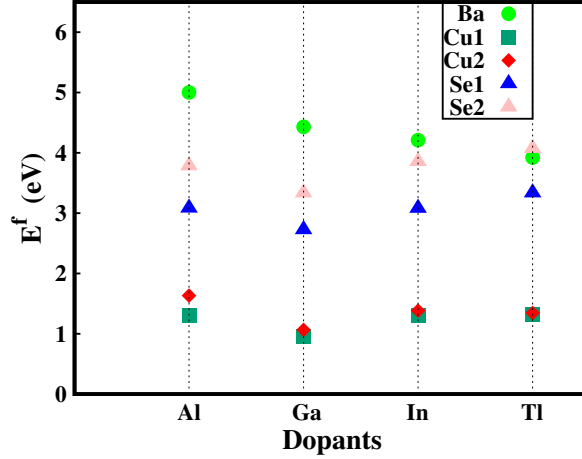


Figure 3.2: The formation energies are computed for boron group of elements doped on Cu, Se and Ba lattice sites.

Table 3.3: The optimized lattice constants for pristine and doped configurations with $(2 \times 1 \times 1)$ supercell.

BaCu ₂ Se ₂	Parent	Cu ₁ -site				
		Al	Ga	In	Tl	
a (Å)	8.46	8.45	8.47	8.51	8.53	
b (Å)	9.79	9.75	9.79	9.81	9.84	
c (Å)	10.82	11.05	11.00	11.10	11.10	
		Cu ₂ -site				
		Parent	Al	Ga	In	Tl
a (Å)	8.46	8.41	8.46	8.54	8.55	
b (Å)	9.79	9.82	9.87	9.90	9.92	
c (Å)	10.82	11.05	10.96	10.89	10.90	

Electronic properties:

In the doped configurations (including both Cu₁ and Cu₂-sites), we observe three distinct peaks arising due to electronic states of dopant atoms (Fig. 3.3 (a-d) and Fig. 3.4 (a-d)). Two of them are occupied states and contribute primarily from *s*-orbital of impurity atom. The first occupied state is deep defect state which lies in the deep valence bands around ~ -6 eV and the second one is found in the gap. The third peak is unoccupied and arises due

to p -orbitals of impurity atom. This impurity state hybridizes with the conduction band states (due to Se- s and Ba- d orbitals) of the parent compound giving rise to resonant levels (RLs). When one host Cu₁ (Cu₂) atom is removed from the bulk system it leaves one hole in system. Doping with boron group of elements on Cu₁ (Cu₂) site donates three extra electrons into the system. One of them is used to compensate the hole, while other two reside in Cu-Se network and give rise to occupied state at the band gap (slightly below Fermi energy). As a result, two extra electrons do not contribute to the transport.

In general, adding the dopants on the Cu₂-site has similar effects on its electronic structure (Fig. 3.4). However, the empty states observed in these doped configurations are delocalized compared to the case where the dopants occupy Cu₁-site. The reason behind this is the nearest neighboring environment of the Cu₁ and Cu₂ sites. When Al is doped on Cu₁-site, Al- p orbital strongly interacts with s orbitals of the nearest two Cu atoms. Moreover, it also strongly interacts with p orbitals of the nearest three Se atoms, whereas it interacts weakly with p -orbital of the fourth Se atom (Fig. A.2(c)). On the other hand, when Al occupies Cu₂-site, it interacts uniformly with p orbitals of four Se atoms and s -orbital of two Cu atoms (Fig. A.2(d)). Similar trends are observed in other doped configurations.

3.3.3 Transport properties of doped configurations

To investigate the effect of resonant states on transport properties we have computed transport coefficients as a function of electron concentration. We have only considered electrons as the carriers because from our electronic structure calculations we have found that the defect induced state is in resonance with the bottom of the conduction band.

Doping at Cu₁-site: When the carrier concentration is in between $(10^{20} - 10^{21}) \text{ cm}^{-3}$, Seebeck coefficient (S) of pristine system starts from $32 \mu\text{V/K}$ and attains a maximum value of $40 \mu\text{V/K}$ at $(3.8 \times 10^{20}) \text{ cm}^{-3}$ (Fig. 3.5 (a)). This carrier concentration corresponds to the chemical potential (μ) touching the second CBM which has a greater curvature compared to that of the first CBM (Fig. 3.1 (b)). For Al-doped BaCu₂Se₂, S has increased significantly compared to pristine and varies from $38 - 141 \mu\text{V/K}$. For Ga-doped BaCu₂Se₂, S attains a maximum values of $\sim 61 \mu\text{V/K}$ around 10^{21} cm^{-3} , while S of In-doped system shows good improvement ($23 - 68 \mu\text{V/K}$) compared to the pristine in doping range $(10^{20} - 10^{21}) \text{ cm}^{-3}$. In Tl-doped case, S is slightly greater than that of pristine system below (1.9×10^{20}) , but it is smaller than the pristine in range $(1.9 \times 10^{20} - 10^{21})$

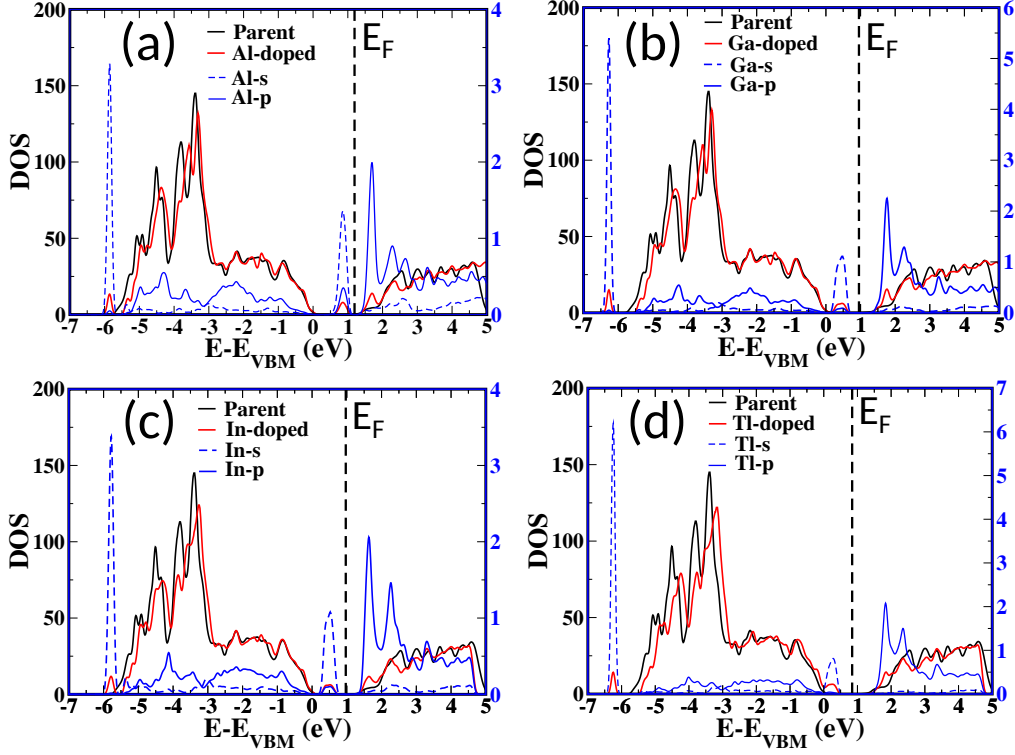


Figure 3.3: The total DOS of pristine (black) and doped (red) BaCu_2Se_2 computed at the level of PBE+U. The DOS projected on dopant s and p -states are shown in dashed and solid blue lines respectively. (a), (b), (c) and (d) are for Al, Ga, In and Tl doped cases. The dopant atom occupies Cu_1 -site. The VBM is set to zero in all the cases.

cm^{-3} . The origin of increase in S in doped configurations can be attributed to local increase in the density of states due to resonant states. In particular, we find that an increase in DOS occurs due to resonant states when μ reaches around 1.43, 1.62, 1.42 and 1.61 eV corresponding to 10^{20} , 10^{21} , 2×10^{20} and $6 \times 10^{20} \text{ cm}^{-3}$ in Al, Ga, In and Tl-doped systems respectively.

The electrical conductivity in terms of scattering time (σ/τ) has been shown in Fig. 3.5 (b) for the pristine and doped configurations. The conductivity values of all systems are comparable around 10^{20} cm^{-3} . However, as the carrier concentration increases for the doped system σ/τ shows a significant reduction with respect to the pristine one. The electronic part of thermal conductivity in terms of scattering time (κ_e/τ) has similar behavior as observed for σ/τ (Fig. 3.5 (d)) since they are connected by Wiedemann-Franz law.

The power factor in terms scattering time (PF/τ) as function of electron concentration is

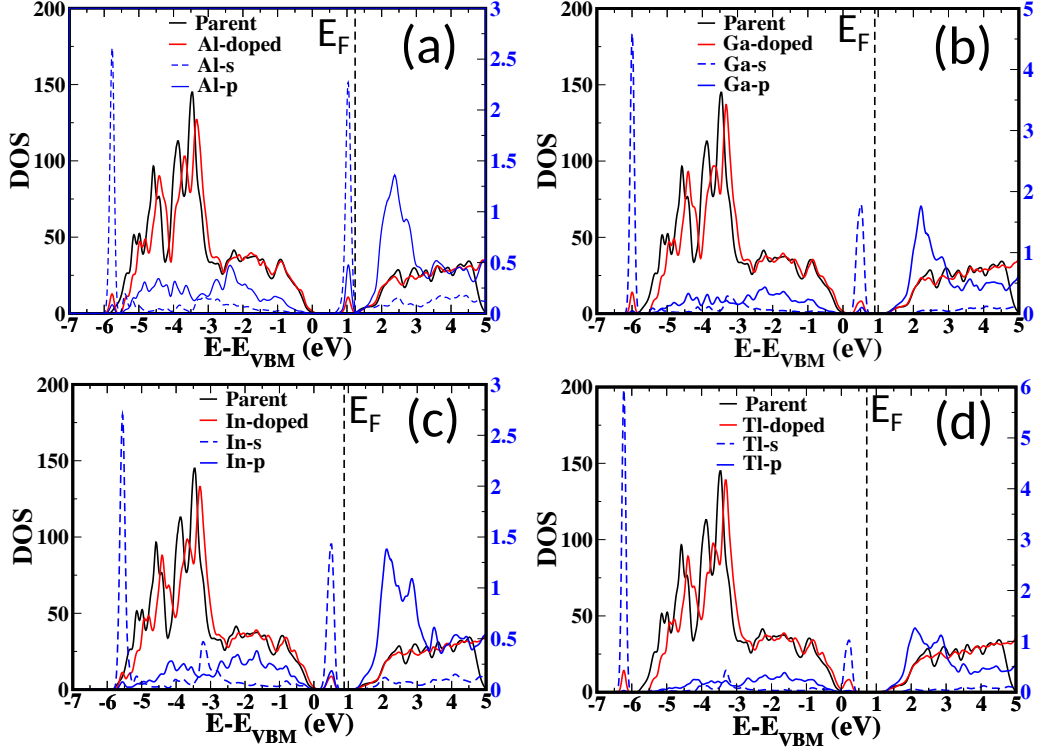


Figure 3.4: The total DOS of pristine (black) and doped (red) BaCu_2Se_2 calculated at the level of PBE+U. The DOS projected on dopant s and p -states are shown in dashed and solid blue lines respectively. (a), (b), (c) and (d) are for Al, Ga, In and Tl doped cases. The dopant atom occupies Cu_2 -site. The VBM is set to zero in all the cases.

shown in Fig. 3.5 (c) for the pristine and doped configurations. The optimized PF/τ of pristine system is found to be ($\sim 3.1 \text{ W/mK}^2\text{sec}$ at $5 \times 10^{20} \text{ cm}^{-3}$). The highest value of optimized PF/τ is observed ($\sim 7.8 \text{ W/mK}^2\text{sec}$ at 10^{20} cm^{-3}) in Al-doped BaCu_2Se_2 when μ touches the energy of resonant level ($\mu \sim 1.4 \text{ eV}$). In similar manner, optimization of PF/τ occurs ($\sim 6.25 \text{ W/mK}^2\text{sec}$ at $9.68 \times 10^{20} \text{ cm}^{-3}$) for Ga-doped system around 10^{21} when μ ($\sim 1.6 \text{ eV}$) starts to touch the resonant level. Since the power factor is the product of square of Seebeck coefficient and electrical conductivity. In our case, we see that doped configurations show increment in S while decrement in electrical conductivity compared to pristine system in between ($10^{20} - 10^{21}$) cm^{-3} . Therefore, any increment in PF can be attributed to an increment in S due to the presence of resonant states.

The electronic figure of merit (ZT_e), independent of τ , is shown for these systems as a function of carrier concentration (Fig. 3.5 (e)). While at low carrier concentration ZT_e is large in accordance with the fact that PF and S , are enhanced, at carrier concentration

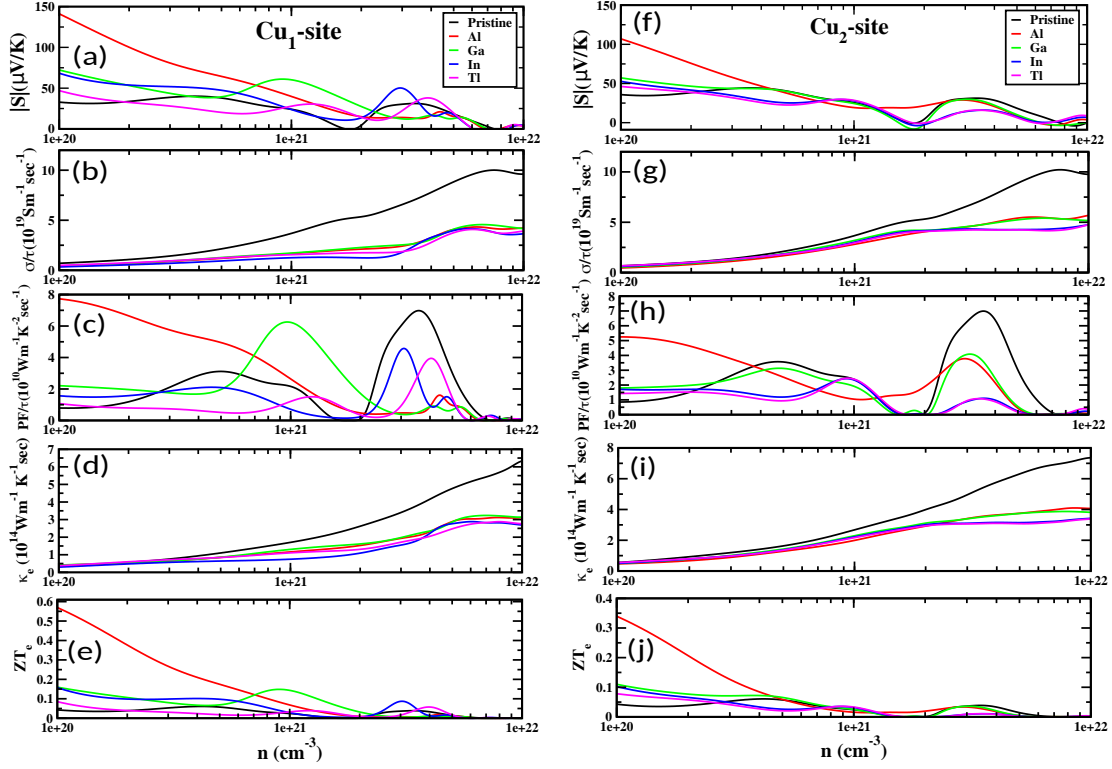


Figure 3.5: (a,d) $|S|$, (b,e) σ/τ and (c,f) PF/τ as a function of carrier concentration for pristine and doped configurations corresponding to Cu_1 -site (left) and Cu_2 -site (right).

of about 10^{21}cm^{-3} and higher, ZT_e decreases drastically for all the cases. This can be attributed to the fact that the κ_e is significantly large at the above mentioned carrier concentration.

Doping at Cu_2 -site: Similar to what was observed for doping at Cu_1 -site, here also we find that Al-doped BaCu_2Se_2 has the largest value of S compared to the pristine one at low carrier concentration, whereas S of other doped cases is comparable to that of the parent compound. In particular, for Al-doped BaCu_2Se_2 , S varies between 19-107 $\mu\text{V}/\text{K}$ when carrier concentration is in between $(10^{20} - 10^{21})\text{cm}^{-3}$, whereas S varies between 24-57, 27-52 and 46-28 $\mu\text{V}/\text{K}$ for Ga, In and Tl-doped systems, respectively. Since the resonant states are delocalized when dopants occupy Cu_2 -site, steepness in DOS is less compared to the cases when dopants occupy Cu_1 -site. Therefore, the overall increment in S is small in these doped configurations corresponding to Cu_2 -site compared to that of Cu_1 -site. Moreover, for the other dopants the steepness in DOS near the conduction band edges is similar, resulting in comparable S values for these systems.

The electrical conductivities of these doped configurations are similar to that of pristine around 10^{20}cm^{-3} , whereas doped configurations show reduction in σ/τ at high carrier concentrations (Fig. 3.5 (g)). The electronic thermal conductivity varies with respect to carrier concentration in a similar manner as observed for σ/τ (Fig. 3.5 (i)).

As a result, a significant enhancement in PF/τ ($\sim 5.2 \text{ W/mK}^2\text{sec}$ at 10^{20}) in Al-doped BaCu_2Se_2 is observed compared to pristine system (Fig. 3.5 (h)), while PF/τ for Ga-doped system is comparable to the pristine system in $(10^{20} - 10^{21}) \text{ cm}^{-3}$. For In and Tl-doped systems, PF/τ is comparable to pristine around 10^{21} cm^{-3} . Any improvement in PF/τ is associated with the increment in S which is similar to what observed in doped systems corresponding to Cu_1 -site. Furthermore, ZT_e is plotted for these systems as a function of carrier concentration (Fig. 3.5 (j)) which is independent of τ . ZT_e shows features that are similar to the case when the dopants occupy Cu_1 -site.

3.4 Summary

In conclusion, we have studied the effect of substitutional doping by group 13 elements on electronic and transport properties of BaCu_2Se_2 . Our calculations of formation energy show that the dopants prefer Cu_1 and Cu_2 -site. From DOS calculations, we find the formation of resonant states at the bottom of the conduction bands arising from the p -orbitals of dopants. Transport calculations have shown that Al and Ga-doped systems (at Cu_1 -site) significantly improve Seebeck coefficient with electron doping when chemical potential touches the resonant states, thereby increasing PF/τ of these systems compared to pristine system. In similar manner, we have observed enhancement in transport properties with Al doping at Cu_2 -site, whereas other doped configurations attain optimized power factor values comparable to pristine system. Though the enhancement in S and PF/τ results in enhancement of ZT_e at low carrier concentration; at higher carrier concentration the enhanced κ_e/τ reduces ZT_e drastically.

Chapter 4

First Principles Investigations of Structural, Electronic and Transport Properties of BiI₃/ZrS₂ van der Waals Heterostructure[†]

4.1 Introduction

Based on theoretical calculations, Dresselhaus *et al.* predicted that reducing the dimensionality can significantly enhance the power factor and thereby ZT compared to their bulk counterparts. [20, 21] Following their predictions researchers have developed novel routes like adopted nanostructuring [110–115], band structure engineering, [116] to enhance the power factor. This has led to a large family of thermoelectric materials based on metal chalcogenides (Bi₂Te₃, Sb₂Te₃ and PbTe), superionic conductors, metal oxides, SiGe alloys, etc. [117] Additionally, with the advancement in nanotechnology, several low-dimensional materials apart from graphene are being prepared with improved and/or novel properties. Amongst them phosphorene [118], transition metal dichalcogenides (TMDC) [119–122], have been predicted to be possible candidates for thermoelectric applications. In a recent work Lv *et al.* predicted that ZrS₂ monolayer, which belongs to the family of TMDC and has a low lattice thermal conductivity, shows a high ZT value [56]. They further showed that the Seebeck coefficient can be increased by engineering the band structure through strain, which results in an increased value of ZT .

[†]Reprinted with permission from *Journal of Electronic Materials*, 50, 1644-1654, (2021). Copyright ©2021, Springer Nature.

In addition to TMDCs, there has been a relatively new family of materials with a chemical formula of MX_3 , where X is a halide ion and M is a metal atom. Recently, there has been great interest in investigating its physical properties [60–64]. Recent calculations by Liu *et al.* on MX_3 (where M=Sc, Y, As, Sb, and Bi) showed that these are semiconductors [64]. Amongst them, BiI_3 is particularly interesting because of the presence of a Mexican hat like band structure in the valence band that might lead to high value of Seebeck coefficient [65]. Moreover, it has been predicted that BiI_3 has a very low value of thermal conductivity [66]. However, it has a large value of effective masses for holes and a band gap that is larger compared to other semiconductors that are typically used for TE devices. These two properties might be detrimental for their performance as a thermoelectric device.

One of the ways to improve material properties is to form van der Waals heterostructures. There have been many reports of such heterostructures (HS) that show enhanced transport properties. For example, Mohanta *et al.* showed that forming vertical heterostructures of boron monosulphide with MoS_2 show an enhanced value of ZT [123]. Nguyen *et al.* showed that vertical HS of graphene layers show a larger value of ZT due to reduced thermal conductivity [124]. In addition to vertical HS there are also efforts to form lateral HS of layered materials to improve ZT . For example Ding *et al.* produced a two-dimensional superlattice-monolayer structure of $\text{ZrSe}_2/\text{HfSe}_2$ with a highly degenerate conduction level, which gives a high n-type power factor [125].

Based on the encouraging results reported in the previous studies, in this chapter, we have studied the structure, electronic and transport properties of vertical HS of $\text{ZrS}_2/\text{BiI}_3$. Besides the interesting properties of each individual component mentioned in the previous paragraphs, we also note that the lattice parameters of BiI_3 monolayer is twice that of ZrS_2 . Hence a (2×2) supercell of ZrS_2 is perfectly lattice matched with that of a (1×1) supercell of BiI_3 . Moreover, based on the positions of the valence and conduction band edges of the individual components, as reported in the literature [56,63], we show that the HS will most probably form a Type-II heterojunction, thereby having a smaller band gap compared to the parent components. This suggests that it may be interesting to investigate the properties of the HS for thermoelectric applications. The rest of the chapter is as follows: Section 4.2 contains the computational details. The results are summarized in Section 4.3. Finally we conclude in Section 4.4.

4.2 Computational details

The calculations in the present chapter are performed using the Quantum ESPRESSO software, which is a plane-wave based implementation of density functional theory. [102, 103] The electronic exchange and correlation potential was described by the generalized gradient approximation (GGA) as parametrized by Perdew, Burke and Ernzerhof (PBE). [79] We have used ultrasoft pseudopotentials to account for the electron-ion interactions. [82] The pseudopotentials have been generated using $4s^2 4p^6 4d^2 5s^2$, $2p^6 3s^2 3p^4$, $4d^{10} 5s^2 5p^5$ and $4f^{14} 5d^{10} 6s^2 6p^2$ valence configurations for Zr, S, I and Bi respectively. The kinetic energy cutoffs for wavefunction and charge density used for the calculation are 80 Ry and 800 Ry respectively. To sample the Brillouin zone (BZ), we used a $(9 \times 9 \times 1)$ Monkhorst-Pack k -mesh. [80]

Since we are using periodic boundary conditions, to avoid the spurious interactions between the periodic images we used 22 Å vacuum along the direction perpendicular to the plane of the monolayers and the heterostructure (z-axis of the unit cell in this case).

Earlier studies have shown that van der Waals interactions are important for these systems [63]. However, these are not accounted for within the PBE exchange correlation functional. Hence we used the semi-empirical Grimme-D2 van der Waals (vdW) corrections in all the calculations. [2]. The vdW radius and the C_6 coefficients used in our calculations for each of the atomic species are listed in Table 4.1. Additionally, Bi and I are heavy atoms, spin orbit interactions (SOI) are important. To correctly account for the SOI, the Kohn-Sham equations were solved self consistently using fully relativistic ultrasoft pseudopotentials. [126, 127]. Further, standard PBE functionals are also known to severely underestimate the band gap. Since we are interested in transport properties of these materials and the latter in turn depends on the band gap, it is important to compute the band gap with reasonable accuracy. For that purpose the band structures for the monolayers and heterostructures were computed using the singularity free Gaussian-attenuating Perdew-Burke-Ernzerhof (Gau-PBE) hybrid functionals [109]. To include the SOC effects along with the hybrid functional calculations, we used norm-conserving pseudopotentials with a plane wave cut off of 125 Ry for Gau-PBE calculations [81]. The matrix elements of the Fock operator have been evaluated with a $3 \times 3 \times 1$ q -mesh.

Table 4.1: van der Waals radius (r_{vdW}) and the C_6 coefficients for the different atomic species used in the Grimme-D2 vdW corrections. These values are taken from Ref. [2].

Atomic species	r_{vdW} (bohr)	C_6 (Ry/bohr ⁶)
Bi	3.586	2204.274
I	3.575	1092.775
Zr	3.097	855.833
S	3.180	193.230

For transport property calculations, we used the BoltzTraP package, [93] which solves the semi-classical Boltzmann transport equation (BTE) within the rigid band (RB) and constant relaxation time approximations (CRTA) [93]. While within the CRTA it is assumed that the relaxation time (τ) is same for all the electronic states, RB approximation considers that doping the material does not alter band dispersion and only results in a shift of the chemical potential of the system. For transport properties, we used $(57 \times 57 \times 1)$ k -point grid to obtain the Kohn-Sham eigenvalues, which are further fed into BoltzTraP code to yield transport properties.

Computation of τ : In addition to the CRTA, the BoltzTraP code computes the transport properties in terms of τ . Hence to know absolute values of the transport coefficients, we must compute τ . τ depends on several factors like electron-phonon coupling, scattering by defects and disorders. However, computing these from first principles is either difficult or for some cases impossible. The contribution to τ from electron-phonon coupling can be obtained from first-principles calculations. However, for our case, particularly for the HS, the unit cell is quite large. This coupled with the fact that we must include SOC, made direct computation of τ impossible with our limited computational resources. Hence, in this chapter, we used the deformation potential theory, together with the effective mass approximation to obtain the phonon-limited mobility μ_{2D} from which we computed τ using the following equation:

$$\mu_{2D} = \frac{e\tau}{m^*} \quad (4.1)$$

where e is the charge of an electron and m^* is the effective mass of an electron. μ_{2D} is given by:

$$\mu_{2D} = \frac{e\hbar^3 C}{k_B T m^* m_d E_{dp}^2} \quad (4.2)$$

where C is the 2D elastic constant, $m_d = \sqrt{m_x^* m_y^*}$ is the average effective mass. $C = \frac{\partial^2 E}{\partial \delta^2} \frac{1}{A_0}$ is the elastic modulus of the 2D material. A_0 is the area of the surface unit cell. To compute C we applied uniaxial strain (δ) along the a direction and computed the total energy E of the strained system. From this we computed the second derivative of total energy with respect to strain at $\delta = 0$. The deformation potential (E_{dp}) is given by $E_{dp} = \partial E_{edge} / \partial \delta$, where E_{edge} is the edge of the valence and conduction band. In order to compute E_{dp} we computed the band structure of the system both under compressive and tensile strain. From the band structure we plotted E_{edge} as a function of strain. The plot is fitted to an equation of a straight line, the slope of which gives the value of E_{dp} . Therefore from Eqn 4.1 and 4.2 we get:

$$\tau = \frac{\hbar^3 C}{k_B T m_d E_{dp}^2}. \quad (4.3)$$

4.3 Results and discussion

4.3.1 Structure and energetics

In bulk, both ZrS_2 and BiI_3 form layered structures, which are held together through weak van der Waals (vdW) interaction. Each layer of ZrS_2 (BiI_3) comprises of three atomic layers where the atomic layer contains metal atoms, i.e. Zr (Bi) is sandwiched between two atomic layers of S (I). The three atomic layers (S-Zr-S of ZrS_2 and I-Bi-I of BiI_3) are stacked in an ABC pattern such that each of the metal cations are at the centre of the octahedron formed by the anions. Though both bulk ZrS_2 and BiI_3 belong to the hexagonal crystal system, their space groups are different. While the former has a $P\bar{3}m1$ space group, the later belongs to the $R\bar{3}$ space group. A monolayer of these materials forms a two-dimensional hexagonal unit cell (Fig. 4.1). Our calculations, at the level of PBE+vdW+SOC yield lattice parameters of 3.64 Å for a monolayer of ZrS_2 (ML- ZrS_2) and 7.41 Å for a monolayer of BiI_3 (ML- BiI_3). We note that these are in excellent agreement with previous literature reports [63] [128] [56]. The Zr-S (Bi-I) bond lengths are 2.56 Å (3.11 Å). Further the thickness of each ML, calculated by measuring the distance between the two anionic layers along the z -direction, is about 2.94 Å and 3.62 Å for ZrS_2 and BiI_3 respectively.

In order to make the vertical heterostructure, i.e., where one layer is stacked over another,

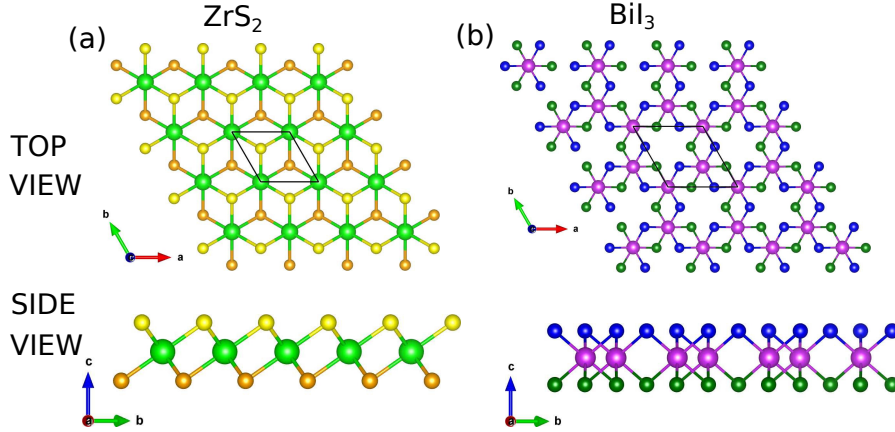


Figure 4.1: The top and side views of the structures of a monolayer of (a) ZrS_2 and (b) BiI_3 . The two-dimensional unit cell for each case is denoted by a black parallelogram. The large light green and violet spheres denote Zr and Bi ions respectively. The S (I) atoms in the top and bottom layers of ZrS_2 (BiI_3) are represented with yellow (blue) and golden (green) spheres respectively.

we begin by noting that the (2×2) 2D unit cell of ZrS_2 is almost lattice matched with the (1×1) unit cell of BiI_3 . The mismatch between the two is about 2%, with the ZrS_2 layer slightly smaller than BiI_3 . Hence, when the HS is to be constructed with the lattice parameter of BiI_3 , the ZrS_2 layer experience a tensile strain. Similarly, when the HS is to be constructed with ZrS_2 lattice parameter, the BiI_3 layer experiences a compressive strain. To minimize this strain due to the lattice mismatch, we further optimized the lattice parameter of the HS. Moreover, depending on the way the 2 MLs are stacked to form the HS, there are three non-equivalent configurations. To explain the stacking, we label the three sublayers of ML- ZrS_2 by A, B and C and that of ML- BiI_3 by A' , B' and C' as displayed in Fig. 4.2(a). Additionally, we define sulphur (iodine) atoms belonging to sublayers C (C') and A (A') as S_{up} (I_{up}) and S_{down} (I_{down}) respectively. In the $B'BC$ configuration each of the B' atoms (Bi atoms) of BiI_3 is placed on the B and C atoms of ZrS_2 , i.e., on the Zr (in sub-layer B) and S_{up} (in sub-layer C) of ML- ZrS_2 as shown by dotted lines in Fig. 4.2(a) and (b). The $B'BA$ configuration is generated by placing each of the B' atoms of ML- BiI_3 on the B and A atoms of ZrS_2 , i.e., on Zr and S_{down} belonging to ML- ZrS_2 (Fig.4.2 (c,d)). In the $B'AC$ configuration the two B' atoms (Bi) of ML- BiI_3 are placed on the A and C atoms (S_{down} belonging to A sublayer and S_{up} belonging to C sublayer, respectively) of ML- ZrS_2 as depicted in Fig. 4.2 (e,f).

In order to compare the thermodynamic stability of the HS and to determine the lowest energy configuration we have computed the binding energy (E_{BE}) of the heterostructure.

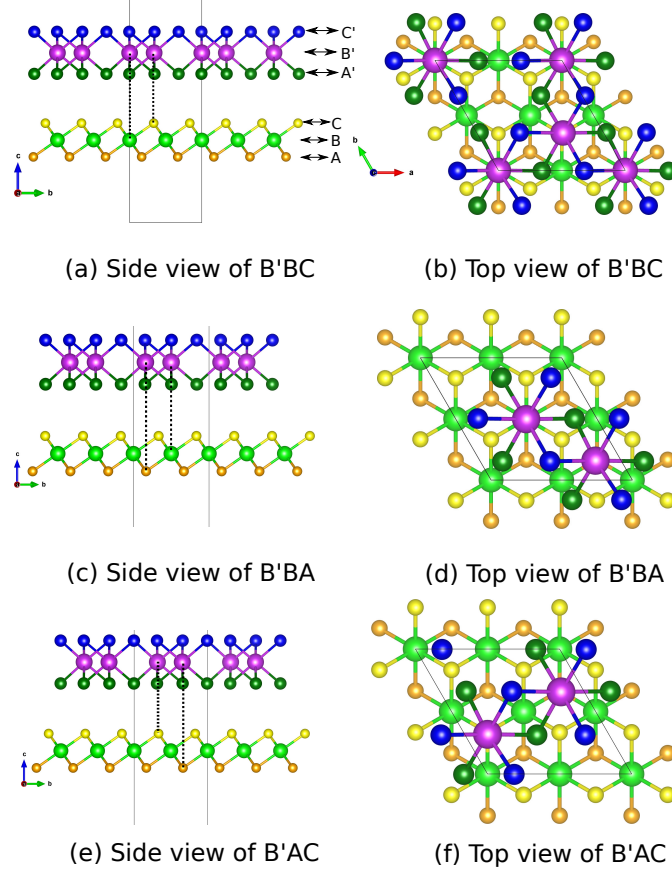


Figure 4.2: The side (a,c and e) and top view (b,d and f) for HS-BiI₃/ZrS₂ in configurations (B'BC, B'BA and B'AC, respectively). The Bi, Zr, I_{up}, I_{down}, S_{up} and S_{down} atoms are represented by violet, light green, blue, dark green, yellow and golden colored spheres, respectively.

E_{BE} is given by:

$$E_{BE} = \frac{E_{HS} - E_{BiI_3} - E_{ZrS_2}}{A}, \quad (4.4)$$

where E_{HS} , E_{BiI_3} and E_{ZrS_2} are the total energies of the HS, BiI₃, and ZrS₂, respectively. A denotes the area of the HS unit cell. The binding energy and the optimized lattice parameter for each of the three configurations are listed in Table 4.2. We find that all the 3 configurations of the HS have the same lattice parameter; 7.30 Å. The B'BC configuration is lowest in energy with a binding energy of -0.165 J/Å². We note that the B'AC and B'BA are about 18 and 2 meV higher in energy than that of the B'BC configuration. Similar values of the binding energy were also observed in HS of graphene and BiI₃. [128].

The separation between the two layers in the HS is about 3.46 Å. Similar separation is also observed in other HS, for eg. between graphene/BiI₃, MX₂/MX₂ (M=Zr,Hf and X=S,Se)

Table 4.2: The lattice parameters (a) and binding energy per unit area (E_{BE}) of the three possible configurations of the HS-BiI₃/ZrS₂ obtained with PBE+vdW+SOC.

Configuration	a (Å)	E_{BE} (J/Å ²)
B'BC	7.30	-0.165
B'AC	7.30	-0.164
B'BA	7.30	-0.159

and transition metal dichalcogenides. [128] [129] [130] The thickness of the ZrS₂ and BiI₃ in the HS are 2.94 Å and 3.76 Å respectively. While the thickness of ZrS₂ in the HS remains unchanged compared to that observed in the monolayer, for BiI₃ it increases by 0.14 Å up on the formation of the HS. This increase in thickness of the BiI₃ layer in the heterostructure can be attributed to the in-plane compressive strain the BiI₃ layer experiences due to the formation of the HS (lattice parameter of the HS is 7.30 Å while that of the BiI₃ monolayer is 7.41 Å). The Bi-I bond length in the heterostructure is about 3.10 Å and is similar to that observed in the BiI₃ monolayer. Within the ZrS₂ layer in the heterostructure, the Zr-S bond lengths are similar to that observed in the ZrS₂ monolayer.

4.3.2 Electronic properties

As mentioned in the previous section, all three configurations of the HS are similar in energy. Hence, for the study of the electronic and transport properties we used the B'BC configuration.

Fig. 4.3 shows the band structures of ZrS₂, BiI₃ and HS calculated with PBE (blue lines) and Gau-PBE (red lines) functionals. For both the functionals we used vdW corrections and have incorporated SOC interactions. The monolayers have indirect band gaps as seen in Fig. 4.3(a) and (b). ZrS₂ has a band gap of 1.00 eV at PBE level, with the valence band maxima (VBM) at the Γ point of the BZ and the conduction band minima at the M -point (Fig. 4.3(b)). In contrast, BiI₃ has a band gap that is about 0.36 eV larger than that of ZrS₂. For the former, the VBM lies along the $\Gamma \rightarrow M$ direction of the BZ while the CBM is at the Γ point (Fig. 4.3(b)). Additionally we find another maxima that is very close in energy to the VBM along the $\Gamma \rightarrow K$ direction. Moreover, as mentioned in the introduction, the valence band edge exhibits a Mexican-hat like structure in the dispersion of VBM around the Γ -point of the BZ. We note that similar band dispersion resulted in high values of Seebeck coefficient for holes in other materials [131]. The major effect

of the hybrid functional is the shift in the positions of the CBM and VBM that results in an increase in the band gap. However, we observe a larger increase in the band gap for ZrS_2 compared to BiI_3 . For example, while for BiI_3 the band gap increases to 1.64 eV with Gau-PBE functional (0.28 eV increase), the band gap for ZrS_2 also increases to 1.91 eV (about 0.9 eV increase). This can be attributed to the fact that both the valence and conduction bands of ZrS_2 are more shifted compared to that of BiI_3 . Unlike BiI_3 where the VBM and CBM are shifted by about 0.14 eV each, for ZrS_2 we observe a shift of 0.41 eV each for the VBM and CBM. The band dispersion is more or less similar to that obtained with PBE (red curves in Fig. 4.3).

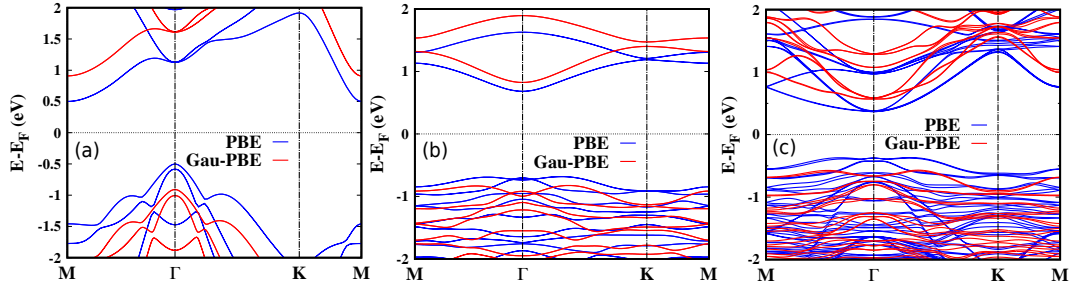


Figure 4.3: The electronic band structure computed using PBE (blue) and Gau-PBE (red) functionals for monolayers of ZrS_2 (a), BiI_3 (b) and the B'BC configuration of the HS(c). The Fermi energy is set to zero.

We compared our computed values of the band gaps of the monolayers with those reported in literature (PBE, HSE-functional and GW calculations) in Table 4.3. For the ZrS_2 , our PBE results are in excellent agreement with the corresponding ones in the literature [56, 132]. While in the literature, most studies used the HSE functionals we used Gau-PBE functionals. We find that the values of the band-gap obtained from our Gau-PBE calculations is about 0.25 eV smaller than those obtained with HSE [132]. However, our band gap is in excellent agreement with those obtained using more accurate GW calculations [133]. For BiI_3 , we find that our PBE band gaps are slightly smaller than those reported in literature [63, 128]. This is because in those studies vdW interactions have not been taken into account.

Upon the formation of the HS, we find that the VBM of the HS is localized on BiI_3 and the CBM is localized on ZrS_2 (Fig. 4.3). This is further corroborated by the plot of the band structure showing contributions from ZrS_2 and BiI_3 in Fig. 4.4(a). Although the band dispersions of the conduction and valence band look very similar to those of ZrS_2

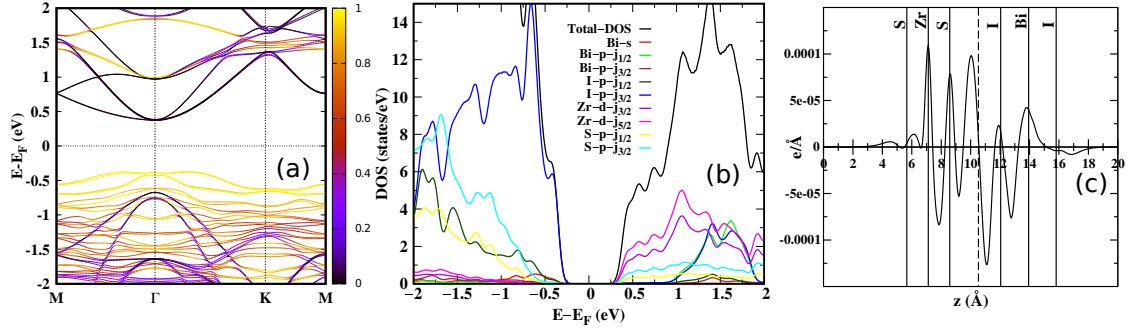


Figure 4.4: (a) The band structure of the HS projected on the BiI_3 electronic states. Black lines represent the bands arising from ZrS_2 and colored lines represent the bands arising from BiI_3 . (b) The density of states projected onto the atomic orbitals of Bi, Zr, I and S. Both are computed using PBE+vdW+SOC. (c) Planar average of the charge transfer due to the formation of the HS.

and BiI_3 monolayers respectively, a closer look at the band structure shows subtle differences, which as discussed in the next section can affect the transport properties of the HS. Fig. 4.5(a) shows the dispersion of the conduction band edge of the HS and ZrS_2 monolayer around the Γ -point. For ZrS_2 monolayer, there are six degenerate bands at the Γ point. On moving away from the CBM, they split into a set of 2 bands, the flatter one has a pair of degenerate bands while the second one has 4 bands. In contrast, in the heterostructure, the bands split weakly resulting into 3 sets of bands at the Γ point. Each of these have two degenerate bands. Additionally, we observe that the curvature of the bands also increases in the HS, compared with that in ZrS_2 monolayer. On comparing the valence band edge of the HS with that of BiI_3 monolayer (Fig. 4.5(b)), we find that the two almost degenerate maxima around the Γ -point show slight changes. In the HS, this degeneracy is broken and we observe a maxima along the $\Gamma \rightarrow K$ direction. Further, the Mexican-hat like dispersion observed in BiI_3 remains intact even in the HS. In contrast with the ZrS_2 ML, we find the CBM of the HS lies at the Γ -point of the BZ. The change in the position of the CBM in the BZ can be attributed to the folding of the BZ in the reciprocal space for the HS. We note that the unit cell of the HS in real (reciprocal) space is twice (half) that of ZrS_2 . As a result the M point of the larger BZ of ZrS_2 folds into the Γ -point of the smaller BZ of the HS.

The HS belongs to type-II with a PBE-band gap of about 0.72 eV (1.20 eV with Gau-PBE). Because of the staggered nature of the alignment of the bands of the individual components of the HS, we find that its band gap is significantly reduced compared to the individual monolayers. Additionally, we find that the weak interaction between the two

Table 4.3: The band gap (E_g , in eV) of BiI_3 , ZrS_2 and the B'BC configuration of the HS obtained with PBE and Gau-PBE hybrid functionals.

Systems	E_g (ours, PBE)	E_g (ours, Gau-PBE)	E_g (others, PBE)	E_g (others, HSE)	E_g (others, GW)	Exp.
ML- ZrS_2	1.01	1.91	1.02 [132], 1.10 [56]	2.16 [132]	1.95 [133]	-
ML- BiI_3	1.43	1.64	1.55 [63], 1.57 [128]	2.21 [63]	-	2.8 [134]
HS- $\text{BiI}_3/\text{ZrS}_2$	0.72	1.20	-	-	-	-

ML results in small amount of charge transfer (Fig. 4.4(c)) from BiI_3 to ZrS_2 . As a result the occupied BiI_3 states move closer to the Fermi level. Further, the density of states (DOS) projected onto the atomic orbitals (Fig. 4.4(b)) show that the VBM of the HS has states comprising primarily from I- p orbitals while the CBM have major contributions from Zr- d orbitals.

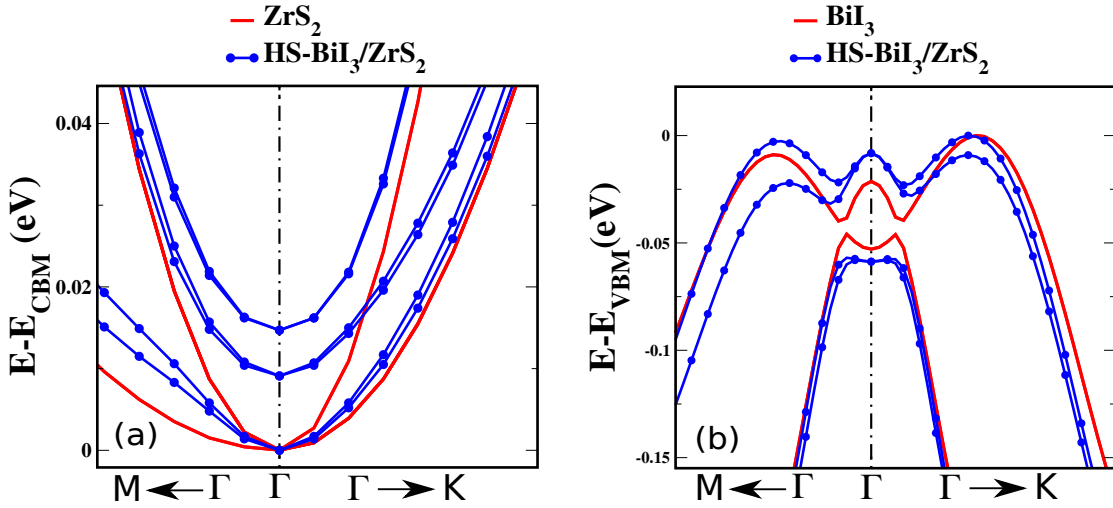


Figure 4.5: Magnified view of the band structure around (a) the conduction band minima and (b) valence band maxima of the HS. For sake of comparison, also shown in (a) and (b) the same for ZrS_2 and BiI_3 monolayers respectively. For both the cases, the bands are shifted with respect to the minima and maxima respectively.

4.3.3 Computation of relaxation time

Table 4.4 lists the values of C , m^* , E_{dp} and τ for the three systems. Since C and E_{dp} are related to the acoustic phonons, we note that the computation of τ by the above mentioned method ignores the contributions coming from coupling of optical phonons with the electrons. Amongst the three systems, we find that BiI_3 has the lowest value of C while the HS has the largest. The same for ZrS_2 lies at an intermediate value. The larger value of C for the HS compared to that of the individual monolayers can be attributed to

Table 4.4: C , m^* , E_{dp} and τ for the electrons and holes in ZrS₂ and BiI₃ monolayers and in the HS.

System		C (eV/Å ²)	m^* (zigzag) (m_e)	m^* (armchair) (m_e)	E_{dp} eV	$T = 300$ K	$T = 400$ K	$T = 500$ K
		τ (10^{-14} s)						
ZrS ₂	electron	6.04	0.28	1.97	-3.47	13.10	9.83	7.86
	hole		0.23	0.27	-9.18	5.58	4.18	3.35
BiI ₃	electron	1.29	2.06	0.50	-5.14	0.93	0.70	0.56
	hole		0.59	1.16	-6.08	0.82	0.61	0.49
HS	electron	7.42	0.29	0.56	-3.81	24.60	18.50	14.80
	hole		0.68	1.10	-8.79	2.15	1.62	1.29

the strain in the monolayers due to formation of the HS and the van der Waals interaction between them. We note that similar enhanced strain was also observed in heterostructures of MoS₂/WS₂ [135] and graphene/MoS₂ [136]. Further, the negative sign of E_{dp} for both the valence and conduction band implies that upon deformation, both the band edges go down in energy. The magnitude of E_{dp} is an indication of the strength of electron-phonon coupling in these systems. A comparison of $|E_{dp}|$ between the holes and electrons suggests that holes couple more strongly with the lattice vibrations compared to electrons. In the heterostructure, the $|E_{dp}|$ for electrons (holes) are similar to that of ZrS₂ (BiI₃).

The effective masses show significant amount of anisotropy based on transport direction. While for BiI₃, m^* for electrons has the largest value along the zigzag direction, for ZrS₂ it is heaviest along the armchair direction. In BiI₃ the holes are heaviest along the armchair direction. In contrast, in ZrS₂, along both the directions, the holes have a lighter mass. For the HS, it is expected that the effective masses of electrons (holes) will be similar to that of ZrS₂ (BiI₃). From Table 4.4 we find that the effective mass of electrons along the zigzag direction is indeed similar to that of ZrS₂. However, along the armchair direction we find that the electron effective mass is significantly reduced compared to that in ZrS₂ along the same direction. This can be attributed to the changes in the band dispersion observed in the conduction band of the HS due to the interactions between ZrS₂ and BiI₃. For the holes, as per our expectation, we find that the effective masses are close to that observed in BiI₃.

The combined effect of C , m^* , E_{dp} results in smallest value of relaxation time in BiI₃ for both electrons and holes. Amongst the three systems, the electrons in the HS have the largest value of τ . This is primarily because of the reduction of the effective masses of electrons in the HS along the armchair direction. For holes largest value of τ is observed

in ZrS₂ monolayer. Further, the relaxation time decreases with increase in temperature.

4.3.4 Electronic transport properties

Based on the electronic structure of the three materials we now evaluate the transport coefficients of these three materials by solving the Boltzmann transport equations. Fig. 4.6 shows the plots of the Seebeck coefficient (α) as a function of chemical potential. Fig. 4.7 (Fig. 4.8) shows the plots for electrical conductivity (σ), power factor ($PF = \alpha^2\sigma$) and (κ_e) for the three systems for holes (electrons). These properties have been computed using the band dispersion obtained from PBE calculations. The PBE band gap has been corrected with the Gau-PBE one for each of the cases.

Near the band edges, we observe that the maximum values of α is similar for all three cases varying between 1.81 and 3.15 mV/K for holes and electrons at 300 K (Fig. 4.7(a)-(c)). With other factors remaining constant, it is usually expected that a larger band gap will result in a greater value of Seebeck coefficient at the band edges. This is because the magnitude of S for non-degenerate semiconductors depends on the distance between the energy at which S is computed and the Fermi level (E_F), the latter is typically close to the middle of the band gap. We note that though ZrS₂ has a larger band gap than BiI₃ and the HS, we find that the Seebeck coefficients for the three systems are comparable. This can be attributed to the fact that even though the latter two have a smaller band gaps than ZrS₂, they have a Mexican-hat like structure at the valence band edge, that gives rise to three, almost degenerate, maxima. In contrast, for ZrS₂, there is just one maximum. This results in increase of density of states at the valence band edge for BiI₃ and the HS, that inturn increases the value of α . Moreover, compared with that of the monolayers, for the HS the Seebeck coefficient decreases more rapidly with higher value of chemical potential, i.e. increase in carrier concentration. On increasing the temperature, we find that there is a reduction of the Seebeck coefficient for all the cases.

Compared to BiI₃, the σ values for ZrS₂ are larger for both electrons and holes (Fig. 4.7(a),(b) and Fig. 4.8(a),(b)). However, due to larger band gap of ZrS₂, we observe that the peaks in the σ plots occur at higher value of chemical potential. This implies that larger number of charge carriers are necessary to achieve electrical conductivity in ZrS₂ than in BiI₃. For example, while in BiI₃, the first peak in σ for holes is at $\mu = -0.96$ eV (9.88×10^{14} cm⁻² carrier concentration), for ZrS₂ the same occurs at 1.54 eV, corresponding to a car-

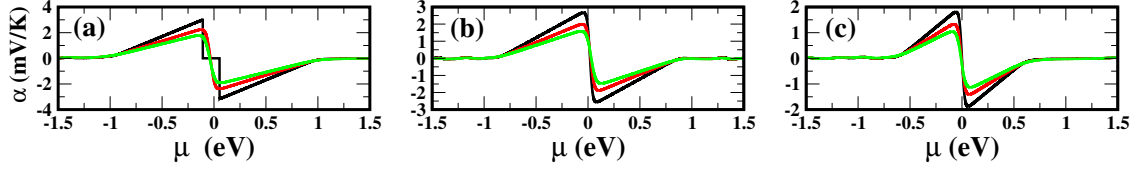


Figure 4.6: Seebeck coefficient (α) as a function of chemical potential (μ) in (a) ZrS_2 , (b) BiI_3 and (c) HS. The black, red and green plots are at 300 K, 400 K and 500 K respectively. Negative (Positive) values of μ denote holes (electrons).

rier concentration of $1.69 \times 10^{15} \text{ cm}^{-2}$. The holes in the HS reside in BiI_3 and since the dispersion of the valence band is similar in both the cases, one would have expected that the σ values for the holes in HS should be closer to that observed in BiI_3 . However, we observe that in HS σ is one order of magnitude larger than that in BiI_3 (Fig. 4.7(b) and (c)). This can be attributed to the faster relaxation times of holes in the HS. Amongst the three materials considered in this chapter, for holes, it is observed that ZrS_2 shows largest value of σ (Fig. 4.7(a)). For the electrons, amongst the three systems, the HS shows the largest value of σ . In fact σ of electrons in the HS is one order of magnitude larger than that observed in ZrS_2 and three order of magnitude larger than that observed in BiI_3 (Fig. 4.8(a), (b) and (c)). Since the band gap of the HS is significantly smaller than that of the individual monolayers, we observe the peaks in the conductivity at lower value of the chemical potential. For example, for holes, the first peak is at -0.74 eV , corresponding to that of $2.86 \times 10^{14} \text{ cm}^{-2}$ while for electrons, the first peak is observed at 1.14 eV corresponding to a carrier concentration of $6.71 \times 10^{14} \text{ cm}^{-2}$.

Further, to separate out the effects of the band gap and τ on the conductivity of the charge carriers in the HS, in Fig. 4.9 we have plotted σ of the HS as a function of the chemical potential using the band gaps and τ 's of the individual components of the HS. Since the holes reside in BiI_3 , we have computed σ for HS with band gap of BiI_3 and τ_{HS} and also with band gap of HS and τ_{BiI_3} (Fig. 4.9(a)). Similarly for electrons, we have used the band gap and τ of ZrS_2 (Fig. 4.9(b)). A comparison of the σ plot computed with the band gap of the HS and τ_{HS} (black line in Fig. 4.9(a)) with that calculated with the band gap of BiI_3 and τ_{HS} (red line in Fig. 4.9(a)) shows that the primary effect of the reduced band gap of the HS is that it changes the doping concentration at which one can observe a given value of conductivity. The plot with a larger band gap shifts to higher (in magnitude) value of μ . In contrast, when we compare the σ computed with the band gap and τ of the HS (black line in Fig. 4.9(a)) with that calculated with the band gap of HS

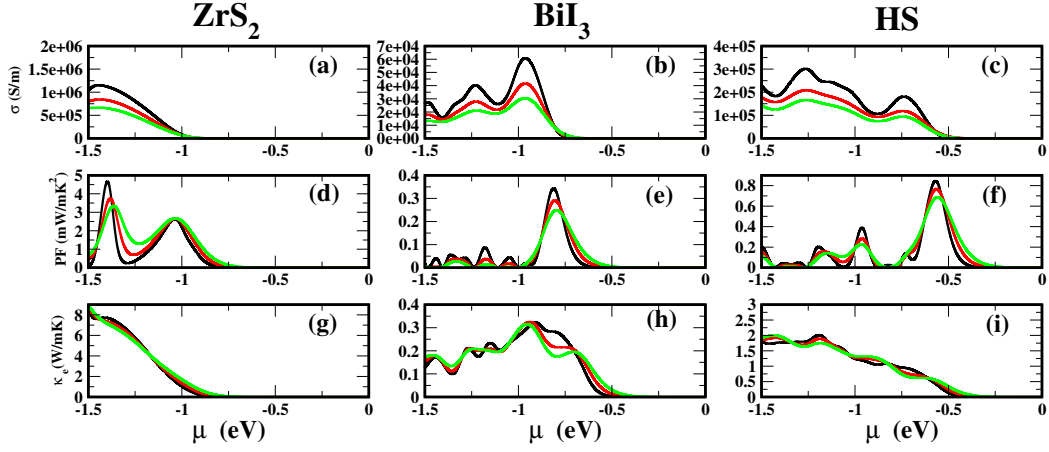


Figure 4.7: Electronic conductivity, σ (a, b, c), power factor PF (d, e, f) and electronic contribution to thermal conductivity, κ_e (g, h, i) for holes as a function of the chemical potential (μ) at three different temperatures, namely 300 K, 400 K and 500 K. The first, second and third columns are results for ZrS_2 , BiI_3 and the HS respectively.

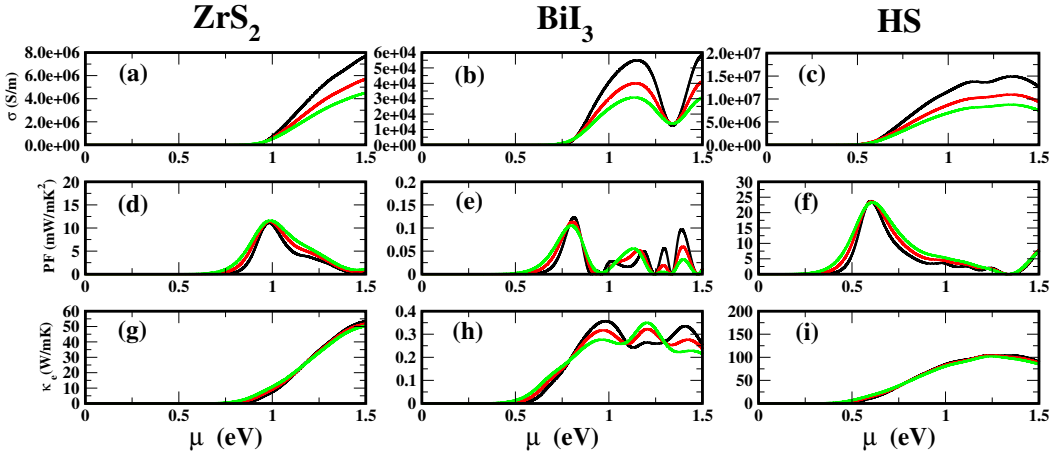


Figure 4.8: Electronic conductivity, σ (a, b, c), power factor PF (d, e, f) and electronic contribution to thermal conductivity, κ_e (g, h, i) for electrons as a function of the chemical potential (μ) at three different temperatures, namely 300 K, 400 K and 500 K. The first, second and third columns are results for ZrS_2 , BiI_3 and the HS respectively.

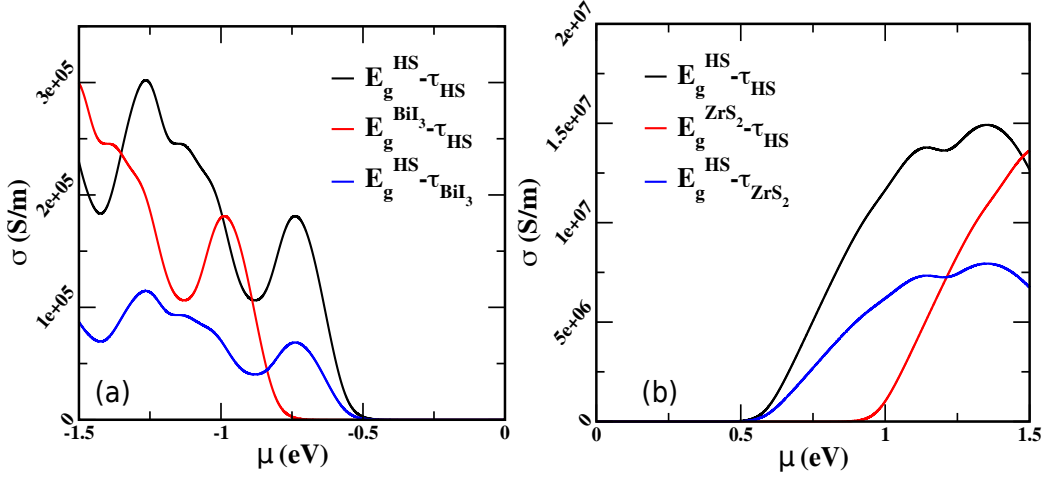


Figure 4.9: Effect of τ and band gap on σ of holes (a) and electrons (b). In the figure legend, E_g denotes band gap and τ denotes the relaxation time.

and τ_{BiI_3} (blue line in Fig. 4.9(a)) we observe that the magnitude of σ changes because the τ 's are different in the two cases. Similar effect is also observed for electrons (Fig. 4.9(b)).

The power-factor is a good measure of a thermoelectric performance of a device. Fig. 4.7(d)-(f) and Fig. 4.8 (d)-(f) show the variation of PF with μ for the three cases. Analogous to the conductivity plots, we find that for the monolayers, the PF for both the electrons and holes are larger in ZrS_2 than in BiI_3 . In ZrS_2 the PF for the holes are smaller than that observed for electrons, while in BiI_3 they are comparable. For the HS, the PF values of the electrons are not only larger than that of the holes, but also they are largest compared to the individual monolayers. This suggests that the heterostructure might show an improved performance over its individual monolayers as a n -type thermoelectric. Further, in comparison with the monolayers, we can achieve a large value of PF at lower carrier concentration. For example, for holes, the first peak in PF observed in ZrS_2 and BiI_3 corresponds to $1.25 \times 10^{15} \text{ cm}^{-2}$ and $4.72 \times 10^{14} \text{ cm}^{-2}$ holes respectively, while in the HS, values of PF similar to that of BiI_3 can be observed at $3.75 \times 10^{13} \text{ cm}^{-2}$ holes. The corresponding numbers for electrons are $4.41 \times 10^{14} \text{ cm}^{-2}$ and $2.36 \times 10^{14} \text{ cm}^{-2}$ for ZrS_2 and BiI_3 respectively compared with that of $2.81 \times 10^{13} \text{ cm}^{-2}$ for the HS. In addition to the PF , we have computed the electronic contribution to the thermal conductivity (κ_e) for the three cases (Fig. 4.7(g)-(i) for holes and Fig. 4.8(g)-(i) for electrons). For all three cases, the behaviour is similar to that observed for σ .

4.4 Summary

In conclusion, we have investigated the electronic and transport properties of monolayers of ZrS_2 and BiI_3 and a vertical HS formed using them for plausible application for thermoelectric devices. While the individual materials have a large band gap, the HS forms a type II junction with a reduced band gap of 1.20 eV. This reduction in band gap results in significant amount of electrical conductivity and PF at low concentration of electrons and holes. Further, the interactions between the monolayers in the HS induce subtle changes in the band dispersion such that electron effective masses are significantly different in the HS than in ZrS_2 monolayer. Moreover from the calculation of deformation potential and two dimensional elastic constants, we find that the phonons of the HS are hardened compared to that of the individual monolayer. All these changes in the electronic and structural properties of the HS results in significantly different relaxation times of charge carriers in the HS compared to that of ZrS_2 or BiI_3 . Further, these are also reflected in their transport properties. In particular, we find that for the electrons in the HS, the power factor is 2 and 100 times larger than those observed in ZrS_2 and BiI_3 . This suggests that the maximum power output from a device made with n-doped heterostructure will be larger than that of the individual components. This suggests that the HS is a plausible candidate for an n-type thermoelectric. However, we note that the efficiency of the device needs to be tested by computing ZT , computation of which is beyond the scope of the present study. We hope that our results will motivate further experimental and theoretical studies on this HS.

Chapter 5

Effect of Electron-Phonon Coupling on Transport Properties of Monolayers of ZrS_2 , and BiI_3 : A thermoelectric Perspective

5.1 Introduction

From the perspective of designing novel materials with higher ZT or improving ZT of existing thermoelectric materials, computational material design can play a significant role [66, 137–139]. For *in silico* search of novel thermoelectric materials it is necessary to compute the transport coefficients, which is done by solving the semiclassical Boltzmann transport equations. However, to do so one not only needs to compute the electronic structure of the material but also the relaxation time (τ) of the carriers. With the advent of fast computers, computing a reasonably accurate electronic structure *ab initio* is relatively simpler. Yet, computing the carrier relaxation time from first principles is challenging. Hence one usually resorts to approximations. One of the most commonly used approximations is the constant relaxation time approximation (CRTA) where it is assumed that the carrier relaxation time is independent of the electronic state of the carrier. Under this assumption one can compute σ and κ_e in terms of relaxation time. Nonetheless, for the simulations to have predictive capabilities, it is also necessary to have estimates of τ . Usually τ has a dominant dependence on electron-phonon coupling and is usually estimated from deformation potential theory. However, in this approximate method the effect of the coupling of the phonons with the electrons is incorporated through the elastic constants and change in the position of the band edges in response to applied strain. Both the elastic constants and the strain are connected to the acoustic mode of the system. Thus through this method one usually considers the coupling of the carriers with the acoustic modes of

the system.

In a recent work by Liao *et al.*, it has been shown that for the case of phosphorene monolayer, in addition to the acoustic modes, the optical modes also contribute significantly to the scattering of the carriers, thereby effecting its transport properties by orders of magnitude [140]. Moreover, they have also shown that in highly anisotropic materials, since the deformation along a specific direction can result in scattering along all directions the deformation potential theory is not applicable for such cases. For ionic solids, the displacement pattern associated with the optical modes induce oscillating dipole moments. It is expected that these dipole moments will couple strongly with the carriers [141] and hence ignoring their contribution to τ might result in erroneous predictions. However, still deformation theory is being used to compute τ for such solids [56]. Hence it is desirable to understand and quantify the effect of these approximations in computing the transport coefficients.

In an effort to achieve this, in this work we have studied the effect of electron-phonon coupling on the electronic and transport properties of two dimensional ionic materials, namely monolayers (MLs) of ZrS_2 and BiI_3 . The reason for choosing low dimensional materials in general is due to the fact that Dresselhaus *et al.* predicted enhancement of the power factor and thereby ZT through reduction of dimensionality. [20, 21] Following their predictions novel routes like adopted nanostructuring [110–115], band structure engineering, [116] etc. have been developed to enhance the power factor of thermoelectric materials. This has led to the development of large families of thermoelectric materials based on metal chalcogenides (Bi_2Te_3 , Sb_2Te_3 and PbTe), superionic conductors, metal oxides, SiGe alloys, etc. [117] These monolayers were chosen in particular because their bulk forms are known to have very low lattice thermal conductivity [66, 142]. Since the thermal conductivity is low, if the transport properties are conducive then these can have large values of ZT . Further these are ionic solids with a different degree of ionicity. The degree of ionicity for binary compounds can be estimated based on the difference in electronegativity ($\Delta|EN|$) of the two elements forming the compound. Based on the Pauling electronegativity scale of the different elements (See Table B.1 of Appendix B) we find that $\Delta|EN|$ for ZrS_2 and BiI_3 are 1.25 and 0.64 respectively, indicating that the Zr-S bonds in ZrS_2 have the largest ionic character, followed by the Bi-I bonds in BiI_3 . Hence, a comparison of the strength of electron-phonon coupling and transport properties

in these materials will also throw light on the effect of ionicity on the transport properties. In particular, here we have investigated the effect of electron-phonon coupling on the band structure and the carrier relaxation times of these materials and how these in turn affect their transport properties.

The rest of the chapter is divided as follows. Section 5.2 contains details of the calculations. The structure and vibrational properties of these monolayers are discussed in Section 5.3.1. In Section 5.3.2 we discuss the effect of electron-phonon coupling on the band structure. The results for computing the relaxation times explicitly considering electron-phonon coupling and deformation potential theory are presented in Section 5.3.3. The effects of the different approximations on the transport properties are discussed in Section 5.3.4. Finally we conclude in Section 5.4.

5.2 Computational details

DFT calculations: Our first principles calculations are based on density functional theory as implemented in the Quantum ESPRESSO software [102, 103]. Norm-conserving pseudopotentials [81] have been used to account for interactions between the valence electrons and ionic cores. Moreover, Bi and I being heavy atoms, spin orbit interactions (SOI) are important. To correctly account for the SOI, relativistic Kohn-Sham equations have been solved self consistently using fully relativistic norm conserving pseudopotentials [126] for the monolayers. The valence electronic configuration considered in our calculations for Zr, Bi, I and S are $4s^2 4p^6 4d^2 5s^2$, $4f^{14} 5d^{10} 6s^2 6p^2$, $4d^{10} 5s^2 5p^5$ and $2p^6 3s^2 3p^4$ respectively. The exchange-correlation potential of electrons was described by using the Perdew-Burke-Ernzerhof (PBE) form of generalized gradient approximation (GGA) [79]. We use an energy cutoff of 70 Ry and 145 Ry to truncate the plane wave basis used in calculating the Kohn-Sham wave-function for ML-ZrS₂ and ML-BiI₃ respectively. Previous computational studies of these monolayers indicated that van der Waals (vdW) interactions are important for them [63, 128, 132, 133]. Since PBE-GGA does not include the vdW interactions, so it was included in our calculations using the semi-empirical approach as proposed by Grimme [2] for ML-BiI₃, whereas no vdW correction is incorporated for the calculations of ML-ZrS₂ to compare our results with those of the study by Lv *et al.* [56]. Brillouin zone integrations are done using a Monkhorst-Pack [80] k -point grid of a $9 \times 9 \times 1$ grid for both the monolayers. To avoid the spurious interactions between periodic images in the

direction perpendicular to the plane of the ML (along z -direction in this case), we have used a vacuum of 13 Å along the z -direction. In order to ascertain the dynamical stability of the MLs and to compute the vibrational properties and electron-phonon coupling, we have used density functional perturbation theory [89]. The calculations have been carried out using a $5 \times 5 \times 1$ q -mesh for both the monolayers.

Electronic transport properties: To obtain the transport properties, we have solved the semiclassical Boltzmann transport equations within the rigid band approximation as implemented in the BoltzTraP code [93], where it uses a Fourier expansion scheme to fit the band structure for calculation of transport properties. A Γ -centred $15 \times 15 \times 1$ grid is introduced for both the monolayers to enable accurate Fourier interpolation of Kohn-Sham eigenvalues.

BoltzTraP can either compute σ/τ and κ_e/τ within the constant relaxation approximation (CRTA) or use explicitly relaxation times for each state and compute the transport properties (b-CRTA). Hence, to obtain absolute values of the transport coefficients, one needs to know the values of τ/τ_{nk} . τ depends on various factors like electron-phonon interactions (EPIs), defects, impurities, etc. Computing contributions to τ from first principles calculations for all the factors is challenging. However, the contribution to τ from EPIs can be computed in two ways. The average value of τ can be obtained using the deformation potential theory and the effective mass approximation. Using these, it can be shown that τ is given by:

$$\tau = \frac{\hbar^3 C}{k_B T m_d E_{dp}^2} \quad (5.1)$$

where C is the 2D elastic constant, m_d is the average effective mass, E_{dp} is the deformation potential, T is the temperature and k_B is the Boltzmann constant. $\hbar = h/2\pi$, h being the Planck's constant. The details of computing the various terms in the above equation has been described in Chapter 4 (Section 4.2) [143].

Computing τ using Eqn. 5.1 has two limitations: (a) it provides us with the average value of τ and (b) considers only the contributions from the acoustic modes. However, for those systems where scattering from optical modes are important this method will typically overestimate τ . Moreover in order to go beyond CRTA, τ for each nk is necessary. Hence to understand the effect of CRTA and the negligence of the contributions from the

scattering of the electrons/holes by optical phonons, we have explicitly calculated $\tau_{n,k}$ from the imaginary part of the electron self-energy. In addition to the relaxation time, the electron-phonon coupling also renormalizes the band structure and thereby the band gap and transport properties of the system. The band-structure renormalization can be obtained from the real part of the electron self-energy. The electron-self energy within the Migdal approximation are given by

$$\sum_{nk}^{EP} = \sum_{\mathbf{q}, m} w_{\mathbf{q}} |g_{mn, \nu}^{SE}(\mathbf{k}, \mathbf{q})|^2 \left[\frac{n_{\mathbf{q}\nu} + 1 - f_{m\mathbf{k}+\mathbf{q}}}{\epsilon_{n\mathbf{k}} - \epsilon_{m\mathbf{k}+\mathbf{q}} - \hbar\omega_{\mathbf{q}\nu} - i\delta} + \frac{n_{\mathbf{q}\nu} + f_{m\mathbf{k}+\mathbf{q}}}{\epsilon_{n\mathbf{k}} - \epsilon_{m\mathbf{k}+\mathbf{q}} + \hbar\omega_{\mathbf{q}\nu} - i\delta} \right] \quad (5.2)$$

where $g_{mn, \nu}^{SE}(\mathbf{k}, \mathbf{q}) = (\frac{\hbar}{2m_0\omega_{\mathbf{q}\nu}})^{1/2} \langle \psi_{m\mathbf{k}+\mathbf{q}} | \partial_{\mathbf{q}\nu} V | \psi_{n\mathbf{k}} \rangle$. $w_{\mathbf{q}}$ is the weight associated with phonon wavevector \mathbf{q} in the BZ, $\psi_{m\mathbf{k}}$ represents the electronic wavefunction for band m , wavevector \mathbf{k} , and eigenvalue $\epsilon_{n\mathbf{k}}$. $\partial_{\mathbf{q}\nu} V$ is the derivative of self consistent potential associated with a phonon of wavevector \mathbf{q} , branch index ν and frequency $\omega_{\mathbf{q}\nu}$. $f_{m\mathbf{k}+\mathbf{q}}$ ($n_{\mathbf{q}\nu}$) is the occupation of the electronic (vibrational) state and is given by the Fermi-Dirac (Bose-Einstein) distribution. The electron self-energies have been calculated using the EPW software [92]. The electron-phonon matrix elements are first computed using coarse k and q grids as mentioned in the previous paragraphs. These are then interpolated to a dense $300 \times 300 \times 1$ q -mesh for both the monolayers. We have used 25 meV Gaussian broadening to smear the δ function of equation:5.2 for the monolayers. We have considered the EP scattering rate due to acoustic and optical phonons in our calculation for all the monolayers. From the imaginary part of electron self-energy (\sum_{nk}^{EP}) the relaxation time for each state is calculated by using the relaxation $\tau_{nk} = \frac{\hbar}{2(\text{Im} \sum_{nk}^{EP})}$, where \hbar is reduced Planck constant. The normalized electronic eigenvalues (ϵ_{nk}^{RG}) is given by [85]:

$$\epsilon_{nk}^{RG} = \epsilon_{nk} + \text{Re} \sum_{nk}^{EP} \quad (5.3)$$

5.3 Results and discussion

5.3.1 Crystal structure and lattice vibrations.

Both the materials form layered structures in their bulk and belong to the hexagonal crystal system. ZrS₂ is known to possess $P\bar{3}m1$ symmetry, whereas BiI₃ belongs to the $R\bar{3}$ space

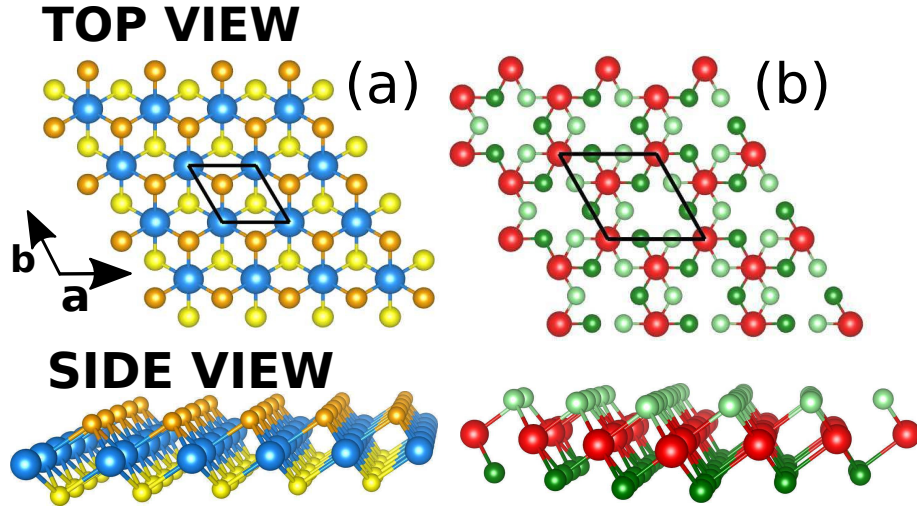


Figure 5.1: The top and the side view of (a) ML-ZrS₂ and (b) ML-BiI₃, where Sulfur (Iodine) is represented by light yellow (light green) and dark yellow (dark green) colored balls belonging to two different sublayers. Zr and Bi are shown by sky blue and red balls respectively.

group. Each layer of these materials is composed of three atomic layers with the metal atoms (Zr/Bi) sandwiched between two layers of S/I. These atomic layers are stacked in ABC form. Within each layer, the positively charged metal atoms occupy the centre of the octahedra formed by the anions (made of S or I). The layers are bound together through van der Waals interaction.

The top and side views of the relaxed structures of the monolayers are shown in Fig. 5.1. For ML-ZrS₂, we obtain a lattice parameter of 3.69 Å, which is in excellent agreement with that reported in previous studies. [56] The monolayer has a thickness (distance between the positions of the atoms in the two anionic layers) of 2.90 Å. The interlayer distance is about 3.70 Å and the Zr-S bond lengths are about 2.57 Å.

Our calculations yield a lattice parameter of 7.35 Å for the ML-BiI₃. Zhang *et al.*, using non-local vdW density functionals (optB88-vdW), obtained a lattice parameter of 7.59 Å. [63] Calculations performed by Fengxian *et al.* with DFT-D3 vdW corrections yield a lattice parameter of 7.64 Å. [128] We obtain the Bi-I bond lengths of 3.09 Å in the ML. The I-I and Bi-I distances are 3.68 Å and 1.84 Å respectively.

To check the dynamical stability, we have calculated the phonon dispersion of the ZrS₂, BiI₃ monolayers. The results are shown in Fig. 5.2 (a-b). We have not found any imaginary modes for ML-ZrS₂, whereas we have obtained slight phonon softening (smaller than

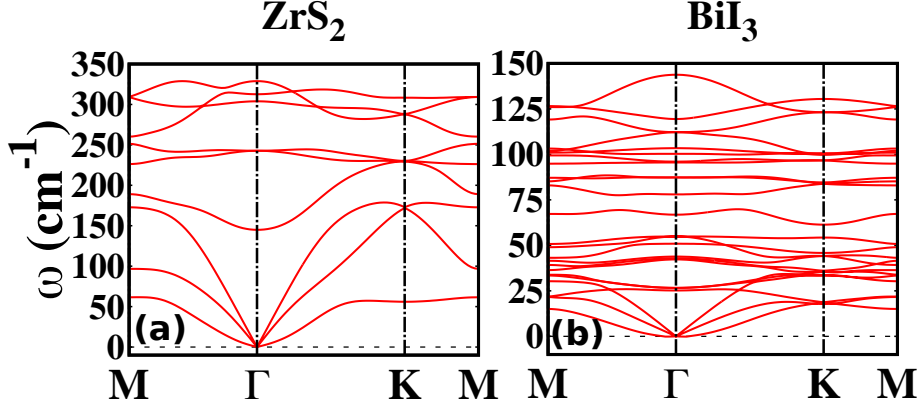


Figure 5.2: The phonon band structures (a) ML-ZrS₂ and (b) ML-BiI₃

0.2 cm⁻¹) near the zone center for ML-BiI₃, which could be due to numerical inaccuracy. Therefore, all the investigated systems are found to be dynamically stable at 0 K.

For ZrS₂, the phonon frequencies extend up to about 350 cm⁻¹ (Fig. 5.2(a)) while those for BiI₃, they extend till 150 cm⁻¹ (Fig. 5.2(b)). This suggests that the stiffness of the bonds is less in ML-BiI₃ than ML-ZrS₂, which is in accordance with the observed increase in cation-anion bond length in these systems. Additionally for ZrS₂, we do not observe mixing of the longitudinal and acoustic modes over the complete BZ.

5.3.2 Temperature dependent renormalization of the band structure.

Fig. 5.3 shows the DFT and renormalized band structures of these monolayers. For each case we observe an indirect band gap. While for ZrS₂ (Fig. 5.3(a)) the valence band maxima (VBM) and the conduction band minima (CBM) are at the Γ and M -points of the BZ, for BiI₃ (Fig. 5.3(b)) the VBM is along the $\Gamma \rightarrow K$ direction (closer to the Γ point). In addition to the DFT band structure, we have also plotted the renormalized band structure at 0K (Fig. 5.3(a)-(b)) and 300 K ((Fig. 5.3(c)-(d)). The 0K renormalized band structure corresponds to zero-point energy (ZPE) corrections to the band structure due to lattice vibrations. While the positions of the VBM and CBM in the BZ are unaffected by the band structure renormalization, we observe significant shifts in the renormalized energy eigenvalues with the VBM (CBM) moving up (down) in energy. This results in significant reduction in the band gaps. For example, in ZrS₂, the renormalized band gap is reduced from 1.16 eV to 0.51 eV at 0K. Similarly for BiI₃ we observe a band gap reduction of

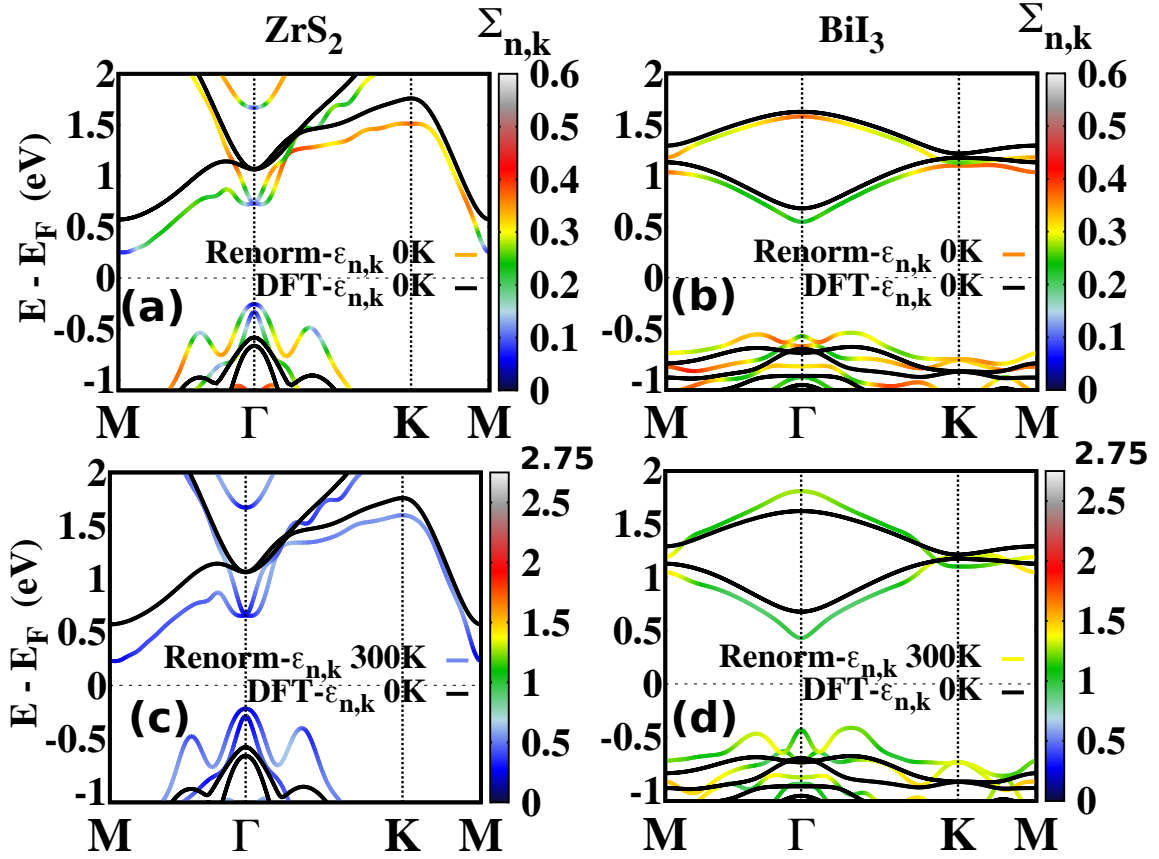


Figure 5.3: The DFT band structure (black) and the renormalized ones at 0K (colored lines) for (a) ML-ZrS₂, (b) ML-BiI₃ and at 300 K ((c) ML-ZrS₂, (d) ML-BiI₃). For the renormalized band structure, the magnitude of the imaginary part of electron-phonon self energy is also shown. For both the cases, the energy eigenvalues are shifted with respect to the Fermi energy. The Fermi energy is taken to be at the middle of the band gap.

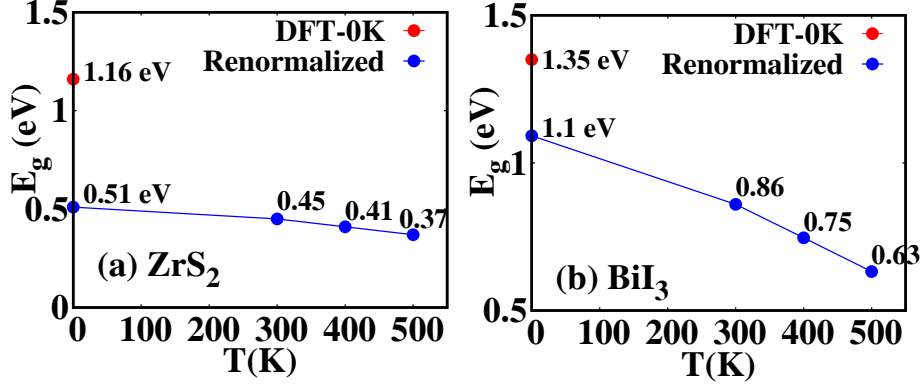


Figure 5.4: The variation of the renormalized band gap as a function of temperature for (a) ML-ZrS₂ (left panel) and (b) ML-BiI₃ (right panel).

about 0.25 eV. Fig. 5.4 shows the temperature dependence of the band gap. We find that as the temperature is increased, the band gap reduces further. However, the rate at which the reduction occurs is different in ZrS₂ compared to that observed in BiI₃. While for BiI₃ monolayer the band gap reduces by 0.47 eV as the temperature is increased from 0K to 500 K, in the case of ZrS₂ we observe a reduction of only 0.14 eV. This can be understood from the phonon frequencies. One observes significant softening of the phonon frequencies from ZrS₂ to BiI₃. As a result as the temperature is increased, it is easier to excite more phonon modes in BiI₃ compared to that in ZrS₂ resulting in larger changes in the temperature dependent band gap. A comparison of the changes in band gaps across these materials due to ZPE corrections and temperature renormalization shows that while the change in the band gap due to ZPE corrections does not show any trends as a function of ionicity, the rate at which the band gap reduces as a function of temperature increases with decrease in ionicity of the bonds.

In addition to the shifting of the band edges, we find that the band dispersion is also significantly altered due to renormalization. For both the cases we observe an enhancement of curvature compared to the DFT band structure. The curvature increases with an increase in temperature (Fig. 5.3(a)-(b) vs. Fig. 5.3(c)-(d)). To quantify the effect, we have computed the effective masses of the electrons and holes along certain high symmetry directions in these materials using the DFT band structure and the renormalized band structure. The same is listed in Table 5.1. We find that for these cases the effective masses of both holes and electrons are significantly reduced due to band structure renormalization.

Table 5.1: Comparison of effective masses of electrons and holes in the monolayers between the DFT-band structure and the renormalized band structure.

System	Carrier type	PBE band		Renormalized band structure @ 300K	
		m^* (zigzag) (m_e)	m^* (armchair) (m_e)	m^* (zigzag) (m_e)	m^* (armchair) (m_e)
ZrS ₂	electron	0.29	2.08	0.11	0.61
	hole	0.25	0.28	0.11	0.25
BiI ₃	electron	1.83	0.50	0.28	0.11
	hole	0.52	1.16	0.11	0.14

For the renormalized band structure, we have also plotted the $\text{Im} \sum_{nk}^{EP}$ in the colour scale. The inverse of $\text{Im} \sum_{nk}^{EP}$ is related to the life-time of carriers in that state. At 0K, we find that electron and hole pockets in ZrS₂ have similar and low values of $\text{Im} \sum_{nk}^{EP}$ (Fig. 5.3(a)) indicating a longer lifetime of the carriers. In contrast, $\text{Im} \sum_{nk}^{EP}$ at the electron and hole pockets in BiI₃ (Fig. 5.3(b)) have larger values compared to that observed in ZrS₂. Moreover, in BiI₃ $\text{Im} \sum_{nk}^{EP}$ for hole pockets are larger than that for electron pockets suggesting that electrons in BiI₃ will have a larger lifetime than holes. As the temperature is increased to 300 K, we observe significant changes in the electron lifetime, particularly for BiI₃ ((Fig. 5.3(c)-(d)).

5.3.3 Computation of τ .

5.3.3.1 τ from electron-phonon coupling.

The temperature dependency of the imaginary part of the electron-phonon self-energy ($\text{Im}\Sigma$) for the valence and conduction bands along high symmetry directions of the BZ is shown in Fig. 5.5. The values of $\text{Im} \sum_{nk}^{EP}$ for BiI₃ are larger than those observed for ZrS₂. Moreover, as expected, with rise in temperature the $\text{Im} \sum_{nk}^{EP}$ also increases suggesting enhanced scattering of electrons due to a larger number of excited phonons. Furthermore, by plotting the mode resolved $\text{Im} \sum_{nk}^{EP}$ (Fig. B.1 in the Appendix B) we find that for each system only one optical mode have a dominant contribution. These modes are shown in Fig. 5.5(c)-(d). For ZrS₂ (Fig. 5.5(c)), these modes correspond to compression and expansion of the monolayer along the direction normal to the plane of the monolayer. For BiI₃ the vibrational motion corresponds to a more complex motion that involves rumpling the BiI₃ sheet. This result clearly shows that computing τ by ignoring the contribution of the

optical modes, for this class of systems will clearly give erroneous results.

As mentioned in Section 5.2 the relaxation time of a carrier residing in a state labelled by n and k (τ_{nk}) is related to the inverse of $\text{Im} \sum_{nk}^{EP}$. Using the value of τ_{nk} we can compute the average value of the relaxation time for a given band n (τ_{av}^n), which is given by:

$$\tau_{av}^n = \sum_k \frac{\tau_{n,k} \epsilon_{n,k}}{\epsilon_{n,k}} \quad (5.4)$$

where the summation is over the complete BZ. The τ_{av} for the conduction (for electrons) and valence bands (for holes) of these systems as a function of temperature is shown in Fig. 5.5(e)-(f). We find that for both the valence and conduction bands τ_{av} decreases as one moves from ZrS₂ to BiI₃ suggesting that in these systems τ decreases as the ionicity of the material decreases. Additionally the difference of τ_{av} at a given temperature between the conduction and valence bands increase from ZrS₂ to BiI₃. Since τ has a complex dependence on the vibrational and electronic properties of a material and their coupling, it is difficult to exactly identify the cause of such a difference. However, based on Fig. 5.5 (a)-(b), one can conclude that the phonons couple with the conduction band and valence band electronic states differently in BiI₃ while in ZrS₂ both show similar coupling. As a consequence, one observes different values of τ for electrons and holes in BiI₃. For both the materials the average relaxation times also reduce with increase in temperature.

5.3.3.2 τ from deformation potential theory.

In this section we compute the average relaxation time for the electrons and holes in these materials from deformation potential theory. We note that the major difference between the two methods is that in the latter the contributions to τ_{av} from the optical phonon modes are neglected.

The values of C , E_{dp} and τ computed from deformation potential theory are given in Table 5.2. We note that the value of C is larger for ZrS₂ compared to that of BiI₃. The coupling strength between the electrons/holes and the acoustic phonons is indicated by $|E_{dp}|$. For both the systems, we find that $|E_{dp}|$ is larger for the holes than for the electrons suggesting that holes couple more strongly to acoustic phonons than electrons. The anisotropy in the transport properties is reflected in anisotropy of the effective masses of the charge

Table 5.2: C , E_{dp} and τ for the electrons and holes in ZrS₂ and BiI₃ monolayers.

System		C (eV/Å ²)	E_{dp} (eV)	τ (10 ⁻¹⁴ s)		
				$T = 300$ K	$T = 400$ K	$T = 500$ K
ZrS ₂	electron	5.34	-1.97	34.98	26.23	20.98
	hole		-7.38	7.06	5.30	4.24
BiI ₃	electron	1.40	-6.57	0.66	0.49	0.39
	hole		-7.38	0.64	0.48	0.39

carriers along the armchair and zigzag directions of the monolayer. Furthermore, the effective masses differ significantly depending on the system. Along the zigzag direction, m^* values for electrons and holes are larger in BiI₃ compared to that observed in ZrS₂. In contrast, along the armchair direction, the electron effective mass decreases from ZrS₂ to BiI₃.

The τ values for the electrons and holes in these monolayers, as a function of temperature, are shown in Fig. 5.6 and also listed in Table 5.2 for some temperatures. In both the materials, over the complete temperature range considered in this study, τ values for electrons are larger than those observed for holes. However, the magnitude by which the relaxation times differ varies from system to system. While for ZrS₂, the τ values for electrons are about two orders of magnitude larger than those observed for holes, for BiI₃ the difference is much smaller.

A comparison of τ computed using EPIs (Fig. 5.5) and deformation potential theory (Fig. 5.6) shows stark differences, not only quantitatively but also qualitatively. On the quantitative side, the values of τ computed using deformation potential theory are overestimated by about two orders of magnitude compared to those obtained from EPIs. Moreover, the qualitative picture is also different. For example, in ZrS₂, τ values computed using EPIs show that τ values for electrons are slightly larger than those for holes, while the difference is larger for BiI₃. In contrast, the difference in the relaxation time between holes and electrons obtained from deformation potential theory is larger for ZrS₂ than BiI₃. These differences can be understood from the fact that in the case of deformation potential theory we consider the coupling of the acoustic phonons only (which has negligible contributions), while in these systems the coupling with the optical phonons is much stronger as captured from the EPW calculations.

5.3.4 Transport properties

5.3.4.1 Transport properties with τ obtained from EPIs and DP theory.

In this section we explicitly show the effect of τ obtained using EPIs and DP theory on the transport properties of ZrS₂. Fig. 5.7 shows the transport properties (within the constant relaxation time approximation) as a function of carrier concentration computed using EPIs and DP theory. Since the Seebeck coefficient is independent of τ , for both the cases it remains unchanged (Fig. 5.7(a) and (d)). In contrast we find drastic changes in σ and power factor, Fig. 5.7(b), (c), (e) and (f), respectively. Due to orders of magnitude differences in the values of τ using the two theories, we observe orders of magnitude changes in the value of σ and power factor. We note that our results for the calculation of the transport properties using DP theory are in excellent agreement with those reported by Lv *et al.* [56], where they have obtained the results using DP theory. These results suggest that it is imperative to compute τ for these systems by explicitly considering the electron-phonon coupling.

5.3.4.2 Effect of CRTA and EPIs on transport properties.

In order to understand the effectiveness of the CRTA and the effect of the band structure renormalization on the transport properties, we have computed S , σ , power factor ($S^2\sigma$) and κ_e at room temperature for the monolayers. In each case, the transport coefficients have been computed in four different ways: (a) using DFT band structure and band gap within CRTA [DFT-BS (τ_{CRTA})], (b) using DFT band structure and band gap with τ_{nk} for each band [DFT-BS ($\tau_{\text{b-CRTA}}$)], (c) using DFT band structure and renormalized band gap within CRTA [EPW-gap+DFT-BS (τ_{CRTA})], (d) using renormalized band structure and band gap within CRTA [EPW-gap+EPW-BS (τ_{CRTA})]. For both the cases we have used the values of τ obtained from the EPW calculations. A comparison between (a) and (b) enables us to understand the effectiveness of the CRTA while that between (a) and (c) highlights the effect of the band gap on the transport properties. Comparing (c) and (d) will help us in understanding the importance and influence of the changes in the transport properties due to changes in the band structure because of the finite temperature effects. The results as a function of chemical potential (μ) at 300K are plotted in Fig. 5.8. Negative (positive) values of μ implies hole (electron) doping.

Going beyond the CRTA and using explicit values of τ yield values of S that are similar to those obtained within CRTA, at least for the range of chemical potential considered in this study (black and green dashed lines in Fig. 5.8(a)-(b)). However, for σ , we observe small changes as one goes beyond CRTA. For the systems considered in our study, we observe that the changes are more for electrons compared to holes. While at low hole doping concentration we do not observe significant changes in the values of σ obtained within CRTA and using explicit values of τ for each electronic state, at higher doping concentration small changes are observed in the magnitude of σ (black and green dashed lines for negative values of μ in Fig. 5.8(c)-(d)). In contrast, for electrons, there are differences in the values of σ obtained using the two methods. These differences increase with the increase in the doping concentration. Consistent with the changes in the values of S and σ , we observe small changes in the values of power factor (PF) as one goes beyond the constant relaxation time approximation (Fig. 5.8(e)-(f)). Similar to that observed in the case of conductivity, we note that the changes in PF for the electrons are larger than that observed for holes. Additionally, we have also studied the effect of the two methods on estimates of electronic contribution to thermal conductivity (κ_e) (Fig. 5.8(g)-(h)). We find that the changes in κ_e follow the changes in σ .

In contrast with the choice of τ , i.e. CRTA or beyond CRTA, used to compute S , the magnitude of the band gap significantly alters the values of Seebeck coefficient observed for these systems. As observed in Fig. 5.8(a)-(b) (black vs. red plots) we find that the maximum value of Seebeck coefficient is significantly reduced with the decrease in the band gap. In case of σ and PF, the band gap results in shift of the σ plots (black vs. red lines in Fig. 5.8(c)-(d), (e)-(f)). This implies that with the decrease in the band gap, it is possible to achieve the same value of conductivity and PF at smaller doping concentration.

A comparison of the red and blue plots in Fig. 5.8 highlights the effect of the band structure renormalization on the transport properties. The modified band structure slightly enhances the maximum value of Seebeck coefficient. For the Seebeck coefficient, the effect of the band structure renormalization is quite small because S being the ratio of the first and zeroth moments of the generalized transport coefficients, the effect due to the changes in the band structure is almost nullified. However, the effect is stronger for σ . In the monolayers considered in this study, the effect is stronger on the holes compared to that in electrons (Fig. 5.8(c)-(d)). While for the electrons the overall shape of the con-

ductivity plots is similar, for the holes we not only observe changes in their magnitude but also changes in their shape. For example, in ZrS_2 monolayer, σ computed with the renormalized band structure shows a peak at $\mu=-0.62$ eV which was not observed when computed with the DFT band structure. The large changes in the σ for the holes due to band structure renormalization are also reflected in the computed PF. Particularly, in ZrS_2 , the presence of a peak in σ at $\mu = -0.62$ eV results in a significant enhancement in the power factor. As observed in the previous cases, the changes in κ_e follow the changes in σ .

5.4 Summary

In conclusion, we have studied the effect of electron-phonon interactions on the transport properties of two ionic monolayers, namely, ZrS_2 and BiI_3 . Furthermore, we also evaluated the validity of the constant relaxation time approximation. EPI affects the transport properties in two ways: (a) the relaxation time of the carriers and (b) the renormalization of the band structure. Our calculations show that for ionic systems it is crucial to incorporate the effect of scattering of electrons by optical phonons because this is the dominant scattering channel for the carriers in these systems. Neglecting the contributions of the scattering of charge carriers by optical phonons results in overestimation of relaxation times by two orders of magnitude. Comparison of the computed values of τ obtained within CRTA and beyond CRTA shows that for heavy doping it might be important to go beyond CRTA to make reasonable estimates of the transport coefficients. Additionally, our results also show that in these systems, since the EPI results in significant changes in the band gap and the band structure, it is important to consider these effects in order to predict or understand the transport properties of ionic solids. For these materials we find that the band gap decreases faster with temperature as the ionicity decreases. Moreover, the relaxation time due to electron-phonon scattering also reduces as the ionicity decreases. We hope that our results will motivate further investigations on other low-dimensional ionic materials.

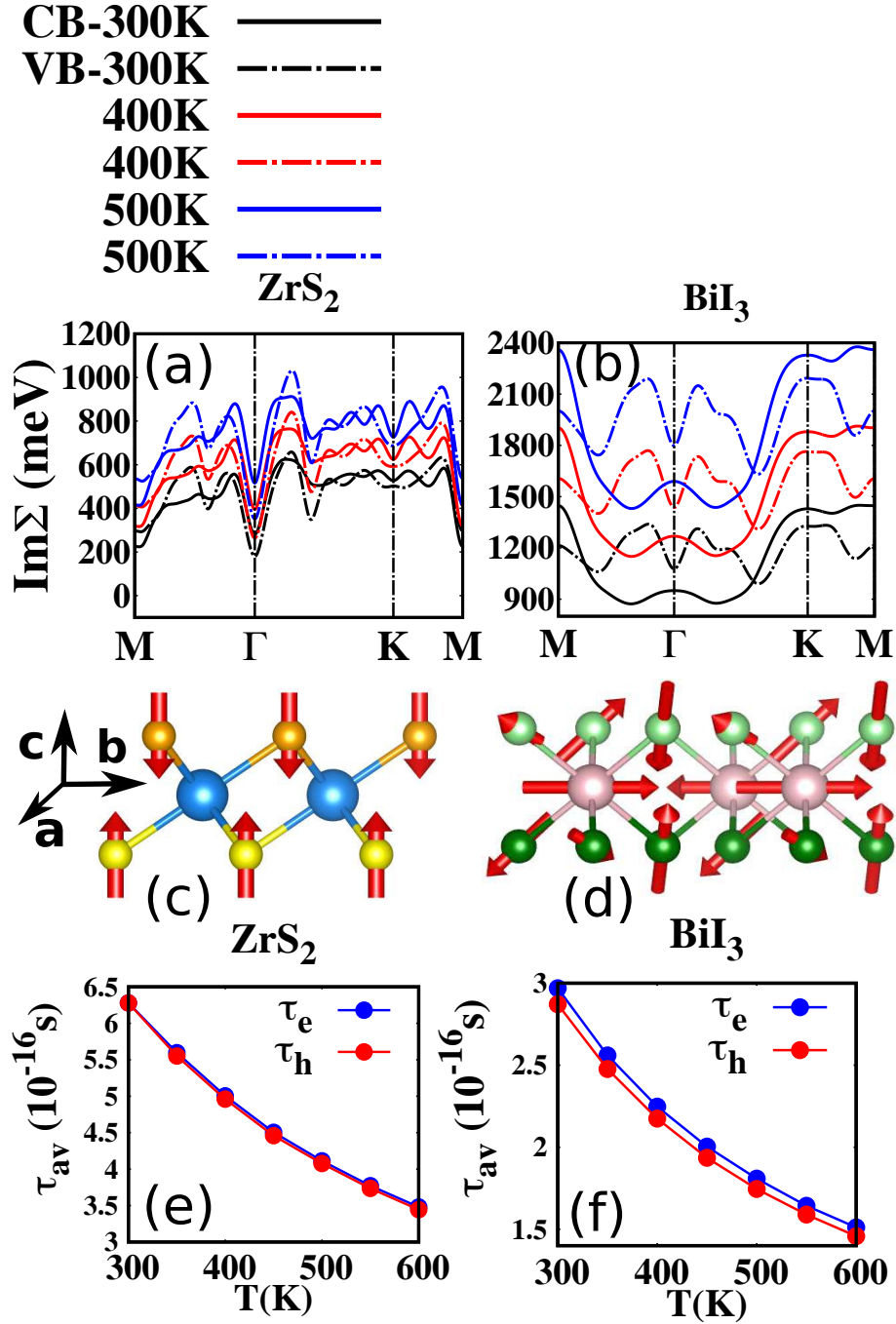


Figure 5.5: The imaginary part of the electron self-energy for the conduction (solid lines) and valence band (dashed lines) for ML-ZrS₂ (a) and ML-BiI₃ (b) at 300 K (black), 400 K (red) and 500 K (blue). The vibrational patterns of optical modes at Γ point which have the largest contribution to $\text{Im}\Sigma_{n,k}$ are shown for ML-ZrS₂ and ML-BiI₃ in (c-d). The average relaxation times for electrons (blue) and holes (red) as a function of temperature for the ML-ZrS₂ (e) and ML-BiI₃ (f) are also shown.

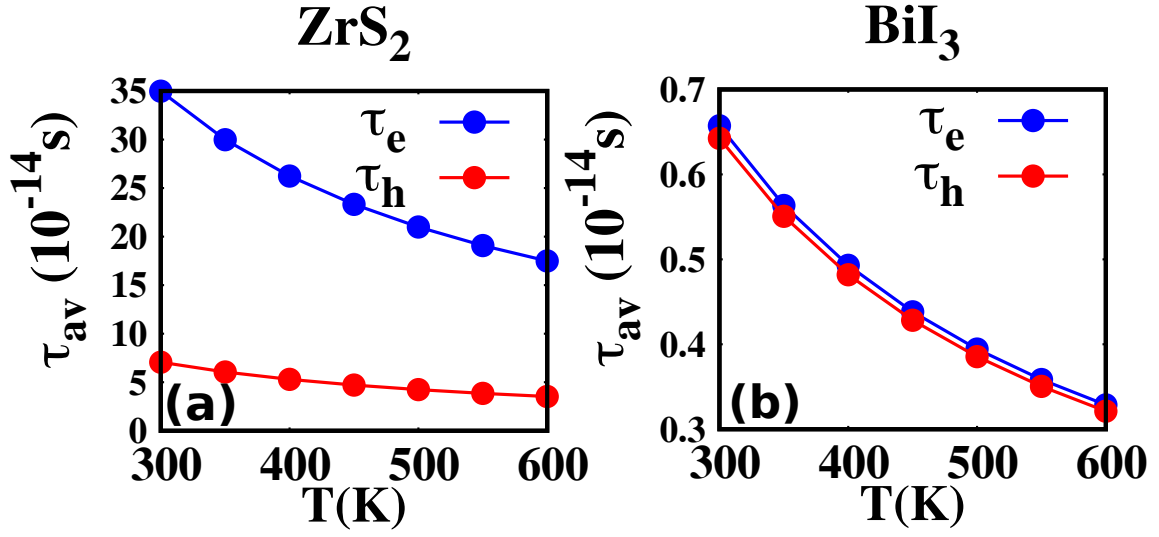


Figure 5.6: The average relaxation time estimated using deformation potential theory for electrons (blue) and holes (red) as a function of temperature for (a) ZrS_2 and (b) BiI_3 monolayers.

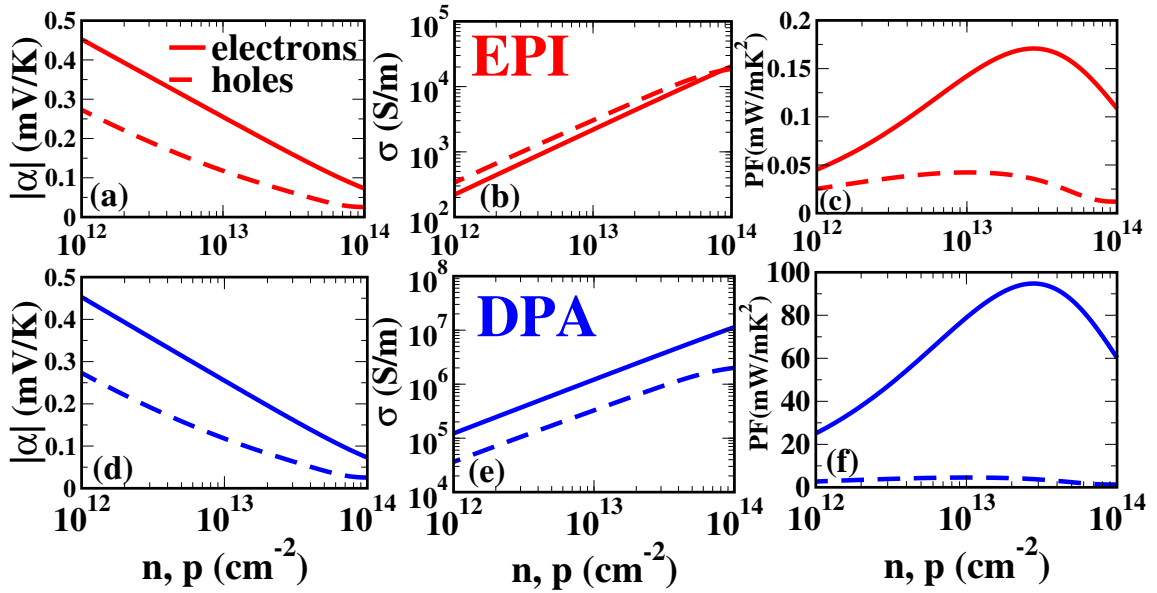


Figure 5.7: Comparison of the transport properties for n-type (solid lines) and p-type (dashed lines) doping of ML- ZrS_2 at 300 K, where τ for the charge carriers is obtained using EPIs (top panel) and deformation potential approximation (bottom panel).

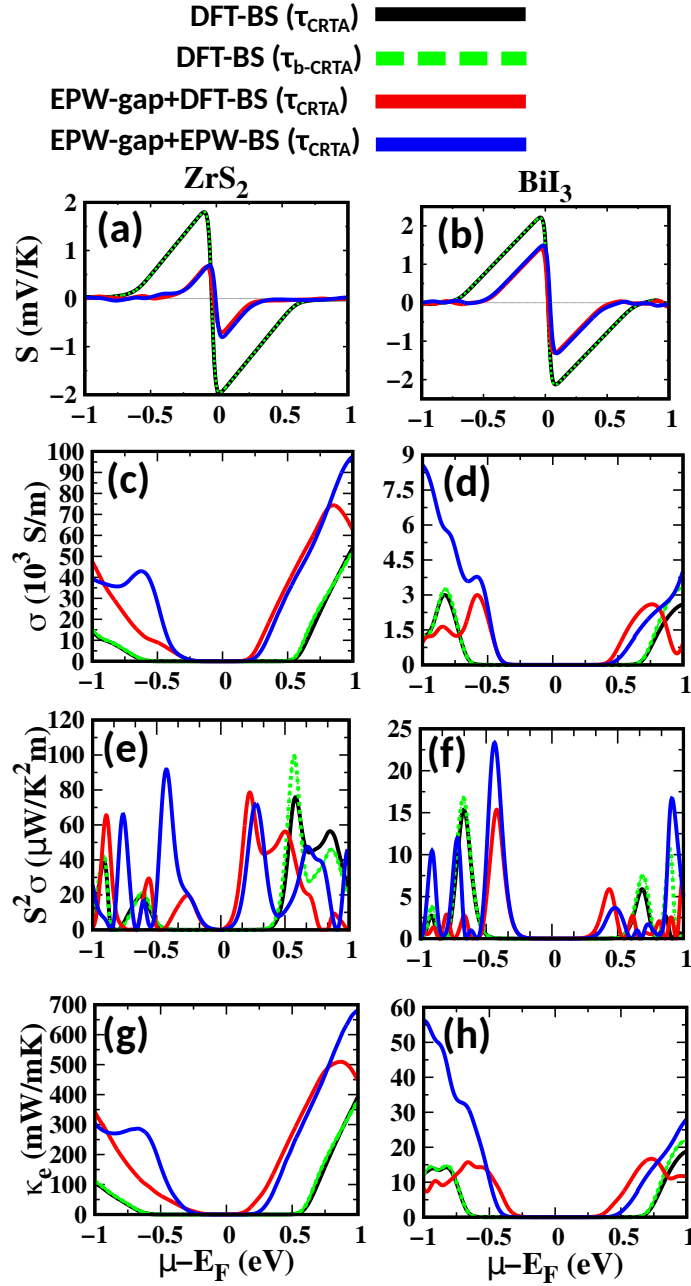


Figure 5.8: The transport properties as a function of chemical potential (μ) based on DFT-BS and CRTA [DFT-BS (τ_{CRTA})] (black solid lines), DFT-BS and with explicit values of τ_{nk} for each state [DFT-BS (τ_{b-CRTA})] (green dashed lines), DFT-BS and renormalized band gap within CRTA [EPW-gap+DFT-BS (τ_{CRTA})] (red solid line) and renormalized band structure and band gap within CRTA [EPW-gap+EPW-BS (τ_{CRTA})] (blue). The top, second, third and bottom panels show plots of α , σ , power factor ($S^2\sigma$) and κ_e , respectively. The left and right panels are for ZrS_2 , BiI_3 respectively.

Appendix A

A.1 Computational details

We have used a q -mesh of $(1 \times 1 \times 1)$ to sample the Fock operator in Gaussian attenuated Perdew-Burke-Ernerhof (Gau-PBE) hybrid functional calculations for all the configurations. [109]

A.2 Determination of U

In order to choose an appropriate value of U, we first computed the band gap for bulk BaCu_2Se_2 varying U from 4 eV to 12 eV and with Gau-PBE hybrid functional. We observed that while for PBE the computed band gap is 0.69 eV, for U=4 to 12 eV the band gaps varied from 0.96 eV to 1.23 eV. These values are significantly lower than the experimental value of 1.80 eV and that of 1.85 eV, computed with Gau-PBE. Since the value of U is already quite large and the band gap does not increase significantly (tripling U resulted in an increase in the band gap by 0.27 eV), we decided to choose the value of U that results in similar hybridization of Cu-3d and Se-4p as observed in the Gau-PBE calculations. We chose hybridization as a criterion because while band gap affects the transport properties primarily through change of carrier concentration, the hybridization will affect the band dispersion and thereby result even in qualitative changes of the transport properties.

In order to choose the appropriate value of U, we computed the DOS of the Al-doped system with U = 4 eV and 12 eV and compared them with the more accurate Gau-PBE

hybrid functionals. The density of states projected on the atomic orbitals of Ba, Cu and Se atoms in Al-doped BaCu_2Se_2 computed using Gau-PBE hybrid functionals and PBE+U with two different values of U parameter (Fig. A.1 (a-c)). Gau-PBE calculations show that the valence band is comprised of electronic states of Se-4p and Cu-3d orbitals whereas the conduction band is composed of Ba-5d orbitals. These features are preserved in PBE+U calculations with U=4 eV. However, with U=12 eV, we observe a splitting between the electronic states of Cu-3d and Se-4p. Cu-3d states are shifted downwards with larger U value. Therefore, we have performed all the electronic and transport calculations with PBE+U (4 eV) that are inexpensive computationally relative to Gau-PBE calculations. Similar features are observed for Ga, In and Tl-doped configurations.

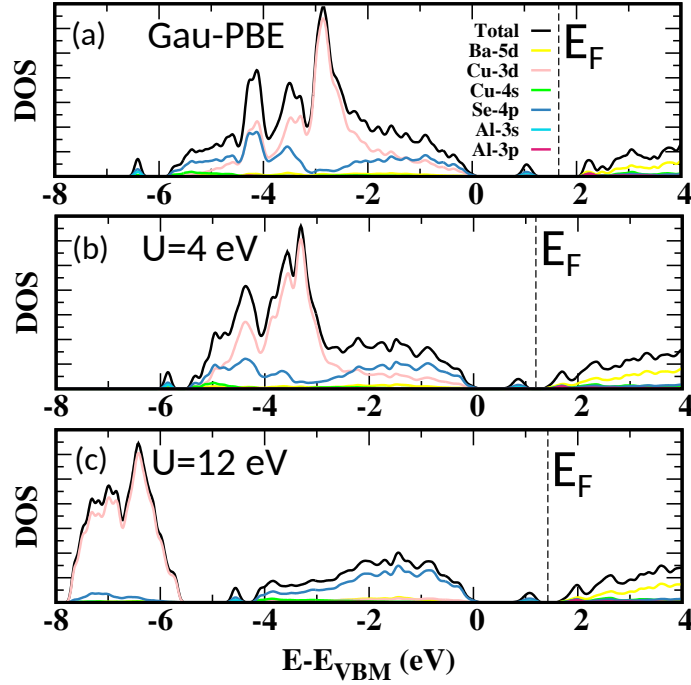


Figure A.1: The projected DOS of Al-doped BaCu_2Se_2 computed at the level of (a) Gau-PBE (b) PBE+U (4 eV) and (c) PBE+U (12 eV). The dopant atom occupies Cu_1 -site. The VBM is set to zero in all the cases.

A.3 Effect of doping BaCu_2Se_2

Fig. A.2 (a) and (b) show the T_1 and T_2 tetrahedra when Al is doped on Cu_1 and Cu_2 -sites respectively. The corresponding projected projected DOS of nearest neighbouring atoms and the dopant are shown in Fig. A.2 (c-d). Table A.1 shows the bond distances

of dopant atoms with neighbouring Se atoms in doped configurations and corresponding bond distances in pristine system. We notice that bond distances increase while going to Al to Tl in all the doped configurations due to increase in atomic size of dopant while moving down the group.

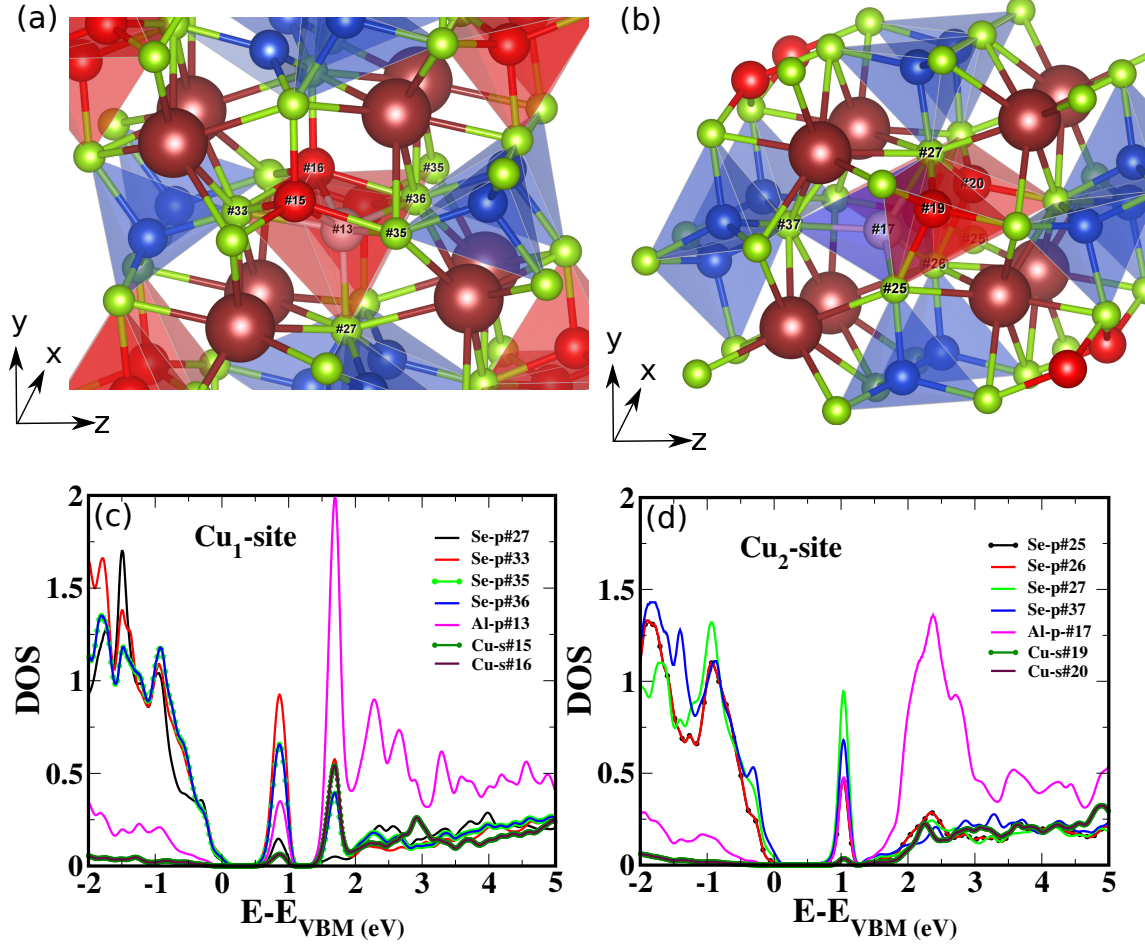


Figure A.2: Al doped on Cu-site in (a) T₁ and (b) T₂ tetrahedron. T₁ and T₂ tetrahedra are represented by red and blue color respectively. The projected DOS of Al-doped BaCu₂Se₂ computed at the level of PBE+U when Al occupies (c) Cu₁ and (d) Cu₂-site. The VBM is set to zero in all the cases.

Table A.1: Bond distances in the tetrahedra T_1 and T_2 for pristine and doped configurations. All the distances are in Å.

Pristine		Dopants on Cu_1 -site			
Cu_1 -Se	Al-Se	Ga-Se	In-Se	Tl-Se	
2.59	2.78	2.83	2.97	3.00	
2.59	2.78	2.83	2.97	3.00	
2.54	2.61	2.74	2.83	2.88	
2.54	2.74	2.76	2.91	3.00	
Pristine		Dopants on Cu_2 -site			
Cu_2 -Se	Al-Se	Ga-Se	In-Se	Tl-Se	
2.50	2.64	2.74	2.83	2.89	
2.50	2.64	2.74	2.83	2.89	
2.52	2.67	2.78	2.96	2.97	
2.62	2.79	2.85	3.00	3.00	

Appendix B

Table B.1: Pauling electronegativity (EN) values for the different elements present in the monolayers [3]. Difference between the electronegativity (ΔEN) of the elements present in the monolayers.

Element	EN
Zr	1.33
Bi	2.02
I	2.66
S	2.58
System	ΔEN
ZrS ₂	1.25
BiI ₃	0.64

B.1 Mode-resolved imaginary part of electron-phonon self-energy

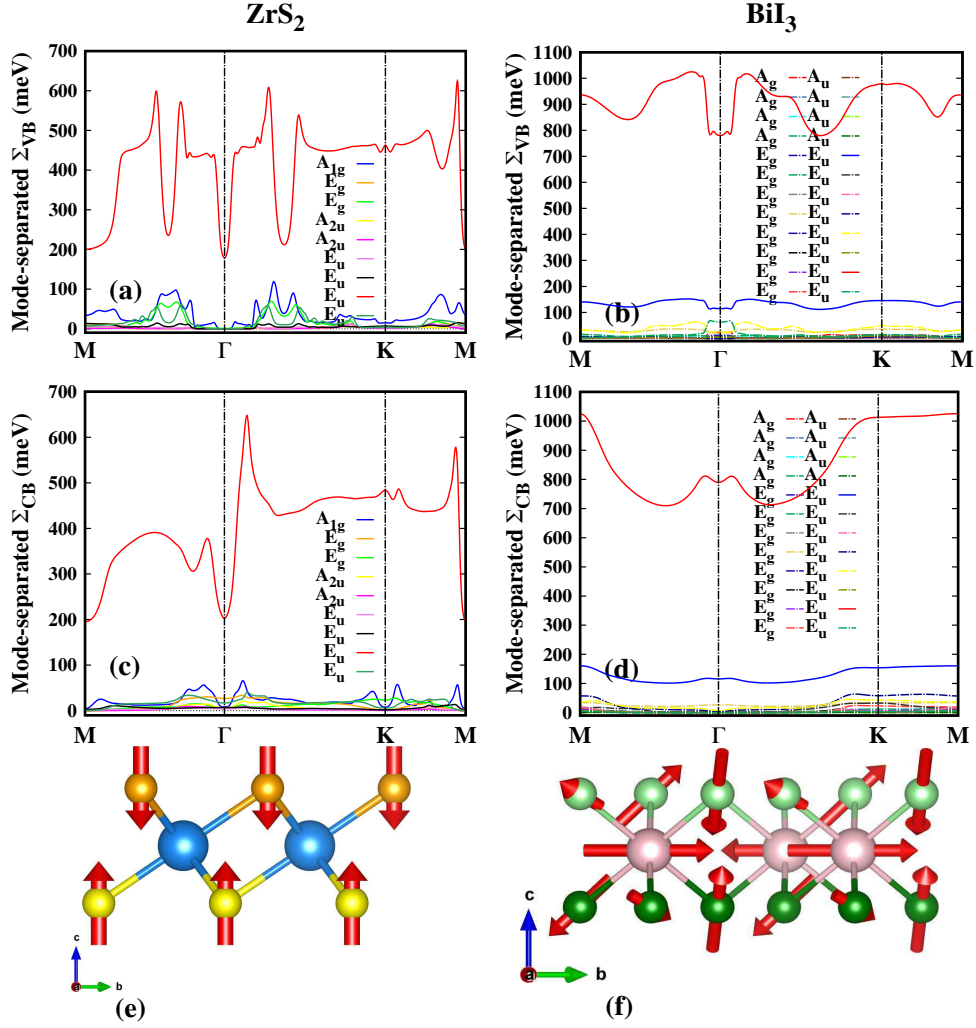


Figure B.1: The mode resolved imaginary part of electron-phonon self energy for the valence (top panels (a-b)) and conduction (middle panels (c-d)) bands for the ML-ZrS₂ and ML-BiI₃ at 300 K, where contribution from various modes are shown by different colors. The largest contribution to $\text{Im}\Sigma_{n,k}$ due to optical modes is shown by red curves in each case. The vibrational patterns of optical modes at Γ point with dominant contribution to $\text{Im}\Sigma_{n,k}$ are shown for ML-ZrS₂ and ML-BiI₃ in (e-f).

Bibliography

- [1] M. C. Payne, M. P. Teter, D. C. Allan, T. A. Arias, and J. D. Joannopoulos, Iterative minimization techniques for ab initio total-energy calculations: molecular dynamics and conjugate gradients, *Rev. Mod. Phys.* **64**, pp. 1045–1097 (1992). [xii](#), [23](#), [24](#)
- [2] Grimme Stefan, Semiempirical GGA-type density functional constructed with a long-range dispersion correction, *Journal of Computational Chemistry* **27**(15), pp. 1787–1799 (2006). [xvii](#), [49](#), [50](#), [66](#)
- [3] R. L. Keiter J. E. Huheey, E. A. Keiter and O. K. Medhi, *Inorganic Chemistry*, Pearson Education India 4 edition (2006). [xvii](#), [86](#)
- [4] Marta Rull-Bravo, Alberto Moure, JF Fernández, and Marisol Martín-González, Skutterudites as thermoelectric materials: revisited, *Rsc Advances* **5**(52), pp. 41653–41667 (2015). [3](#)
- [5] GS Nolas, M Kaeser, RT Littleton IV, and TM Tritt, High figure of merit in partially filled ytterbium skutterudite materials, *Applied Physics Letters* **77**(12), pp. 1855–1857 (2000). [4](#)
- [6] G Rogl and P Rogl, Skutterudites, a most promising group of thermoelectric materials, *Current opinion in green and sustainable chemistry* **4**, pp. 50–57 (2017). [4](#)
- [7] Chao Han, Zhen Li, and Shixue Dou, Recent progress in thermoelectric materials, *Chinese Science Bulletin* **59**, pp. 2073–2091 (2014). [4](#), [5](#), [6](#), [8](#)
- [8] Xun Shi, Jiong Yang, James R. Salvador, Miaofang Chi, Jung Y. Cho, Hsin Wang, Shengqiang Bai, Jihui Yang, Wenqing Zhang, and Lidong Chen, Multiple-Filled

Skutterudites: High Thermoelectric Figure of Merit through Separately Optimizing Electrical and Thermal Transports, *Journal of the American Chemical Society* **133**(20), pp. 7837–7846 (2011), PMID: 21524125. [4](#)

- [9] Zhi-Yuan Liu, Jiang-Long Zhu, Xin Tong, Shuo Niu, and Wen-Yu Zhao, A review of CoSb₃-based skutterudite thermoelectric materials, *Journal of Advanced Ceramics* **9**(6), pp. 647–673 (2020). [4](#)
- [10] Mogens Christensen, Simon Johnsen, and Bo Brummerstedt Iversen, Thermoelectric clathrates of type I, *Dalton transactions* **39**(4), pp. 978–992 (2010). [4](#), [5](#)
- [11] Marion C Schäfer and Svilen Bobev, Tin clathrates with the type II structure, *Journal of the American Chemical Society* **135**(5), pp. 1696–1699 (2013). [4](#)
- [12] GS Nolas, JL Cohn, M Kaeser, and TM Tritt, Thermal Conductivity of type I and II Clathrate Compounds, *MRS Online Proceedings Library (OPL)* **626** (2000). [4](#)
- [13] A. Saramat, G. Svensson, A. E. C. Palmqvist, C. Stiewe, E. Mueller, D. Platzek, S. G. K. Williams, D. M. Rowe, J. D. Bryan, and G. D. Stucky, Large thermoelectric figure of merit at high temperature in Czochralski-grown clathrate Ba₈Ga₁₆Ge₃₀, *Journal of Applied Physics* **99**(2), pp. 023708 (2006). [4](#), [5](#)
- [14] Juli-Anna Dolyniuk, Bryan Owens-Baird, Jian Wang, Julia V Zaikina, and Kirill Kovnir, Clathrate thermoelectrics, *Materials Science and Engineering: R: Reports* **108**, pp. 1–46 (2016). [5](#)
- [15] Abanti Nag and V. Shubha, Oxide Thermoelectric Materials: A Structure-Property Relationship, *Journal of Electronic Materials* **43**, pp. 962–977 (2014). [5](#)
- [16] I. Terasaki, Y. Sasago, and K. Uchinokura, Large thermoelectric power in NaCo₂O₄ single crystals, *Phys. Rev. B* **56**, pp. R12685–R12687 (1997). [5](#)
- [17] Masahiro Shikano and Ryoji Funahashi, Electrical and thermal properties of single-crystalline (Ca₂CoO₃)_{0.7}CoO₂ with a Ca₃Co₄O₉ structure, *Applied physics letters* **82**(12), pp. 1851–1853 (2003). [5](#)
- [18] Ryoji Funahashi and Masahiro Shikano, Bi₂Sr₂Co₂O_y whiskers with high thermoelectric figure of merit, *Applied physics letters* **81**(8), pp. 1459–1461 (2002). [5](#)

- [19] Kenjiro Fujita, Tadashi Mochida, and Kazuo Nakamura, High-temperature thermoelectric properties of $\text{Na}_x\text{CoO}_{2-\delta}$ single crystals, *Japanese Journal of Applied Physics* **40**(7R), pp. 4644 (2001). [5](#)
- [20] L. D. Hicks and M. S. Dresselhaus, Effect of quantum-well structures on the thermoelectric figure of merit, *Phys. Rev. B* **47**, pp. 12727–12731 (1993). [5](#), [11](#), [47](#), [65](#)
- [21] L. D. Hicks and M. S. Dresselhaus, Thermoelectric figure of merit of a one-dimensional conductor, *Phys. Rev. B* **47**, pp. 16631–16634 (1993). [5](#), [11](#), [47](#), [65](#)
- [22] Hiromichi Ohta, SungWng Kim, Yoriko Mune, Teruyasu Mizoguchi, Kenji Nomura, Shingo Ohta, Takashi Nomura, Yuki Nakanishi, Yuichi Ikuhara, Masahiro Hirano, Hideo Hosono, and Kunihiro Koumoto, Giant thermoelectric Seebeck coefficient of a two-dimensional electron gas in SrTiO_3 , *Nature Materials* **6**, pp. 129–134 (2007). [5](#)
- [23] Jian He, Yufei Liu, and Ryoji Funahashi, Oxide thermoelectrics: The challenges, progress, and outlook, *Journal of Materials Research* **26**(15), pp. 1762–1772 (2011). [5](#)
- [24] Yining Feng, Xiaodong Jiang, Ehsan Ghafari, Bahadir Kucukgok, Chaoyi Zhang, Ian Ferguson, and Na Lu, Metal oxides for thermoelectric power generation and beyond, *Advanced Composites and Hybrid Materials* **1**(1), pp. 114–126 (2018). [5](#)
- [25] Rishi Prasad and Shekhar D Bhame, Review on texturization effects in thermoelectric oxides, *Materials for Renewable and Sustainable Energy* **9**(1), pp. 1–22 (2020). [5](#)
- [26] Yinong Yin, Bharati Tudu, and Ashutosh Tiwari, Recent advances in oxide thermoelectric materials and modules, *Vacuum* **146**, pp. 356–374 (2017). [5](#)
- [27] Jiong Yang, Huanming Li, Ting Wu, Wenqing Zhang, Lidong Chen, and Jihui Yang, Evaluation of half-Heusler compounds as thermoelectric materials based on the calculated electrical transport properties, *Advanced Functional Materials* **18**(19), pp. 2880–2888 (2008). [5](#)

- [28] T Fang, K Xia, P Nan, B Ge, X Zhao, and T Zhu, A new defective 19-electron TiPtSb half-Heusler thermoelectric compound with heavy band and low lattice thermal conductivity, *Materials Today Physics* **13**, pp. 100200 (2020). [5](#)
- [29] Hossein Asghar Rahnamaye Aliabad, Zahra Nodehi, Behrooz Maleki, and Azam Abareshi, Electronical and thermoelectric properties of half-Heusler ZrNiPb under pressure in bulk and nanosheet structures for energy conversion, *Rare Metals* **38**(11), pp. 1015–1023 (2019). [5](#)
- [30] Wuyang Ren, Hangtian Zhu, Qing Zhu, Udara Saparamadu, Ran He, Zihang Liu, Jun Mao, Chao Wang, Kornelius Nielsch, Zhiming Wang, et al., Ultrahigh power factor in thermoelectric system $\text{Nb}_{0.95}\text{M}_{0.05}\text{FeSb}$ (M = Hf, Zr, and Ti), *Advanced Science* **5**(7), pp. 1800278 (2018). [5](#)
- [31] Ran He, Daniel Kraemer, Jun Mao, Lingping Zeng, Qing Jie, Yucheng Lan, Chunhua Li, Jing Shuai, Hee Seok Kim, Yuan Liu, et al., Achieving high power factor and output power density in p-type half-Heuslers $\text{Nb}_{1-x}\text{Ti}_x\text{FeSb}$, *Proceedings of the National Academy of Sciences* **113**(48), pp. 13576–13581 (2016). [5](#)
- [32] Chenguang Fu, Tiejun Zhu, Yintu Liu, Hanhui Xie, and Xinbing Zhao, Band engineering of high performance p-type FeNbSb based half-Heusler thermoelectric materials for figure of merit $zT > 1$, *Energy & Environmental Science* **8**(1), pp. 216–220 (2015). [5](#), [6](#)
- [33] S. Joseph Poon, Recent Advances in Thermoelectric Performance of Half-Heusler Compounds, *Metals* **8**(12) (2018). [6](#)
- [34] Hangtian Zhu, Jun Mao, Yuwei Li, Jifeng Sun, Yumei Wang, Qing Zhu, Guannan Li, Qichen Song, Jiawei Zhou, Yuhao Fu, et al., Discovery of TaFeSb-based half-Heuslers with high thermoelectric performance, *Nature communications* **10**(1), pp. 1–8 (2019). [6](#)
- [35] Kaiyang Xia, Yintu Liu, Shashwat Anand, G Jeffrey Snyder, Jiazhan Xin, Junjie Yu, Xinbing Zhao, and Tiejun Zhu, Enhanced Thermoelectric Performance in 18-Electron $\text{Nb}_{0.8}\text{CoSb}$ Half-Heusler Compound with Intrinsic Nb Vacancies, *Advanced Functional Materials* **28**(9), pp. 1705845 (2018). [6](#)
- [36] Junjie Yu, Yunfei Xing, Chaoliang Hu, Zhijie Huang, Qinyi Qiu, Chao Wang, Kaiyang Xia, Zhenyi Wang, Shengqiang Bai, Xinbing Zhao, et al., Half-heusler

- thermoelectric module with high conversion efficiency and high power density, *Advanced Energy Materials* **10**(25), pp. 2000888 (2020). [6](#)
- [37] Wenjie Xie, Anke Weidenkaff, Xinfeng Tang, Qingjie Zhang, Joseph Poon, and Terry M. Tritt, Recent advances in nanostructured thermoelectric half-Heusler compounds, *Nanomaterials* **2**(4), pp. 379–412 (2012). [6](#)
- [38] Shuo Chen and Zhifeng Ren, Recent progress of half-Heusler for moderate temperature thermoelectric applications, *Materials today* **16**(10), pp. 387–395 (2013). [6](#)
- [39] Lihong Huang, Qinyong Zhang, Bo Yuan, Xiang Lai, Xiao Yan, and Zhifeng Ren, Recent progress in half-Heusler thermoelectric materials, *Materials Research Bulletin* **76**, pp. 107–112 (2016). [6](#)
- [40] Tiejun Zhu, Chenguang Fu, Hanhui Xie, Yintu Liu, and Xinbing Zhao, High efficiency half-Heusler thermoelectric materials for energy harvesting, *Advanced Energy Materials* **5**(19), pp. 1500588 (2015). [6](#)
- [41] Jan-Willem G Bos and Ruth A Downie, Half-Heusler thermoelectrics: a complex class of materials, *Journal of Physics: Condensed Matter* **26**(43), pp. 433201 (2014). [6](#)
- [42] Chao Han, Qiao Sun, Zhen Li, and Shi Xue Dou, Thermoelectric Enhancement of Different Kinds of Metal Chalcogenides, *Advanced Energy Materials* **6**(15), pp. 1600498 (2016). [6](#), [7](#), [8](#)
- [43] Aaron D. LaLonde, Yanzhong Pei, and G. Jeffrey Snyder, Reevaluation of $\text{PbTe}_{1-x}\text{I}_x$ as high performance n-type thermoelectric material, *Energy Environ. Sci.* **4**, pp. 2090–2096 (2011). [6](#)
- [44] Yanzhong Pei, Aaron LaLonde, Shiho Iwanaga, and G. Jeffrey Snyder, High thermoelectric figure of merit in heavy hole dominated PbTe , *Energy Environ. Sci.* **4**, pp. 2085–2089 (2011). [6](#)
- [45] Kanishka Biswas, Jiaqing He, Ivan D. Blum, Chun-I Wu, Timothy P. Hogan, David N. Seidman, Vinayak P. Dravid, and Mercouri G. Kanatzidis, High-performance bulk thermoelectrics with all-scale hierarchical architectures, *Nature* **489**(7416), pp. 414–418 (2012). [6](#)

- [46] Terry M. Tritt and M. A. Subramanian, Thermoelectric Materials, Phenomena, and Applications: A Bird's Eye View, *MRS Bulletin* **31**(3), pp. 188198 (2006). 7
- [47] Zhenglong Tang, Lipeng Hu, Tiejun Zhu, Xiaohua Liu, and Xinbing Zhao, High performance n-type bismuth telluride based alloys for mid-temperature power generation, *J. Mater. Chem. C* **3**, pp. 10597–10603 (2015). 7
- [48] Sang Il Kim, Kyu Hyoung Lee, Hyeon A Mun, Hyun Sik Kim, Sung Woo Hwang, Jong Wook Roh, Dae Jin Yang, Weon Ho Shin, Xiang Shu Li, Young Hee Lee, G. Jeffrey Snyder, and Sung Wng Kim, Dense dislocation arrays embedded in grain boundaries for high-performance bulk thermoelectrics, *Science* **348**(6230), pp. 109–114 (2015). 7
- [49] Rama Venkatasubramanian, Edward Siivola, Thomas Colpitts, and Brooks O'Quinn, Thin-film thermoelectric devices with high room-temperature figures of merit, *Nature* **413**(6856), pp. 597–602 (2001). 7
- [50] Huili Liu, Xun Shi, Fangfang Xu, Linlin Zhang, Wenqing Zhang, Lidong Chen, Qiang Li, Ctirad Uher, Tristan Day, and G. Jeffrey Snyder, Copper ion liquid-like thermoelectrics, *Nature Materials* **11**(5), pp. 422–425 (2012). 7
- [51] Huili Liu, Xun Yuan, Ping Lu, Xun Shi, Fangfang Xu, Ying He, Yunshan Tang, Shengqiang Bai, Wenqing Zhang, Lidong Chen, Yue Lin, Lei Shi, He Lin, Xingyu Gao, Xingmin Zhang, Hang Chi, and Ctirad Uher, Ultrahigh Thermoelectric Performance by Electron and Phonon Critical Scattering in $\text{Cu}_2\text{Se}_{1-x}\text{I}_x$, *Advanced Materials* **25**(45), pp. 6607–6612 (2013). 7
- [52] Michihiro Ohta, Shuhei Satoh, Toshihiro Kuzuya, Shinji Hirai, Masaru Kunii, and Atsushi Yamamoto, Thermoelectric properties of $\text{Ti}_{1+x}\text{S}_2$ prepared by CS_2 sulfuration, *Acta Materialia* **60**(20), pp. 7232–7240 (2012). 8
- [53] E. Guilmeau, T. Barbier, A. Maignan, and D. Chateigner, Thermoelectric anisotropy and texture of intercalated TiS_2 , *Applied Physics Letters* **111**(13), pp. 133903 (2017). 8
- [54] S. Kumar and U. Schwingenschlöggl, Thermoelectric Response of Bulk and Monolayer MoSe_2 and WSe_2 , *Chemistry of Materials* **27**(4), pp. 1278–1284 (2015). 8

- [55] Swastibrata Bhattacharyya, Tribhuvan Pandey, and Abhishek K Singh, Effect of strain on electronic and thermoelectric properties of few layers to bulk MoS₂, *Nanotechnology* **25**(46), pp. 465701 (2014). [8](#)
- [56] H. Y. Lv, W. J. Lu, D. F. Shao, H. Y. Lu, and Y. P. Sun, Strain-induced enhancement in the thermoelectric performance of a ZrS₂ monolayer, *J. Mater. Chem. C* **4**, pp. 4538–4545 (2016). [8](#), [47](#), [48](#), [51](#), [55](#), [57](#), [65](#), [66](#), [69](#), [76](#)
- [57] Patrick R. N. Misse, David Berthebaud, Oleg I. Lebedev, Antoine Maignan, and Emmanuel Guilmeau, Synthesis and Thermoelectric Properties in the 2D Ti_{1-x}Nb_xS₃ Trichalcogenides, *Materials* **8**(5), pp. 2514–2522 (2015). [8](#)
- [58] Jing Li, Li-Dong Zhao, Jiehe Sui, David Berardan, Wei Cai, and Nita Dragoe, BaCu₂Se₂ based compounds as promising thermoelectric materials, *Dalton Trans.* **44**, pp. 2285–2293 (2015). [8](#), [37](#)
- [59] Priyanka Jood and Michihiro Ohta, Hierarchical Architecturing for Layered Thermoelectric Sulfides and Chalcogenides, *Materials* **8**(3), pp. 1124–1149 (2015). [8](#)
- [60] Junyi Liu, Qiang Sun, Yoshiyuki Kawazoe, and Puru Jena, Exfoliating biocompatible ferromagnetic Cr-trihalide monolayers, *Phys. Chem. Chem. Phys.* **18**, pp. 8777–8784 (2016). [8](#), [48](#)
- [61] Chengxi Huang, Jian Zhou, Haiping Wu, Kaiming Deng, Puru Jena, and Erjun Kan, Quantum anomalous Hall effect in ferromagnetic transition metal halides, *Phys. Rev. B* **95**, pp. 045113 (2017). [8](#), [48](#)
- [62] Junjie He, Shuangying Ma, Pengbo Lyu, and Petr Nachtigall, Unusual Dirac half-metallicity with intrinsic ferromagnetism in vanadium trihalide monolayers, *J. Mater. Chem. C* **4**, pp. 2518–2526 (2016). [8](#), [48](#)
- [63] Wei-Bing Zhang, Long-Jun Xiang, and Hai-Bin Li, Theoretical perspective of energy harvesting properties of atomically thin BiI₃, *J. Mater. Chem. A* **4**, pp. 19086–19094 (2016). [8](#), [48](#), [49](#), [51](#), [55](#), [57](#), [66](#), [69](#)
- [64] Pan Liu, Feng Lu, Maokun Wu, Xiaoguang Luo, Yahui Cheng, Xue-Wei Wang, Weichao Wang, Wei-Hua Wang, Hui Liu, and Kyeongjae Cho, Electronic structures and band alignments of monolayer metal trihalide semiconductors MX₃, *J. Mater. Chem. C* **5**, pp. 9066–9071 (2017). [8](#), [48](#)

- [65] Darshana Wickramaratne, Ferdows Zahid, and Roger K. Lake, Electronic and thermoelectric properties of van der Waals materials with ring-shaped valence bands, *Journal of Applied Physics* **118**(7), pp. 075101 (2015). [8](#), [48](#)
- [66] Prashun Gorai, Eric S. Toberer, and Vladan Stevanovi, Computational identification of promising thermoelectric materials among known quasi-2D binary compounds, *J. Mater. Chem. A* **4**, pp. 11110–11116 (2016). [8](#), [48](#), [64](#), [65](#)
- [67] Vladimir Tsurkan, Hans-Albrecht Krug von Nidda, Joachim Deisenhofer, Peter Lunkenheimer, and Alois Loidl, On the complexity of spinels: Magnetic, electronic, and polar ground states, *Physics Reports* **926**, pp. 1–86 (2021), On the complexity of spinels: Magnetic, electronic, and polar ground states. [8](#)
- [68] M. Hussein N. Assadi, J. Julio Gutierrez Moreno, and Marco Fronzi, High-Performance Thermoelectric Oxides Based on Spinel Structure, *ACS Applied Energy Materials* **3**(6), pp. 5666–5674 (2020). [8](#)
- [69] G. Jeffrey Snyder and Eric S. Toberer, Complex thermoelectric materials, *Nature Materials* **7**(2), pp. 105–114 (2008). [9](#)
- [70] J. Korringa and A.N. Gerritsen, The cooperative electron phenomenon in dilute alloys, *Physica* **19**(1), pp. 457–507 (1953). [9](#)
- [71] Joseph P. Heremans, Bartłomiej Wiendlocha, and Audrey M. Chamoire, Resonant levels in bulk thermoelectric semiconductors, *Energy Environ. Sci.* **5**, pp. 5510–5530 (2012). [10](#), [37](#)
- [72] Joseph P. Heremans, Vladimir Jovovic, Eric S. Toberer, Ali Saramat, Ken Kurosaki, Anek Charoenphakdee, Shinsuke Yamanaka, and G. Jeffrey Snyder, Enhancement of Thermoelectric Efficiency in PbTe by Distortion of the Electronic Density of States, *Science* **321**(5888), pp. 554–557 (2008). [11](#), [36](#), [37](#)
- [73] R. M. Martin, editor, *Electronic Structure: Basic Theory and Practical Methods*, Cambridge University Press, New York 2 edition (2004). [15](#), [17](#)
- [74] W. Hohenberg and P. Kohn, Inhomogeneous electron gas, *Phys. Rev.* **136**, pp. 864–871 (1964). [15](#)

- [75] Jean-Louis Calais, Density-functional theory of atoms and molecules. R.G. Parr and W. Yang, Oxford University Press, New York, Oxford, 1989. IX + 333 pp., *International Journal of Quantum Chemistry* **47**(1), pp. 101–101 (1993). [15](#)
- [76] W. Kohn and L. J. Sham, Self-consistent equations including exchange and correlation effects, *Phys. Rev.* **140**(4A), pp. A1133–A1138 (1965). [17](#)
- [77] A. D. Becke, Density-functional exchange-energy approximation with correct asymptotic behavior, *Phys. Rev. A* **38**, pp. 3098–3100 (1988). [21](#)
- [78] Yue Wang and John P. Perdew, Spin scaling of the electron-gas correlation energy in the high-density limit, *Phys. Rev. B* **43**, pp. 8911–8916 (1991). [21](#)
- [79] John P. Perdew, Kieron Burke, and Matthias Ernzerhof, Generalized Gradient Approximation Made Simple [Phys. Rev. Lett. 77, 3865 (1996)], *Phys. Rev. Lett.* **78**, pp. 1396–1396 (1997). [21](#), [38](#), [49](#), [66](#)
- [80] Hendrik J. Monkhorst and James D. Pack, Special points for Brillouin-zone integrations, *Phys. Rev. B* **13**, pp. 5188–5192 (1976). [22](#), [38](#), [49](#), [66](#)
- [81] D. R. Hamann, M. Schlüter, and C. Chiang, Norm-Conserving Pseudopotentials, *Phys. Rev. Lett.* **43**, pp. 1494–1497 (1979). [23](#), [49](#), [66](#)
- [82] David Vanderbilt, Soft self-consistent pseudopotentials in a generalized eigenvalue formalism, *Phys. Rev. B* **41**, pp. 7892–7895 (1990). [23](#), [38](#), [49](#)
- [83] J. Frenkle, *Wave Mechanics : Elementary Theory*, Oxford, UK: Oxford University Press (1932). [23](#)
- [84] G.D. Mahan, *Many-Particle Physics*, Plenum, New York 2 edition (1993). [24](#)
- [85] Feliciano Giustino, Electron-phonon interactions from first principles, *Rev. Mod. Phys.* **89**, pp. 015003 (2017). [25](#), [29](#), [31](#), [32](#), [33](#), [68](#)
- [86] J. Bardeen and W. Shockley, Deformation Potentials and Mobilities in Non-Polar Crystals, *Phys. Rev.* **80**, pp. 72–80 (1950). [26](#)
- [87] Michel M. Dacorogna, Marvin L. Cohen, and Pui K. Lam, Self-Consistent Calculation of the q Dependence of the Electron-Phonon Coupling in Aluminum, *Phys. Rev. Lett.* **55**, pp. 837–840 (1985). [27](#)

- [88] A. A. MARADUDIN and S. H. VOSKO, Symmetry Properties of the Normal Vibrations of a Crystal, *Rev. Mod. Phys.* **40**, pp. 1–37 (1968). [28](#)
- [89] Stefano Baroni, Stefano de Gironcoli, Andrea Dal Corso, and Paolo Giannozzi, Phonons and related crystal properties from density-functional perturbation theory, *Rev. Mod. Phys.* **73**, pp. 515–562 (2001). [28](#), [31](#), [32](#), [67](#)
- [90] N.W. Ashcroft and N.D. Mermin, *Solid State Physics*, Saunders College Philadelphia (1976). [28](#)
- [91] A. B. Migdal, INTERACTION BETWEEN ELECTRONS AND THE LATTICE VIBRATIONS IN A NORMAL METAL, *Zhur. Eksp. Teoret. Fiz.* **34**(996) (1958). [32](#)
- [92] S. Poncé, E.R. Margine, C. Verdi, and F. Giustino, EPW: Electron-phonon coupling, transport and superconducting properties using maximally localized Wannier functions, *Computer Physics Communications* **209**, pp. 116–133 (2016). [33](#), [68](#)
- [93] Georg K.H. Madsen and David J. Singh, BoltzTraP. A code for calculating band-structure dependent quantities, *Computer Physics Communications* **175**(1), pp. 67 – 71 (2006). [34](#), [38](#), [50](#), [67](#)
- [94] Qinyong Zhang, Hui Wang, Weishu Liu, Hengzhi Wang, Bo Yu, Qian Zhang, Zhit-ing Tian, George Ni, Sangyeop Lee, Keivan Esfarjani, Gang Chen, and Zhifeng Ren, Enhancement of thermoelectric figure-of-merit by resonant states of aluminium doping in lead selenide, *Energy Environ. Sci.* **5**, pp. 5246–5251 (2012). [36](#)
- [95] Zhenyu Pan and Heng Wang, A descriptive model of thermoelectric transport in a resonant system of PbSe doped with Tl, *J. Mater. Chem. A* **7**, pp. 12859–12868 (2019). [36](#)
- [96] Jiahong Shen, Hulei Yu, Yanzhong Pei, and Yue Chen, Resonant doping in Bi-CuSeO thermoelectrics from first principles, *J. Mater. Chem. A* **5**, pp. 931–936 (2017). [37](#)
- [97] George S. Nolas, Joe Poon, and Mercouri Kanatzidis, Recent Developments in Bulk Thermoelectric Materials, *MRS Bulletin* **31**(3), pp. 199205 (2006). [37](#)

- [98] Chao Han, Qiao Sun, Zhen Li, and Shi Xue Dou, Thermoelectric Enhancement of Different Kinds of Metal Chalcogenides, *Advanced Energy Materials* **6**(15), pp. 1600498 (2016). [37](#)
- [99] R. Viennois, D. Brardan, and C. Popescu, Crystal Structure, Lattice Dynamics, and Thermodynamic Properties of a Thermoelectric Orthorhombic BaCu₂Se₂ Compound, *The Journal of Physical Chemistry C* **124**(25), pp. 13627–13638 (2020). [37](#), [40](#)
- [100] Han Zhang, Shanming Li, Dandan Li, Shifeng Jin, Shijie Shen, Tianping Ying, Zhiping Lin, Kunkun Li, Duanduan Yuan, and Huaizhou Zhao, Enhancement of the thermoelectric properties of BaCu₂Se₂ by potassium doping, *Materials Letters* **152**, pp. 117–120 (2015). [37](#)
- [101] Lihua Wu, Xin Li, Shanyu Wang, Tiansong Zhang, Jiong Yang, Wenqing Zhang, Lidong Chen, and Jihui Yang, Resonant level-induced high thermoelectric response in indium-doped GeTe, *NPG Asia Materials* **9**(e343), pp. 1–7 (2017). [37](#)
- [102] Paolo Giannozzi, Stefano Baroni, Nicola Bonini, Matteo Calandra, Roberto Car, Carlo Cavazzoni, Davide Ceresoli, Guido L Chiarotti, Matteo Cococcioni, Ismaila Dabo, Andrea Dal Corso, Stefano de Gironcoli, Stefano Fabris, Guido Fratesi, Ralph Gebauer, Uwe Gerstmann, Christos Gougoussis, Anton Kokalj, Michele Lazzeri, Layla Martin-Samos, Nicola Marzari, Francesco Mauri, Riccardo Mazzarello, Stefano Paolini, Alfredo Pasquarello, Lorenzo Paulatto, Carlo Sbraccia, Sandro Scandolo, Gabriele Sclauzero, Ari P Seitsonen, Alexander Smogunov, Paolo Umari, and Renata M Wentzcovitch, QUANTUM ESPRESSO: a modular and open-source software project for quantum simulations of materials, *Journal of Physics: Condensed Matter* **21**(39), pp. 395502 (19pp) (2009). [37](#), [49](#), [66](#)
- [103] P Giannozzi, O Andreussi, T Brumme, O Bunau, M Buongiorno Nardelli, M Calandra, R Car, C Cavazzoni, D Ceresoli, M Cococcioni, N Colonna, I Carnimeo, A Dal Corso, S de Gironcoli, P Delugas, R A DiStasio Jr, A Ferretti, A Floris, G Fratesi, G Fugallo, R Gebauer, U Gerstmann, F Giustino, T Gorni, J Jia, M Kawamura, H-Y Ko, A Kokalj, E Kkbenli, M Lazzeri, M Marsili, N Marzari, F Mauri, N L Nguyen, H-V Nguyen, A Otero de-la Roza, L Paulatto, S Ponc, D Rocca, R Sabatini, B Santra, M Schlipf, A P Seitsonen, A Smogunov, I Timrov, T Thonhauser, P Umari, N Vast, X Wu, and S Baroni, Advanced capabilities for materials

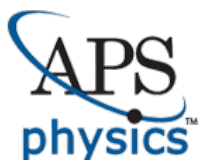
- modelling with QUANTUM ESPRESSO, *Journal of Physics: Condensed Matter* **29**(46), pp. 465901 (2017). [37](#), [49](#), [66](#)
- [104] Vladimir I. Anisimov, Jan Zaanen, and Ole K. Andersen, Band theory and Mott insulators: Hubbard U instead of Stoner I, *Phys. Rev. B* **44**, pp. 943–954 (1991). [38](#)
- [105] J.E. Iglesias, K.E. Pachali, and H. Steinfink, Structural chemistry of Ba₂CdS₃, Ba₂CdSe₃, BaCdS₂, BaCu₂S₂ and BaCu₂Se₂, *Journal of Solid State Chemistry* **9**(1), pp. 6–14 (1974). [39](#), [40](#)
- [106] Michael A. McGuire, Andrew F. May, David J. Singh, Mao-Hua Du, and Gerald E. Jellison, Transport and optical properties of heavily hole-doped semiconductors BaCu₂Se₂ and BaCu₂Te₂, *Journal of Solid State Chemistry* **184**(10), pp. 2744–2750 (2011). [39](#), [40](#)
- [107] Wenfeng Li, Zhiyong Liu, and Gui Yang, First-principles study of electronic structure, elastic and anisotropic thermoelectric properties of BaCu₂Se₂, *Journal of Alloys and Compounds* **695**, pp. 3682–3688 (2017). [40](#)
- [108] Daifeng Zou, Hairong Zheng, and Jiangyu Li, Comparative studies of the electronic structure and thermoelectric properties in orthorhombic and tetragonal BaCu₂Se₂ by first-principles calculations, *RSC Adv.* **6**, pp. 60717–60722 (2016). [40](#)
- [109] Jong-Won Song, Giacomo Giorgi, Koichi Yamashita, and Kimihiko Hirao, Communication: Singularity-free hybrid functional with a Gaussian-attenuating exact exchange in a plane-wave basis, *The Journal of Chemical Physics* **138**(24), pp. 241101 (2013). [39](#), [49](#), [82](#)
- [110] V. Goyal, D. Teweldebrhan, and A. A. Balandin, Mechanically-exfoliated stacks of thin films of Bi₂Te₃ topological insulators with enhanced thermoelectric performance, *Applied Physics Letters* **97**(13), pp. 133117 (2010). [47](#), [65](#)
- [111] T. C. Harman, P. J. Taylor, M. P. Walsh, and B. E. LaForge, Quantum Dot Superlattice Thermoelectric Materials and Devices, *Science* **297**(5590), pp. 2229–2232 (2002). [47](#), [65](#)
- [112] T. C. Harman, M. P. Walsh, B. E. laforge, and G. W. Turner, Nanostructured thermoelectric materials, *Journal of Electronic Materials* **34**(5), pp. L19–L22 (2005). [47](#), [65](#)

- [113] Jun Mao, Zihang Liu, and Zhifeng Ren, Size effect in thermoelectric materials, *npj Quantum Materials* **1**, pp. 1–9 (2016). [47](#), [65](#)
- [114] Long Cheng, Huijun Liu, Xiaojian Tan, Jie Zhang, Jie Wei, Hongyan Lv, Jing Shi, and Xinfeng Tang, Thermoelectric Properties of a Monolayer Bismuth, *The Journal of Physical Chemistry C* **118**(2), pp. 904–910 (2014). [47](#), [65](#)
- [115] Kai-Xuan Chen, Xiao-Ming Wang, Dong-Chuan Mo, and Shu-Shen Lyu, Thermoelectric Properties of Transition Metal Dichalcogenides: From Monolayers to Nanotubes, *The Journal of Physical Chemistry C* **119**(47), pp. 26706–26711 (2015). [47](#), [65](#)
- [116] Joseph R. Sootsman, Huijun Kong, Ctirad Uher, Jonathan James D’Angelo, Chun-I Wu, Timothy P. Hogan, Thierry Caillat, and Mercouri G. Kanatzidis, Large Enhancements in the Thermoelectric Power Factor of Bulk PbTe at High Temperature by Synergistic Nanostructuring, *Angewandte Chemie International Edition* **47**(45), pp. 8618–8622 (2008). [47](#), [65](#)
- [117] Chao Han null, Zhen Li null, and Shixue Dou null, Recent progress in thermoelectric materials, *Chinese Science Bulletin* **59**(18), pp. 2073–2091 (2014). [47](#), [65](#)
- [118] Zeyu Liu, J. O. Morales-Ferreiro, and Tengfei Luo, First-principles study of thermoelectric properties of blue phosphorene, *Applied Physics Letters* **113**(6), pp. 063903 (2018). [47](#)
- [119] Hasan Babaei, J. M. Khodadadi, and Sanjiv Sinha, Large theoretical thermoelectric power factor of suspended single-layer MoS₂, *Applied Physics Letters* **105**(19), pp. 193901 (2014). [47](#)
- [120] Wen Huang, Haixia Da, and Gengchiao Liang, Thermoelectric performance of MX₂ (M=Mo,W; X=S,Se) monolayers, *Journal of Applied Physics* **113**(10), pp. 104304 (2013). [47](#)
- [121] Darshana Wickramaratne, Ferdows Zahid, and Roger K. Lake, Electronic and thermoelectric properties of few-layer transition metal dichalcogenides, *The Journal of Chemical Physics* **140**(12), pp. 124710 (2014). [47](#)

- [122] Michele Buscema, Maria Barkelid, Val Zwiller, Herre S. J. van der Zant, Gary A. Steele, and Andres Castellanos-Gomez, Large and Tunable Photothermoelectric Effect in Single-Layer MoS₂, *Nano Letters* **13**(2), pp. 358–363 (2013), PMID: 23301811. [47](#)
- [123] Manish Kumar Mohanta, Ashima Rawat, Nityasagar Jena, Dimple, Raihan Ahammed, and Abir De Sarkar, Interfacing Boron Monophosphide with Molybdenum Disulfide for an Ultrahigh Performance in Thermoelectrics, Two-Dimensional Excitonic Solar Cells, and Nanopiezotronics, *ACS Applied Materials & Interfaces* **12**(2), pp. 3114–3126 (2020), PMID: 31904214. [48](#)
- [124] V. Hung Nguyen, M. Chung Nguyen, Huy-Viet Nguyen, J. Saint-Martin, and P. Dollfus, Enhanced thermoelectric figure of merit in vertical graphene junctions, *Applied Physics Letters* **105**(13), pp. 133105 (2014). [48](#)
- [125] Guangqian Ding, Cong Wang, Guoying Gao, Kailun Yao, Chaochao Dun, Chunbao Feng, Dengfeng Li, and Gang Zhang, Engineering of charge carriers via a two-dimensional heterostructure to enhance the thermoelectric figure of merit, *Nanoscale* **10**, pp. 7077–7084 (2018). [48](#)
- [126] Andrea Dal Corso, Pseudopotentials periodic table: From H to Pu, *Computational materials science* **95**, pp. 337–350 (2014). [49](#), [66](#)
- [127] Andrea Dal Corso and Adriano Mosca Conte, Spin-orbit coupling with ultrasoft pseudopotentials: Application to Au and Pt, *Phys. Rev. B* **71**, pp. 115106 (2005). [49](#)
- [128] Ma Fengxian, Zhou Mei, Jiao Yalong, Gao Guoping, Gu Yuantong, Bilic Ante, Chen Zhongfang, and Du Aijun, Single Layer Bismuth Iodide: Computational Exploration of Structural, Electrical, Mechanical and Optical Properties, *Scientific Reports* **5**, pp. 1–9 (2015). [51](#), [53](#), [54](#), [55](#), [57](#), [66](#), [69](#)
- [129] Fawad Khan, H.U. Din, S.A. Khan, G. Rehman, M. Bilal, Chuong V. Nguyen, Iftikhar Ahmad, Li-Yong Gan, and B. Amin, Theoretical investigation of electronic structure and thermoelectric properties of MX₂ (M=Zr, Hf; X=S, Se) van der Waals heterostructures, *Journal of Physics and Chemistry of Solids* **126**, pp. 304 – 309 (2019). [54](#)

- [130] B. Amin, N. Singh, and U. Schwingenschlögl, Heterostructures of transition metal dichalcogenides, *Phys. Rev. B* **92**, pp. 075439 (2015). [54](#)
- [131] Xu-Jin Ge, Dan Qin, Kai-Lun Yao, and Jing-Tao L, First-principles study of thermoelectric transport properties of monolayer gallium chalcogenides, *Journal of Physics D: Applied Physics* **50**(40), pp. 405301 (2017). [54](#)
- [132] Qiyi Zhao, Yaohui Guo, Keyu Si, Zhaoyu Ren, Jintao Bai, and Xinlong Xu, Elastic, electronic, and dielectric properties of bulk and monolayer ZrS₂, ZrSe₂, HfS₂, HfSe₂ from van der Waals density-functional theory, *physica status solidi (b)* **254**(9), pp. 1700033 (2017). [55](#), [57](#), [66](#)
- [133] Mahmud Abdulsalam and Daniel P. Joubert, Optical spectrum and excitons in bulk and monolayer MX₂ (M=Zr, Hf; X=S, Se), *physica status solidi (b)* **253**(4), pp. 705–711 (2016). [55](#), [57](#), [66](#)
- [134] Dan Mu, Wei Zhou, Yundan Liu, Jin Li, Ming Yang, Jincheng Zhuang, Yi Du, and Jianxin Zhong, Resolving the intrinsic bandgap and edge effect of BiI₃ film epitaxially grown on graphene, *Materials Today Physics* **20**, pp. 100454 (2021). [57](#)
- [135] Kai Liu, Qimin Yan, Michelle Chen, Wen Fan, Yinghui Sun, Joonki Suh, Deyi Fu, Sangwook Lee, Jian Zhou, Sefaattin Tongay, Jie Ji, Jeffrey B. Neaton, and Junqiao Wu, Elastic Properties of Chemical-Vapor-Deposited Monolayer MoS₂, WS₂, and Their Bilayer Heterostructures, *Nano Letters* **14**(9), pp. 5097–5103 (2014), PMID: 25120033. [58](#)
- [136] Sobhit Singh, Camilo Espejo, and Aldo H. Romero, Structural, electronic, vibrational, and elastic properties of graphene/MoS₂ bilayer heterostructures, *Phys. Rev. B* **98**, pp. 155309 (2018). [58](#)
- [137] Jun Yan, Prashun Gorai, Brenden Ortiz, Sam Miller, Scott A. Barnett, Thomas Mason, Vladan Stevanovi, and Eric S. Toberer, Material descriptors for predicting thermoelectric performance, *Energy Environ. Sci.* **8**, pp. 983–994 (2015). [64](#)
- [138] Guangzong Xing, Jifeng Sun, Yuwei Li, Xiaofeng Fan, Weitao Zheng, and David J. Singh, Electronic fitness function for screening semiconductors as thermoelectric materials, *Phys. Rev. Materials* **1**, pp. 065405 (2017). [64](#)

- [139] Madhubanti Mukherjee, George Yumnam, and Abhishek K. Singh, High Thermoelectric Figure of Merit via Tunable Valley Convergence Coupled Low Thermal Conductivity in $A^{II}B^{IV}C_2^V$ Chalcopyrites, *The Journal of Physical Chemistry C* **122**(51), pp. 29150–29157 (2018). [64](#)
- [140] Bolin Liao, Jiawei Zhou, Bo Qiu, Mildred S. Dresselhaus, and Gang Chen, Ab initio study of electron-phonon interaction in phosphorene, *Phys. Rev. B* **91**, pp. 235419 (2015). [65](#)
- [141] V. G. Tyuterev, Interaction of electrons with polar optical phonons in semiconductor superlattices, *Physics of the Solid State* **47**, pp. 560–570 (2005). [65](#)
- [142] Nina Glebko and Antti J. Karttunen, Lattice thermal conductivity of TiS_2 , ZrS_2 , and HfS_2 : Periodic trends studied by dispersion-corrected hybrid density functional methods, *Phys. Rev. B* **100**, pp. 024301 (2019). [65](#)
- [143] Prasenjit Ghosh Gautam Sharma, Shouvik Datta, First Principles Investigations of Structural, Electronic and Transport Properties of BiI_3/ZrS_2 van der Waals Heterostructure: A Thermoelectric Perspective, *Journal of Electronic Materials* (2020). [67](#)



American Physical Society Reuse and Permissions License

14-Sep-2021

This license agreement between the American Physical Society ("APS") and Gautam Sharma ("You") consists of your license details and the terms and conditions provided by the American Physical Society and SciPris.

Licensed Content Information

License Number: RNP/21/SEP/044508
License date: 14-Sep-2021
DOI: 10.1103/RevModPhys.64.1045
Title: Iterative minimization techniques for ab initio total-energy calculations: molecular dynamics and conjugate gradients
Author: M. C. Payne et al.
Publication: Reviews of Modern Physics
Publisher: American Physical Society
Cost: USD \$ 0.00

Request Details

Does your reuse require significant modifications: No
Specify intended distribution locations: Worldwide
Reuse Category: Reuse in a thesis/dissertation
Requestor Type: Student
Items for Reuse: Figures/Tables
Number of Figure/Tables: 5
Figure/Tables Details: Schematic of Pseudo potential and corresponding wavefunction
Format for Reuse: Print and Electronic
Total number of print copies: Up to 1000

Information about New Publication:

University/Publisher: IISER Pune, India
Title of dissertation/thesis: First Principles Investigation of Thermoelectric Materials
Author(s): Gautam Sharma
Expected completion date: Dec. 2021

License Requestor Information

Name: Gautam Sharma
Affiliation: Individual
Email Id: gautam.sharma@students.iiserpune.ac.in
Country: India

TERMS AND CONDITIONS

The American Physical Society (APS) is pleased to grant the Requestor of this license a non-exclusive, non-transferable permission, limited to Print and Electronic format, provided all criteria outlined below are followed.

1. You must also obtain permission from at least one of the lead authors for each separate work, if you haven't done so already. The author's name and affiliation can be found on the first page of the published Article.
2. For electronic format permissions, Requestor agrees to provide a hyperlink from the reprinted APS material using the source material's DOI on the web page where the work appears. The hyperlink should use the standard DOI resolution URL, <http://dx.doi.org/{DOI}>. The hyperlink may be embedded in the copyright credit line.
3. For print format permissions, Requestor agrees to print the required copyright credit line on the first page where the material appears: "Reprinted (abstract/excerpt/figure) with permission from [(FULL REFERENCE CITATION) as follows: Author's Names, APS Journal Title, Volume Number, Page Number and Year of Publication.] Copyright (YEAR) by the American Physical Society."
4. Permission granted in this license is for a one-time use and does not include permission for any future editions, updates, databases, formats or other matters. Permission must be sought for any additional use.
5. Use of the material does not and must not imply any endorsement by APS.
6. APS does not imply, purport or intend to grant permission to reuse materials to which it does not hold copyright. It is the requestor's sole responsibility to ensure the licensed material is original to APS and does not contain the copyright of another entity, and that the copyright notice of the figure, photograph, cover or table does not indicate it was reprinted by APS with permission from another source.
7. The permission granted herein is personal to the Requestor for the use specified and is not transferable or assignable without express written permission of APS. This license may not be amended except in writing by APS.
8. You may not alter, edit or modify the material in any manner.
9. You may translate the materials only when translation rights have been granted.
10. APS is not responsible for any errors or omissions due to translation.
11. You may not use the material for promotional, sales, advertising or marketing purposes.
12. The foregoing license shall not take effect unless and until APS or its agent, Aptara, receives payment in full in accordance with Aptara Billing and Payment Terms and Conditions, which are incorporated herein by reference.
13. Should the terms of this license be violated at any time, APS or Aptara may revoke the license with no refund to you and seek relief to the fullest extent of the laws of the USA. Official written notice will be made using the contact information provided with the permission request. Failure to receive such notice will not nullify revocation of the permission.
14. APS reserves all rights not specifically granted herein.
15. This document, including the Aptara Billing and Payment Terms and Conditions, shall be the entire agreement between the parties relating to the subject matter hereof.

SPRINGER NATURE LICENSE
TERMS AND CONDITIONS

Aug 19, 2021

This Agreement between Mr. Gautam Sharma -- Gautam Sharma ("You") and Springer Nature ("Springer Nature") consists of your license details and the terms and conditions provided by Springer Nature and Copyright Clearance Center.

License Number 5131960798300

License date Aug 18, 2021

Licensed Content
Publisher Springer NatureLicensed Content
Publication Journal of Electronic MaterialsLicensed Content Title First Principles Investigations of Structural, Electronic and
Transport Properties of $\text{BiI}_3/\text{ZrS}_2$ BiI₃ /
ZrS₂ van der Waals Heterostructure: A Thermoelectric PerspectiveLicensed Content
Author Gautam Sharma et al

Licensed Content Date Oct 8, 2020

Type of Use Thesis/Dissertation

Requestor type academic/university or research institute

Format print and electronic

Portion full article/chapter

Will you be translating? no

Circulation/distribution 1 - 29

Author of this Springer Nature content yes

Title Mr. Gautam Sharma

Institution name IISER Pune

Expected presentation date Jan 2022

Order reference number NA

Mr. Gautam Sharma
State bank nagar

Requestor Location
PUNE, MAHARASHTRA 411008
India
Attn: Mr. Gautam Sharma

Total 0.00 USD

Terms and Conditions

Springer Nature Customer Service Centre GmbH Terms and Conditions

This agreement sets out the terms and conditions of the licence (the **Licence**) between you and **Springer Nature Customer Service Centre GmbH** (the **Licensor**). By clicking 'accept' and completing the transaction for the material (**Licensed Material**), you also confirm your acceptance of these terms and conditions.

1. Grant of License

1. 1. The Licensor grants you a personal, non-exclusive, non-transferable, world-wide licence to reproduce the Licensed Material for the purpose specified in your order only. Licences are granted for the specific use requested in the order and for no other

use, subject to the conditions below.

1. 2. The Licensor warrants that it has, to the best of its knowledge, the rights to license reuse of the Licensed Material. However, you should ensure that the material you are requesting is original to the Licensor and does not carry the copyright of another entity (as credited in the published version).

1. 3. If the credit line on any part of the material you have requested indicates that it was reprinted or adapted with permission from another source, then you should also seek permission from that source to reuse the material.

2. Scope of Licence

2. 1. You may only use the Licensed Content in the manner and to the extent permitted by these Ts&Cs and any applicable laws.

2. 2. A separate licence may be required for any additional use of the Licensed Material, e.g. where a licence has been purchased for print only use, separate permission must be obtained for electronic re-use. Similarly, a licence is only valid in the language selected and does not apply for editions in other languages unless additional translation rights have been granted separately in the licence. Any content owned by third parties are expressly excluded from the licence.

2. 3. Similarly, rights for additional components such as custom editions and derivatives require additional permission and may be subject to an additional fee. Please apply to Journalpermissions@springernature.com/bookpermissions@springernature.com for these rights.

2. 4. Where permission has been granted **free of charge** for material in print, permission may also be granted for any electronic version of that work, provided that the material is incidental to your work as a whole and that the electronic version is essentially equivalent to, or substitutes for, the print version.

2. 5. An alternative scope of licence may apply to signatories of the [STM Permissions Guidelines](#), as amended from time to time.

3. Duration of Licence

3. 1. A licence for is valid from the date of purchase ('Licence Date') at the end of the relevant period in the below table:

Scope of Licence	Duration of Licence
Post on a website	12 months
Presentations	12 months
Books and journals	Lifetime of the edition in the language purchased

4. Acknowledgement

4. 1. The Licensor's permission must be acknowledged next to the Licenced Material in print. In electronic form, this acknowledgement must be visible at the same time as the figures/tables/illustrations or abstract, and must be hyperlinked to the journal/book's homepage. Our required acknowledgement format is in the Appendix below.

5. Restrictions on use

5. 1. Use of the Licensed Material may be permitted for incidental promotional use and minor editing privileges e.g. minor adaptations of single figures, changes of format, colour and/or style where the adaptation is credited as set out in Appendix 1 below. Any other changes including but not limited to, cropping, adapting, omitting material that affect the meaning, intention or moral rights of the author are strictly prohibited.

5. 2. You must not use any Licensed Material as part of any design or trademark.

5. 3. Licensed Material may be used in Open Access Publications (OAP) before publication by Springer Nature, but any Licensed Material must be removed from OAP sites prior to final publication.

6. Ownership of Rights

6. 1. Licensed Material remains the property of either Licensor or the relevant third party and any rights not explicitly granted herein are expressly reserved.

7. Warranty

IN NO EVENT SHALL LICENSOR BE LIABLE TO YOU OR ANY OTHER PARTY OR ANY OTHER PERSON OR FOR ANY SPECIAL, CONSEQUENTIAL, INCIDENTAL OR INDIRECT DAMAGES, HOWEVER CAUSED, ARISING OUT OF OR IN CONNECTION WITH THE DOWNLOADING, VIEWING OR USE OF THE MATERIALS REGARDLESS OF THE FORM OF ACTION, WHETHER FOR BREACH OF CONTRACT, BREACH OF WARRANTY, TORT, NEGLIGENCE, INFRINGEMENT OR OTHERWISE (INCLUDING, WITHOUT LIMITATION, DAMAGES BASED ON LOSS OF PROFITS, DATA, FILES, USE, BUSINESS OPPORTUNITY OR CLAIMS OF THIRD PARTIES), AND WHETHER OR NOT THE PARTY HAS BEEN ADVISED OF THE POSSIBILITY OF SUCH DAMAGES. THIS LIMITATION SHALL APPLY NOTWITHSTANDING ANY FAILURE OF ESSENTIAL PURPOSE OF ANY LIMITED REMEDY PROVIDED HEREIN.

8. Limitations

8. 1. BOOKS ONLY: Where '**reuse in a dissertation/thesis**' has been selected the following terms apply: Print rights of the final author's accepted manuscript (for clarity, NOT the published version) for up to 100 copies, electronic rights for use only on a personal website or institutional repository as defined by the Sherpa guideline

(www.sherpa.ac.uk/romeo/).

8. 2. For content reuse requests that qualify for permission under the [STM Permissions Guidelines](#), which may be updated from time to time, the STM Permissions Guidelines supersede the terms and conditions contained in this licence.

9. Termination and Cancellation

9. 1. Licences will expire after the period shown in Clause 3 (above).

9. 2. Licensee reserves the right to terminate the Licence in the event that payment is not received in full or if there has been a breach of this agreement by you.

Appendix 1 — Acknowledgements:

For Journal Content:

Reprinted by permission from [the Licensor]: [Journal Publisher (e.g. Nature/Springer/Palgrave)] [JOURNAL NAME] [REFERENCE CITATION (Article name, Author(s) Name), [COPYRIGHT] (year of publication)]

For Advance Online Publication papers:

Reprinted by permission from [the Licensor]: [Journal Publisher (e.g. Nature/Springer/Palgrave)] [JOURNAL NAME] [REFERENCE CITATION (Article name, Author(s) Name), [COPYRIGHT] (year of publication), advance online publication, day month year (doi: 10.1038/sj.[JOURNAL ACRONYM].)]

For Adaptations/Translations:

Adapted/Translated by permission from [the Licensor]: [Journal Publisher (e.g. Nature/Springer/Palgrave)] [JOURNAL NAME] [REFERENCE CITATION (Article name, Author(s) Name), [COPYRIGHT] (year of publication)]

Note: For any republication from the British Journal of Cancer, the following credit line style applies:

Reprinted/adapted/translated by permission from [the Licensor]: on behalf of Cancer Research UK: : [Journal Publisher (e.g. Nature/Springer/Palgrave)] [JOURNAL NAME] [REFERENCE CITATION (Article name, Author(s) Name), [COPYRIGHT] (year of publication)]

For Advance Online Publication papers:

Reprinted by permission from The [the Licensor]: on behalf of Cancer Research UK: [Journal Publisher (e.g. Nature/Springer/Palgrave)] [JOURNAL NAME] [REFERENCE CITATION (Article name, Author(s) Name), [COPYRIGHT] (year of publication), advance online publication, day month year (doi: 10.1038/sj.[JOURNAL ACRONYM].)]

For Book content:

Reprinted/adapted by permission from [the Licensor]: [Book Publisher (e.g. Palgrave Macmillan, Springer etc)] [Book Title] by [Book author(s)] [COPYRIGHT] (year of publication)

Other Conditions:

Version 1.3

Questions? customercare@copyright.com or +1-855-239-3415 (toll free in the US) or +1-978-646-2777.
